Behavior of SiC-SiC Composite Laminates Under Multiaxial Load States: Experiments and Simulations

by

Lucas R. Hansen

A dissertation submitted in partial fulfillment
of the requirements for the degree of
Doctor of Philosophy
(Aerospace Engineering)
in the University of Michigan
2015

Doctoral Committee:

Professor Anthony M. Waas, Chair
Associate Professor Samantha H. Daly
Professor John W. Halloran
Associate Professor Veera Sundararaghavan

2015

To my family.

A C K N O W L E D G M E N T S

Although only one author appears on the cover of this dissertation, a PhD is far from an individual effort. Numerous individuals have contributed in their own ways, large and small, to making this work happen.

Firstly, I would like to acknowledge GE Aviation, whose funding allowed this work to happen. I would like to thank my student colleagues on this project, Jared Tracy, Brad Wing, and Pascal Meyer for insight, assistance, and general helpfulness throughout the course of this project. I would also like to thank all of the past and current members of the Composite Structures Lab, for various assistance in the labs and with software, bouncing ideas, and all the other little ways that a successful research group supports the individuals within.

Further, I would like to acknowledge the following persons: The U-M Aerospace Department Technical support staff, especially Tom Griffin and Terry Larrow; Dr. Kathleen Sevener for her assistance with the SEM and other insights; Evan Pineda, Brett Bednarcyk, and Steve Arnold of NASA Glenn Research Center for providing and assisting with MAC/GMC and FEAMAC; all of my friends in and out of the department for helping maintain sanity during five years of research, and the members of my committee and my advisor, Prof. Tony Waas, for his guidance and support over the years.

Lastly, I would like to thank my family for everything they've provided over the last nine years of college and 27 years of my life. Yes, Mom and Dad, I'm actually done.

TABLE OF CONTENTS

LIST OF FIGURES

Figure

LIST OF TABLES

Table

LIST OF APPENDICES

Appendix

LIST OF ABBREVIATIONS

CMC Ceramic Matrix Composite

MOC Method of Cells

GMC Generalized Method of Cells

RUC Representative Unit Cell

DIC Digital Image Correlation

FRC Fiber-reinforced Composite

FRP Fiber-reinforced Polymer

PLH Ply-Level Homogenization, Ply-level homogenized

PL Proportional Limit

SiC Silicon Carbide

CTE Coefficient of Thermal Expansion

EPS Effective Processing Strain

ASTM American Society for Testing and Materials

ABSTRACT

Fiber-reinforced ceramic reinforced composites are a promising material class for use in high temperature structural applications, such as the hot sections of gas turbine engines. Monolithic ceramics possess certain desirable properties under these service conditions: namely creep resistance and retention of strength at elevated temperature. Use of CMCs in engineering applications, however, is limited by the low toughness of ceramic monoliths. By reinforcing the ceramic with coated fibers, the toughness of the CMC is dramatically increased. However, the behavior of such materials under multiaxial load states is not well understood. To this end, CMC laminates are tested under a state of biaxial flexure at room and elevated temperature in an atmospheric environment. From these tests, the strength and strain-to-failure of a the CMC ply is determined. Appropriate constituent failure models and failure criteria are determined, and multiscale simulations of the biaxial flexure tests are carried out, using a framework combining the Generalized Method of Cells at the microscale with the Finite Element Method at the macroscale.

CHAPTER 1

Introduction

In recent years, composite materials (especially continuous fiber-reinforced polymers) have become increasingly used as primary structural materials in the aerospace and automotive industries. This is due to the significant weight savings that are possible over metals in these applications, as well as the high toughness associated with Fiber-reinforced Composite (FRC)s. Unfortunately, Fiber-reinforced Polymer (FRP)s are only usable at relatively low temperatures due to the nature of the polymer matrix. Ceramic Matrix Composite (CMC)s are a class of materials capable of operating within high temperature environments, such as engines, that have previously been the domain of super alloys. Any component made form these materials will see multiaxial stress states in service. However, much of the literature available has focused on uniaxial characterization of CMCs. The objective the this research is to characterize the behavior and response of laminated CMCs under in-plane biaxial stress states, and to develop a methodology for simulating the behavior of these materials. To this end, CMC specimens were tested under ring-on-ring biaxial flexure, and a multiscale method of material simulation was validated against these results. The multiscale approach used for this research is a three-scale hybrid hierarchical/concurrent method. In this method, the finest scale (referred to as the sub-microscale) is handled separately from the fiber/matrix scale (microscale) and the coupon scale (macroscale). In the sub-microscale, only linear thermoelastic and phase-change effects are considered, to provide part of the constituent behavior for the matrix in the microscale. The micro- and macroscales are then solved concurrently to investigate damage progression in the composite. This methodology is considered in greater detail in Chapter 4

1.1 Overview of Ceramic Matrix Composites

Ceramic materials posses several properties that are useful in engineering structural applications. They have a higher resistance to elevated temperature than metals or polymers. However, use of ceramic materials in load-bearing roles has been limited by their poor fracture toughness. A

method of improving the toughness of ceramics is to reinforce the monolith with fibers. These fibers can then bridge the crack, thus resisting the opening of the crack mouth and providing resistance to increased crack growth. For this to be effective, a coating id often applied to the fiber, preventing the matrix crack from penetrating directly into the fiber; instead, the crack is deflected around the fiber, leaving the fiber intact [4, 5, 6, 7]

Similar to FRPs, there are several available architectures for CMCs, such as laminates or various woven architectures. The choice of construction depends on the desired properties: woven CMCs tend to possess better interlaminar properties at the expense of greatly increased porosity and degraded in-plane properties as compared to laminates. [8, 9, 10]

1.1.1 Material of Consideration

In this work, the material of focus is a laminated CMC comprising a Silicon Carbide (SiC) matrix and a SiC fiber. The fiber is coated with a proprietary interphase coating. Figure 1.1 shows a micrograph of a typical laminate SiC-SiC microstructure. Note that in these materials, the interphase thickness is on the order of the fiber diameter.

The material under consideration in this research has a fiber volume fraction of 25%. This is much lower than the fiber volume fraction seen in FRPs. All specimens used in this study are of an 8-ply, $[0/90]_{2s}$ construction. Unless otherwise noted, the 0-plies are always taken to be on the outer surface.[2]

[2]Due to the circular shape of the ring-on-ring tests, the layup could be labeled by $[\theta/\theta + 90]_{2s}$ for any θ. The choice of $[0/90]_{2s}$ is chosen for convenience.

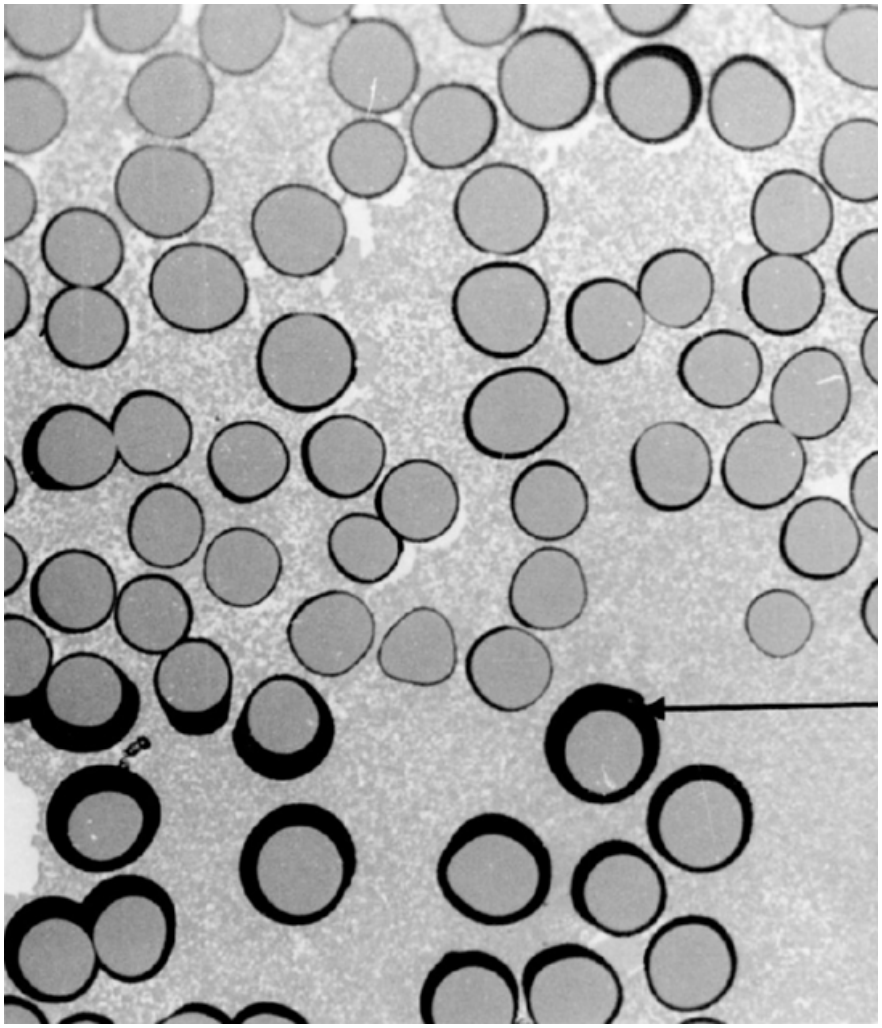

Figure 1.1: A micrograph showing the microstructure of a SiC-SiC laminate, from [1]

1.2 Background: Uniaxial Testing And Characterization of CMCs

There exists a considerable body of work on the testing of CMCs under uniaxial tension and flexure. Much of this work has been focused on woven architectures, rather that the laminate architecture considered in this work. Zhang [11] considered the fracture behavior of plain woven [0/90] CMCs. Jones, et al, [12] examined subcritical crack growth in 2D woven SiC/SiC CMCs under adverse environmental conditions. Some work on laminate architecture CMCs has been reported. Marshall and Evans examined SiC/Glass unidirectional CMCs under uniaxial flexure [4]. This work also used indentation testing to demonstrate the residual stress present in the composite. Morscher has examined woven and laminated CMCs with electrical resistance and acoustic emission techniques, demonstrating the existence of matrix cracks prior to the proportional limit point on the experimental curves [13, 14, 15]

With regards to microscale testing, Morscher considered the behavior of CMC microcomposites consisting of a single tow under uniaxial tension [13]. This provided insight as to the pull out and fracture mechanisms in CMCs. Various micromechanical models have been proposed, including models by Lamon [16, 17], and Marshall [18, 4]. These models focus primarily on the matrix and fiber, and neglect the elastic effects of the coating, considering only the coating strength and toughness as it applies to progressive debond through or along the interphase.

1.3 Motivation for Ring-On-Ring Testing

Engineering components in service are likely to be subjected to complex multiaxial stress states throughout the course of their service lives. In order to safely design such components from any material, the behavior of that material under such stress states must be understood. There are many possible tests that can be carried out to characterize the multiaxial response of materials, or to validate multiaxial models. Such possibilities include biaxial tension of cruciforms [19], [20], combined tension/torsion or compression/torsion of tubes [20], saddle shear (i.e. anti-biaxial) flexure of plates [cite], and equibiaxial flexure of discs [2]. For the purposes of this research, biaxial flexure of discs was chosen. This choice was due to the difficulty and expensive of producing high quality cruciform tension or tension/torsion specimens. Equibiaxial flexure was chosen over saddle shear out of a desire for characterization in the tension/tension regime. Further, the ring-on-ring flexure test was chosen over other biaxial flexure methods (such as ball-on-ring or ball-on-three-balls) due to the increased size of the region subjected to maximal loads [21], [22].

1.4 Motivation for Multiscale Modeling

Composites modeling is a rich field encompassing many methods of predicting the properties and behavior of these materials and structures made from them. Each method is a trade-off between computational cost and physical fidelity.

One method of composite modeling is to homogenize each ply and treat the composite as a laminate consisting of orthotropic layers [23]. For failure analysis in this method, a multiaxial failure criterion is needed There are several such failure criterion available. Some commonly used criteria are the Hill, Tsai-Hill, and Tsai-Wu criteria [24, 25, 26] . These are all empirical criteria, which require several tests to calibrate. At a minimum, longitudinal and transverse tension, longitudinal and transverse compression, axial shear, and at least one multiaxial test are needed to calibrate the required parameters for these types of criteria [24].

The other major method of modeling is the field of multiscale modeling. In these methods, there exist models at several length scales, the number of which is to be determined by the analyst. In the current research, a pseudo three-scale framework is considered. The two larger scales used in this framework are the micromechanical scale (containing the fibers, fiber coatings, and matrix) and the structural or coupon scale, consisting of a geometric model of the specimen. These scales are linked in a concurrent fashion, and are thus solved simultaneously. The third scale is a sub-micromechanical scale, and represents the different phases that are present in the matrix phase of the micromechanical scale. This scale is linked hierarchically, and is used only to generate equivalent properties for the matrix in the micromechanical scale: no stress analysis is done at this level. The linking of scales is outlined in Figure 1.2.

The choice of micromechanical model in a multiscale analysis is made at the discretion of the analyst. This model can have nearly any level of fidelity, from simplified analytical models, to low order numerical models, to a second, fully featured finite element code (also known as FEA^2 [27, 28, 29, 30]. The choice between models comes down to a tradeoff between physical fidelity and computational cost.

For this work, the multiscale framework consisting of the generalized method of cells as a micromechanical model and the finite element method are validated for the problem of interest. This method was chosen because it occupies a point near the middle of the fidelity-cost continuum. This provides for a more physically accurate representation of the physics, but still has a computational cost which would be feasible for solving practical engineering problems.

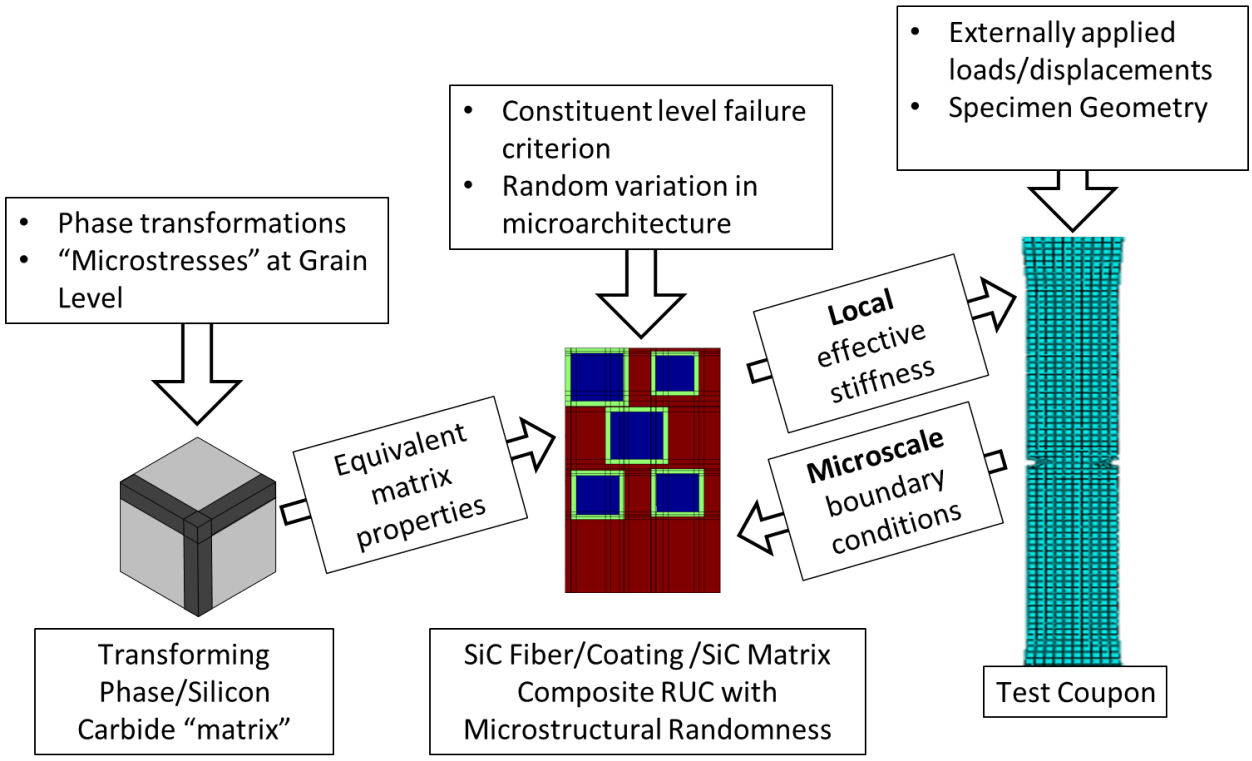

Figure 1.2: Linking of the three length scales used in this procedure. The sub-micro scale is a one-way linkage feeding into the matrix properties of the microscale model. The micro- and macroscale models are solved simultaneously.

1.5 Organization and Scope

The first portion of this dissertation covers efforts performed in stand-alone micromechanical modeling of CMCs. Chapter 2 covers a 3+1 phase concentric cylinder model which provides a more accurate estimation of the elastic properties of the CMC than existing 2+1 and 3+0 phase models. The novel contributions of this model are the combination of an explicitly modeled fiber coating phase, as well as a homogenized outer sheath of infinite extent which provides the correct boundary conditions on the cylindrical assemblage.

Chapter 3 details a second cylinder-based model used to predict the progressive cracking of a longitudinal CMC ply under uniaxial loading. This model allows for multiple Mode I cracking of the matrix as well as progressive Mode II cracking of the fiber coating. The novel contribution of this model is the explicit inclusion of the fiber coating, which is often neglected in other cracking models, an assumption which cannot be made in the case of the current material of interest.

Chapter 4 details the numerical multiscale modeling methodology used in this research. An overview of the generalized method of cells, used as the micromechanical model in this method, is given. Uniaxial simulation of cross-ply tensile coupons is used to determine the initial behavior of the CMC as well as validate the method of using random micro-architectural variations to drive multiple cracking of the matrix across the gage length of the coupon. From this work, the simulations of biaxial flexure specimens is informed and presented.

Chapter 5 presents the biaxial flexure experiments at both room temperature and an elevated temperature of 1315°C (2400°F). The room temperature experiments include DIC results collected of the tension side of the specimen and provide insight to the expected failure mode of the composite. Optical imaging of the post-test specimen is used to confirm the damage implied by the DIC results. High temperature tests are then used to investigate the reduction in properties and search for any change in failure mode at elevated temperature ultimately, it was found that the failure mode remained similar to that seen in the room temperature test. This is encouraging, as the high temperature tests lacked imaging and DIC analysis. The similarity in response mode implies that the DIC results from the room temperature tests can be used to inform further analysis of the high temperature tests. Finally, the effects of residual stress on the biaxial response were tested by annealing several specimens (in atmosphere) for 20 hours at 1315°C (2400°F). These effects are compared to the effects of the same heat treatment performed on tensile dogbone specimens for uniaxial tension. It is shown that the change in proportional limit and ultimate load are not as strongly affected in the biaxial tests as they are in the uniaxial tests.

Chapter 6 discusses the results of the multiscale simulation in more detail. First, the multiscale results are compared to the results of the ring-on-ring flexure experiments. It is shown that the pre-peak and immediate posit-peak behavior are well represented in the simulated load-displacement

curves. Further, it is shown that the final damage patterns seen in the test (including the failure well after the ultimate load). Finally, the multiscale method is compared to the lower fidelity homogenized ply-level crack band model. It is shown that while there is only slight improvement to the load-displacement results, there is a considerable increase in accuracy in the representation of the failure matter in the specimen. This improves failure representation would be of high importance if one were to attempt to implement an oxidation mode into the simulation, as the failure pattern would dramatically affect the oxygen pathways and subsequent mechanical response of the failed/oxidized specimen.

CHAPTER 2

Embedded Concentric Cylinder Model

2.1 Introduction

Prediction of the macroscopic stiffness properties of composite is a basic, but very important, step in the deployment of any new composite system. A number of approaches have been taken for fiber-reinforced composites, one of which is the concentric cylinder model proposed by Hill [31] and extended by Christensen and Lo [32]. However, these models are applicable only to composites comprising only two phases. In the area of ceramic matrix composites, the material typically includes a third interphase material between the fiber and matrix, which may account for several percent of the volume of the composite system. Understanding the influence of this third phase is critical if the proper response is to be achieved, particularly in the transverse direction where the influence of the compliant interphase may be significant.

One approach that has been taken in the past is to consider the composite as a set of nested two phase models [33]; that is, a sub-composite material comprising the fiber and interphase materials is modeled as one CCM, and then used as the fiber phase in a second two-phase CCM. While this approach is straight forward and is easily extended to an arbitrary number of phases, it does not necessarily provide good estimates of the transverse properties of the material. The current work instead considers all three phases simultaneously. To obtain the proper boundary conditions, these three phases are embedded in a fourth phase which is taken to be a transversely isotropic solid that has the properties of the composite, i.e. the properties that are sought.

The novelty of this method lies in the use of a consistent geometrical model to obtain all independent elastic constants for the material, while additionally ensuring the proper level of constraint on the assemblage. In traditional cylinder models, no homogenized outer phase in used, instead enforcing either fixed-displacement or traction-free boundary conditions on the outer radius of the assemblage. By including the homogenized outer phase, the effective boundary condition on the constituents is a mixed traction-displacement condition. This is important for use in ceramic matrix composites, as the matrix stiffness is high, and therefore the "'un-mixed"' boundary conditions

can introduce errors.

2.2 Embedded Concentric Cylinder Assemblage

In the current model, the composite is modeled as a series of four concentric cylinders, representing the fiber, interphase, matrix, and a homogenized equivalent material. At present, the inner three phases representing explicit constituents are taken to be isotropic, however the method can be extended to material models of lower symmetry. The outer phase, which has the unknown properties of the composite, is treated as a transversely isotropic solid, which the plane of isotropy is normal to the generation axis of the cylinder. The assembly is assumed to be of infinite length. The radii of the three physical phases are chosen to accurately represent the volume fractions of each constituent, and the outer, homogenized phase is assumed to be of infinite extent.

The general process to be followed is to subject the assemblage to a simple state of strain, and compute the stress associated with it. The resultant traction in the appropriate direction can then be determined, allowing stiffness in the associated direction to be computed. The process for determining the five independent elastic constants is outlined diagrammatically in Figure 2.2. In this process, the plane-strain bulk modulus and axial shear modulus (k_{23} and G_{12}), which can be calculated independently in closed form, are obtained first. They are then used to in the simultaneous solution of the remaining (coupled) elastic constants: E_{11}, ν_{12}, and G_{23}.

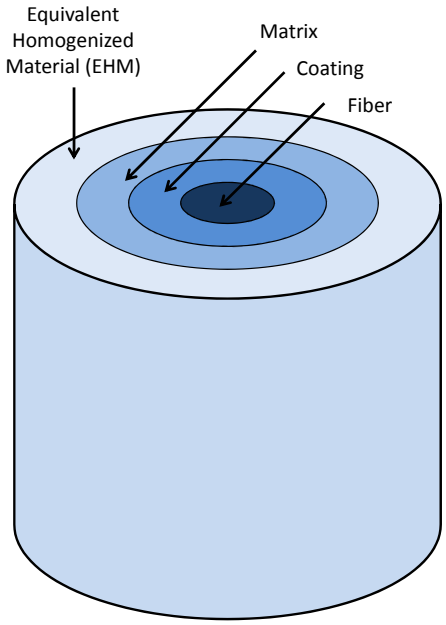

Figure 2.1: Four-phase cylindrical assembly

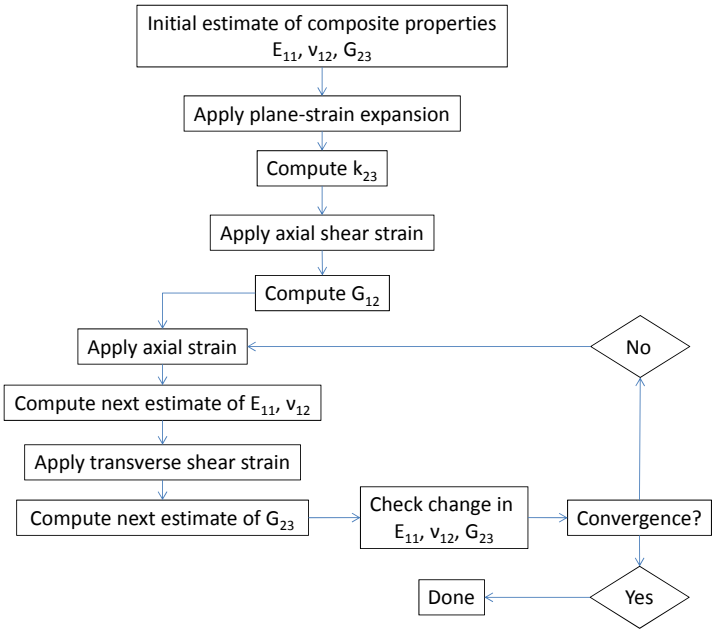

Figure 2.2: Process flow for solving the iterative cylinder model.

2.3 Step 1: Plane-strain Expansion: k_{23}

To obtain the plane strain bulk modulus, k_{23}, the assemblage is subjected to uniform expansion in the plane of isotropy, with the axial deformation constrained. This problem is axially independent and axisymmetric, so the only equilibrium equation is (for each phase) given in Equation 2.1.

$$\frac{\sigma_{rr} - \sigma_{\theta\theta}}{r} + \frac{\partial \sigma_{rr}}{\partial r} = 0 \tag{2.1}$$

The in-plane displacements take the form given in Equation 2.2.

$$u_r = Ar - \frac{B}{r} u_\theta = Ar + \frac{B}{r} \tag{2.2}$$

In this case, the axial strain is set to zero. Continuity of tractions and displacements are assumed at the interfaces. At the inner boundary, (i.e. r = 0) displacements are assumed to be finite. At the outer boundary (R_4), a radial displacement is applied

$$u_r(r = R_4) = \delta u_\theta(r = R_4) = 0 \tag{2.3}$$

The elasticity problem is formulated and solved, obtaining the stress applied at the outer boundary $r = R_4$. We then state that

$$k_{23} = \lim_{R_4 \to \infty} \frac{\sigma_r r(r = R_4)}{2\epsilon_r r} = \lim_{R_4 \to \infty} \frac{\sigma_r r(r = R_4)}{2\frac{\delta}{R_4}} \tag{2.4}$$

2.4 Step 2: Axial Shear: G_{12}

To obtain the axial shear modulus, G_{12}, the cylinder is subjected to a state of pure shear in a Cartesian frame on the outer boundary, γ_{12}. The displacements associated with this shear are given by

$$u_x = \phi(y, z) - \frac{\gamma_{xy}}{2} y u_y = \frac{\gamma_{xy}}{2} x u_z = 0 \tag{2.5}$$

where ϕ is a shear deformation function. Because only axial shear strains are present, the only non-zero stresses are the axial shear stresses, so the relevant equilibrium equation for each phase is given by

$$\frac{\partial \sigma_{rx}}{\partial r} + \frac{\sigma_{rx}}{r} + \frac{1}{r} \frac{\partial \sigma_{\theta x}}{\partial \theta} = 0 \tag{2.6}$$

which in terms of the shear deformation function is

$$\frac{\partial^2\phi}{\partial r^2} + \frac{1}{r}\frac{\partial\phi}{\partial r} + \frac{1}{r^2}\frac{\partial\phi}{\partial\theta} = 0 \tag{2.7}$$

On the outer boundary, the applied shear deformation is given by

$$\phi(r = R_4, \theta) = \gamma_{xy} R_4 cos(\theta) \tag{2.8}$$

At $r = 0$ the displacements must be finite. Again, traction and displacement continuity are assumed at all interfaces. The boundary value problem can then be solved, giving an expression for the stress applied on the outer boundary. The stress is then resolved back into a Cartesian reference frame. We then state that

$$G_{12} = \lim_{R_4\to\infty} \frac{\tau_{avg}}{\gamma_{xy}} = \lim_{R_4\to\infty} \frac{\frac{1}{2\pi R_4}\int \tau_{xy} r d\theta}{\gamma_{xy}} \tag{2.9}$$

Solving the elasticity problem and using Equation 2.9 yields a closed form expression for the axial shear modulus given by Equation 2.10, G_i indicates the shear modulus of the i^{th} phase and f_i indicates the volume fraction of the i^{th} phase.

$$\mathrm{G_{12}} = -\frac{G_3\left(f_3^2(G_3-G_2)(G_1+G_2)-2G_2(G_1+f_1G_1+G_2-f_1G_2)+f_3(G_2((1+f_1)G_3+(-3+f_1)G_2)+G_1((-1+f_1)G_3+(3+f_1)G_2))\right)}{G_1((-2+f_3)(-1+f_1+f_3)G_3+(1+f_1-f_3)f_3G_2)+G_2(-(1+f_1-f_3)(-2+f_3)G_3-f_3(-1+f_1+f_3)G_2)} \tag{2.10}$$

2.5 Step 3: Uniaxial Strain: E_{11}, ν_{12}

To obtain the axial Young's modulus and Poisson's ratio, E_{11} and ν_{12}, the cylinder is subjected to a uniform axial strain, ϵ_{xx}. This problem is independent of axial position and is axisymmetric; therefore, the only relevant equilibrium equation in each phase is given by Equation 2.11.

$$\frac{\sigma_{rr} - \sigma_{\theta\theta}}{r} + \frac{\partial\sigma_{rr}}{\partial r} = 0 \tag{2.11}$$

The radial and circumferential displacements are assumed to be of the form

$$u_r = Ar - \frac{B}{r} u_\theta = Ar + \frac{B}{r} \tag{2.12}$$

The outermost boundary of the homogenized cylinder is enforced to be traction free. At the center of the fiber (i.e. r = 0), the displacement is assumed to be finite. Continuity of tractions and displacement are assumed at the interfaces between each phase. Using the assumed deformations in conjunction with equilibrium, constitutive laws, and the usual cylindrical strain-displacement relations, formulates the elasticity problem to be solved. Expressions for the axial stress in each phase are obtained. We then state that

$$E_{11} = \lim_{R_4 \to \infty} \frac{\sigma_{avg}}{\epsilon_{xx}} \tag{2.13}$$

and

$$\nu_{12} = \lim_{R_4 \to \infty} (-\frac{\epsilon_{rr}}{\epsilon_{xx}}) \tag{2.14}$$

where R_4 is the radius of the composite equivalent phase. Solving the elasticity problem and using the solution in conjunction with Equations 2.13 and 2.14 will provide an expression for the equivalent property of the entire cylindrical assembly. These expressions are quite long, and have been omitted. Note that the expressions are implicit in terms of E_{11} and ν_{12}, and will require an iterative solution procedure to calculate.

2.6 Step 4: Transverse Shear: G_{23}

To compute the transverse shear modulus, G_{23}, the composite assemblage is subjected to a state of in-plane shear strain at the infinite boundary. The solution method for this constant is adapted from [23], and extended to include an additional phase. For this problem, the relevant equilibrium equations for each phase are

$$\frac{\partial \sigma_{rr}}{\partial r} + \frac{1}{r}\frac{\partial \sigma_{r\theta}}{\partial \theta} + \frac{\sigma_{rr} - \sigma_{\theta\theta}}{r} = 0 \frac{\partial \sigma_{r\theta}}{\partial r} + \frac{1}{r}\frac{\partial \sigma_{\theta\theta}}{\partial \theta} + 2\frac{\sigma_{r\theta}}{r} = 0 \tag{2.15}$$

Applying strain-displacement equations and the assumed displacement functions, a system of equations for the unknown constants and G_{23} can be obtained. This system can be written in a form

$$\mathbf{A}\vec{a} = \vec{b} \tag{2.16}$$

where both $\mathbf{A}$ and $\vec{b}$ contain material information, including the unknown G_{23}, and $\vec{a}$ is a column vector of the unknown constants a_i in the displacement functions. Presently, a closed form expression for G_{23} has not been obtained, and it must therefore be computed numerically using a procedure outlined in the next section.

2.7 Solution for E11, ν_{12}, and G_{23}

For Cases 2 and 3, obtaining the solution is straightforward, as a closed form expression for these properties can be obtained directly. However, Cases 1 and 4 are dependent on each other, as well as on G_{12} and k_{23}. To find E_{11}, ν_{12}, and G_{23}, an initial guess must be made for each property. The

next iteration for E_{11} and ν_{12} can then be computed from the functions determined previously. The new values for are then used to numerically compute the next iteration of G_{23}.

2.8 Comparison of Predictions

To validate the model, the predicted elastic constants are compared to experimentally determined values for GE's HiPerComp SiC/SiC composite system. The system used in this comparison is a symmetric cross ply layup, [0/90]2s. Classical lamination theory [34] is used along with the embedded CCM predictions to determine the elastic constants of the laminate. A summary of the results are provided in Table 1. Also provided in this table is the predication from a nested model, where the coated fiber is treated as a traditional 2-phase composite whose equivalent properties are then used as the "'fiber"' in a second traditional 2-phase composite. Note that this table has been normalized by the experimentally determined value for proprietary reasons.

Table 2.1: Comparison of Embedded 3-phase CCM and Nested CCM prediction, normalized by experimental value

Property	Embedded 3-phase CCM	Nested CCM
E_{11}	0.996	1.089
ν_{12}	1.007	1.007
E_{22}	0.884	0.753

Immediately evident from Table 2.1 is the superior prediction given by the explicit 3-phase model over the nested model. This is due largely to the proper handling of the compliant interphase layer. In the nested model, the transverse stiffness of the coating and fiber is averaged over the new "'coated fiber"', yielding an equivalent that is soft, but not extremely so. In the current model, this averaging does not occur, and the compliant interphase responds as it will. Due to its very low modulus (2 orders of magnitude less than the fiber and matrix), the fiber essentially appears to be a hole in the transverse response of the composite. This allows the appropriate knockdown to occur.

2.9 Concluding Remarks

An improved method for determining the elastic constants of a coated-fiber reinforced composite has been discussed. This method explicitly models the coating and considers all constituents at once, rather than relying on nested methods that treat the coated fiber as one phase with smeared

coating/fiber properties. Further, the method described avoids inaccuracies introduced by boundary conditions be embedding the constituent cylinders within a medium possessing the composite properties, effectively providing mixed boundary conditions. The improved accuracy of the new method is especially highlighted in the case of the transverse properties, where the effects of the explicit coating phase are properly considered. The nested method provides an estimate which is nearly 25% lower than the experimentally determined value, compared to a 12% underestimate provided by the new method, a reduction in the error of nearly 50%.

CHAPTER 3

Shear-Lag Model for Progressive Longitudinal Cracking

3.1 Introduction

Fiber-reinforcement of ceramic matrices provides enhanced fracture toughness through crack deflection and fiber pullout. These mechanisms are driven in large part by the behavior of a weak interphase coating of substantial thickness relative to the fiber diameter, and allow for substantial matrix cracking to accumulate before catastrophic failure of the composite. Therefore, to understand the response of these material in the post-failure regime, one must properly account for load transfer between the fiber and matrix via the soft interphase and how this load transfer affects, and is affected by, high-density matrix cracking and fiber debond.

One choice of architecture for these composites is a cross-ply laminate with straight, continuous fibers. This architecture has favorable in-plane properties as compared to woven laminates, and are considerably easier to manufacture with low porosity [35]. The damage progression under uniaxial tension in these composites is: 1) elastic deformation, 2) cracking of the transverse plies, 3) matrix cracking within the longitudinal plies, 4) failure of longitudinal fibers, and 5) pullout of the cracked fibers from the matrix [36]. These mechanisms persist also at elevated temperature, albeit, with the coating the mechanics of the process, [14]. There are several models available for predicting the effects of cracking in the transverse plies, such as the well-known model developed by Aveston, Cooper, and Kelly, (ACK model) [37] as well as models for cracking of the longitudinal plies that assume an interphase of negligible thickness [6]. There are also several models which predict the cracking of longitudinal plies where the interphase is not considered [38, 16]. However, the damage accumulation within the longitudinal plies is important for capturing the late deformation behavior, as well as allowing for models for fatigue, creep, and oxidation within the plies to be properly applied. While it is possible to develop numerical models to capture longitudinal ply cracking [39], this necessitates the use of 3-dimensional models, which are computationally expensive when applied to a multiscale modeling methodology.

There are several concentric cylinder-based models that predict various aspects of composite behavior related to the problem at hand. Numerous three-phase models have been presented that deal with the thermoelastic properties and response of the composite [40, 41]. There are also many models that predict the progressive damage response of two-phase composites, where the effects of the interphase are not considered explicitly [42, 38, 18, 16]. Further, much of the available literature considers only one of the two mechanisms (i.e. *only* progressive cracking or *only* fiber debond [42, 18]). Other models consider the effects of pullout on a single crack progressing through a wide specimen [6]. However, analytical models that predict progressive cracking where the interphase is *explicitly* considered have not been available. The effects of the interphase can alter the stress distribution in the cylindrical assembly and make subsequent effective stiffness of the cracked composite. As will be shown, this effect is less important when the interphase is thin in comparison to the fiber radius. However, the effects become more pronounced as the interphase becomes thicker.

To this end, a model comprising 3 concentric cylinders representing the fiber, interphase, and matrix is proposed and analyzed to capture the deformation response of a longitudinal ply in a cross-ply CMC. The explicit inclusion of the interphase is a key contribution of this work. Scanning electron microscopy reveals that the interphase thickness can be a substantial fraction of the fiber radius (often as thick as 3 or more microns on a 5-7 micron radius fiber [35]. A shear-lag approach is taken to describe the load transfer via interphase shear, similar to the approach taken in two-phase materials with soft matrices [43]. An energetical argument is used to drive the progressive cracking of the matrix and the extension of debond cracks along the fiber length. Similar ideas have been proposed for considering laminate cracking at the laminate level [44, 45], and reduced models have been considered for two-phase composites [37, 6, 46, 45], but have not been applied at the constituent level for three-phase composites. While it is acknowledged that extreme values dictate damage and failure, in the present work, the salient critical quantities used as inputs to the model are treated as being deterministic, with the task of including probabilistic descriptions left for future work [47]. The analytical nature of the proposed model will reduce computational cost when used in a multiscale approach [48] to study multi-directional CMC laminates (such as cross-ply laminates).

3.2 Equilibrium Equations

Consider a 3-phase fiber reinforced composite, comprising a fiber, a finite thickness coating, and a matrix, as representing the mechanics of a longitudinal ply in a CMC [32]. Let the geometry and tractions be defined as shown in the free-body diagram in Figure 3.1.

The following assumptions are made regarding the stress state in the material:

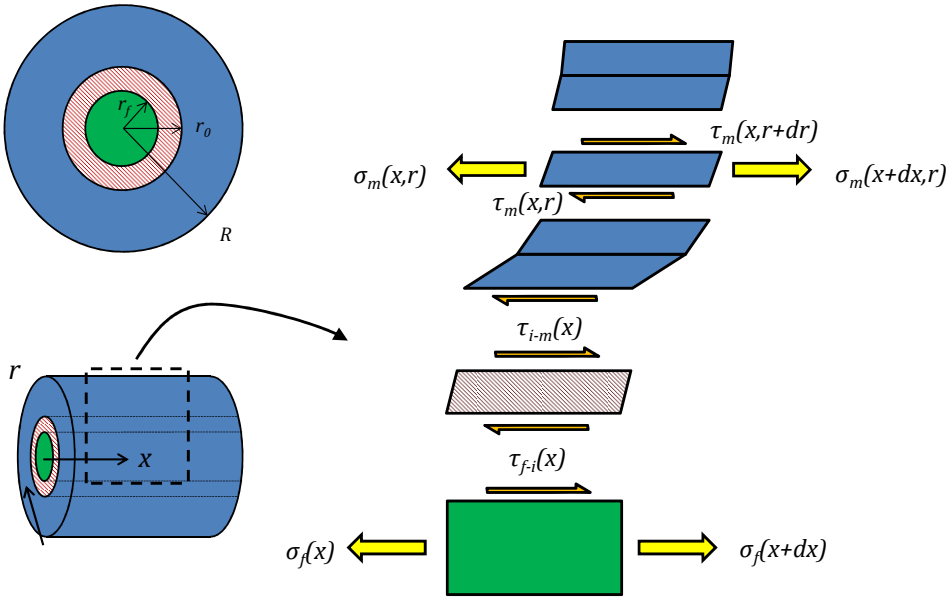

Figure 3.1: Tractions acting on differential chunks of length dx of the three constituents

1. The model is axisymmetric

2. The fiber carries only axial stresses which are constant in the radial direction.

3. The coating carries only shear stress.

4. The matrix carries both axial and shear stresses.

5. All other stresses are assumed to be negligible.

Equilibrium in the fiber can be expressed as

$$\frac{d\sigma_f}{dx} = -\frac{2}{r_f}\tau_{i-f}(x) \tag{3.1}$$

where $\tau_{i-f}(x)$ is the interfacial shear between the fiber and the coating. Here, it is assumed that the axial stress in the fiber has no radial or circumferential dependence. Across the interphase, equilibrium is simply

$$\tau_{i-f}(x) = \tau_i(x, r_f) = \frac{r_0}{r_f}\tau_{i-m}(x) \tag{3.2}$$

where $\tau_{i-m}(x)$ is the interfacial shear between the matrix and the coating, r_0 is the outer radius of the coated fiber and r_f is the radius of the uncoated fiber. It is assumed that the shear stress in the coating has no circumferential dependence. Substituting this into Equation (3.1) gives.

$$\frac{d\sigma_f}{dx} = -2\frac{r_0}{r_f^2}\tau_{i-m}(x) = -2\frac{r_f}{r_0^2}\tau_i(x, r_0) \tag{3.3}$$

where $\tau_i(x, r_0) = \tau_{i-m}(x)$ is used. In the matrix, the relevant equilibrium equation is

$$\frac{d\sigma_m(x,r)}{dx} + \frac{1}{r}\tau_m(x,r) + \frac{d\tau_m(x,r)}{dr} = 0 \tag{3.4}$$

where the axial and shear stresses in the matrix are assumed to have no circumferential dependence. Now, a separation of variables approach is taken to solve Eqn. (3.4), letting $\sigma_m(x,r) = S_X(x)S_R(r)$ and $\tau_m(x,r) = T_X(x)T_R(r)$. Further, it is assumed that $T_R(r) = \left(\frac{1}{r}\frac{R^2 r_0}{(R^2 - r_0^2)} + r\frac{r_0}{r_0^2 - R^2}\right)$. This form is chosen such that $T_R(r) = 1$ at the matrix-coating interface and vanishes at the outer radius of the matrix sheath. Substitution into and subsequent rearrangement of Eqn (3.4) yields,

$$-\frac{1}{T_x}\frac{dS_x}{dx} = \frac{1}{S_R}\left(\frac{1}{r}T_R + \frac{dT_R}{dr}\right) = \lambda_n \tag{3.5}$$

Using the above form of $T_R(r)$ and the second of Eqns (3.5), one can solve for S_R.

$$S_R = \frac{1}{\lambda_n}\left(\frac{(R^2 - r^2)r_0}{r^2(R^2 - r_0^2)} - \frac{(r^2 + R^2)r_0}{r^2(R^2 - r_0^2)}\right) \tag{3.6}$$

Enforcing continuity of tractions at the matrix-coating interface in the separated form of the shear stress yields

$$\tau(x, r = r_0) = T_X(x)T_R(r = r_0) = T_X(x) = \tau_i(x, r_0) \tag{3.7}$$

Combining this result with the first of Eqns (3.5) and Eqn (3.1) gives

$$\frac{dS_X}{dx} = -\frac{\lambda_n}{2}\frac{r_f^2}{r_0}\frac{d\sigma_f}{dx} \tag{3.8}$$

Integrating Eqn. (3.8) yields,

$$S_X = -\frac{\lambda_n}{2}\frac{r_f^2}{r_0}\sigma_f + C \tag{3.9}$$

where C is a constant of integration.

3.3 Compatibility

At the matrix-coating interface, the axial displacement of the matrix can be expressed in terms of a partial contribution from the axial extension of the fiber and a contribution from the shear strain in the coating. The shear strain in the interphase can be written as

$$\gamma_i(x, r) = \frac{\partial u_i}{\partial r} + \frac{\partial v_i}{\partial x} \approx \frac{\partial u_i}{\partial r} \tag{3.10}$$

where u_i and v_i are respectively the axial and radial displacements of the interphase. Here it is assumed that the coating thickness does not vary under deformation. Further, since the interphase is much softer than the fiber and matrix, the contribution to displacement due to shearing of the interphase can be approximated by (solution given in the Appendix)

$$u_i^{shear}(x) = \bar{\gamma} t_i = \frac{5}{6}\frac{\tau_i(x)}{G_i}\frac{(r_0^3 - r_f^3)}{r_0^2} \tag{3.11}$$

where $\bar{\gamma}$ is the average shear strain across the coating, t_i is the coating thickness, and G_i is the shear modulus of the coating. Further, the axial displacement of the coating also contributes due to the axial strain in the fiber. This contribution may be expressed as

$$u_i^{axial}(x) = \int_0^x \epsilon_f(\hat{x})d\hat{x} \tag{3.12}$$

Finally, the axial displacement of the matrix can be expressed as

$$u_m(x, r_0) = u_i(x, r_0) = u_i^{axial}(x) + u_i^{shear}(x) = \int_0^x \epsilon_f(\hat{x})d\hat{x} + \bar{\gamma}t_i \tag{3.13}$$

This same displacement can also be expressed in terms of the axial extension of the matrix along the matrix-coating interface. Expressed in this form, the displacement is

$$u_m(x, r_0) = \int_0^x \epsilon_m(\hat{x})d\hat{x} \tag{3.14}$$

Eqns (3.13) and (3.14) provide an integral form of compatibility in this problem. Setting $u_m(x, r_0)$ from Eqn (3.13) equal to $u_m(x, r_0)$ from Eqn (3.14) and solving for the interfacial stress yields

$$\tau_i(x, r_0) = \frac{6G_i r_0}{5G_m\left(r_f^3 - r_0^3\right)}\left(G_m r_0 \int_0^x \left(\frac{\sigma_f(x)}{E_f}\right) dx + G_m r_0 \int_0^x \frac{r_f^2\left(\phi + \sigma_f(x)\right)}{2E_m r_0^2}\, dx\right) \tag{3.15}$$

3.4 Governing Equations

Using $\gamma = \frac{\tau_m}{G_m}$, $\epsilon = \frac{\sigma_m}{E_m}$ and the separated form of the stress solution from Eqn (3.5), we can express this in terms of stresses. We can further use the results of Eqns (3.7) and (3.8) to obtain

$$\tau_i(x, r_0) = \frac{G_m(n-1)\left(-u(x, R) + u(x, r_0) + \frac{(n-1)\left(R - r_0 V_{cf}^{n/2}\right)\int_0^x \frac{S_X(x)}{E_m}\, dx}{E_m R r_0 \lambda_n}\right)}{-r_0 + R V_{cf}^{n/2}} \tag{3.16}$$

and

$$\sigma_f''(x) = -6\frac{G_c G_m R}{\alpha}\left(E_f r_0^2 S_x(x) + E_m r_0^3 \lambda \sigma_f(x)\right) \tag{3.17}$$

Substituting Eqn (3.9) will yield a 2nd order ODE for σ_f.

$$\sigma_f''(x) = -\frac{G_c G_m R}{\alpha}(6E_m r_0^3 \lambda \sigma_f(x) + 3E_f r_0 r_f^2 \lambda \sigma_f(x) + 6E_f r_0^2 \phi_1) \tag{3.18}$$

where $\alpha = \lambda\frac{E_f E_m}{G_c} r_f^2(-6r_0^3 R - 5G_m^* r_0^3 R + 6r_0^4 + 5G_m^* r_f^3 R)$, and $G_m^* = \frac{G_m}{G_c}$

The solution of this ODE can then be substituted into Eqns (3.8) and (3.15) to obtain the (somewhat lengthy) expressions for the shear and normal stresses in the matrix and interphase.

3.5 Boundary Conditions

Assume that the cylinder is uniformly cracked, with a crack spacing of $2h$, as shown in Figure 3.2.

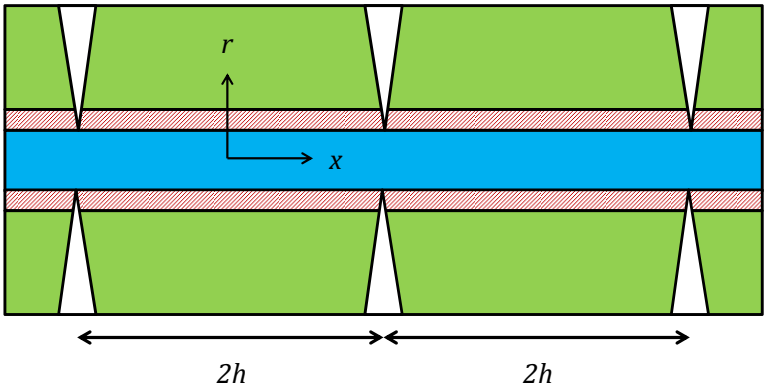

Figure 3.2: Matrix cracks in the composite. Note that the problem is periodic in the axial direction.

In the present formulation, the composite is subjected to a far field applied strain, ϵ^c. It is assumed in the current formulation that the fibers remain uncracked, and therefore the average strain along the fiber must equal the applied composite strain, which can be expressed as

$$\begin{aligned} \int_0^{-h} \epsilon_f dx = \int_0^{-h} \frac{\sigma_f}{E_f} dx = \epsilon^c h \\ \int_h^{0} \epsilon_f dx = \int_h^{0} \frac{\sigma_f}{E_f} dx = \epsilon^c h \end{aligned} \tag{3.19}$$

At the crack faces, the matrix cannot support any stress. The boundary conditions at these faces are

$$\sigma_m(x = h, r) = \sigma_m(x = -h, r) = 0 \tag{3.20}$$

Eqn (3.20) will provide the constant C in Eqn (3.9), and Eqn (3.19) will provide the constants of integration in the general solution to (3.18).

3.6 Progressive cracking

The solution in the preceding section provides the stress and strain distributions in a unidirectional composite with some known crack density and subjected to some applied strain. To determine the crack density associated with a given state of applied strain, an energy based criterion is used. Using the above solution, and keeping h as a parameter of the problem, the average strain energy per unit length can be obtained as,

$$U_c = U_f + U_i + U_m = \int_{-h}^{h} \int_A \frac{1}{2} \left(\frac{\sigma_f(x)^2}{E_f} + \frac{\tau_i(x,r)^2}{G_i} + \frac{\sigma_m(x,r)^2}{E_m} + \frac{\tau_m^2}{G_m} \right) dA dx \tag{3.21}$$

Additionally, the work of fracture that must be overcome to provide cracks at a spacing $2h$ can be expressed as

$$\Delta W = \frac{1}{2h} G_{Ic_m} A_m \tag{3.22}$$

The total energy associated with an applied strain, ϵ_c and a crack spacing, h, is therefore given by

$$\Phi = U_c + \Delta W \tag{3.23}$$

From this result, a minimum energy configuration can be obtained, yielding the energetically favorable crack spacing for a given applied strain, ϵ_c. Using the solution from the previous section, it is trivial to determine the resultant composite stress, allowing for a stress-strain response to be generated. It should be noted that this framework does not consider the effects of preexisting cracks or cracks that may have occurred earlier in the loading cycle. However, so long as the crack spacing remains sufficiently large compared to any characteristic length of the microstructure, crack interaction effects are small, and the obtained crack density can be considered as an average crack density over a sufficiently large structure (such as a tensile coupon).

3.6.1 Initiation of cracking

The preceding analysis focused on determining the accumulation of additional cracks in a longitudinal ply that has some existing crack density. To determine the level of strain at which the first

cracks are initiated, an energy based procedure is adopted. In this case, an existing crack spacing is assumed to be infinitely large, such that only a small region near one of the crack faces is of interest. Within this region, the strain (and stress) fields can be considered to be a superposition of the strain (or stress) field in the uncracked material and the perturbation caused by the existence of the crack, which leads to a perturbed strain energy, δU. When the perturbed energy released exceeds the energy required to overcome the work of fracture for a single annular crack, then it is assumed that cracking has initiated.

$$U_{cracked}^{composite} = U_{uncracked}^{composite} - \delta U \tag{3.24}$$

where δU is a positive quantity. It is this energy deficit that is of interest. We then seek the level of strain such that energy deficit due to the perturbation is sufficiently large to overcome the work of fracture, i.e.

$$\delta U > G_{Ic_{matrix}} A_{matrix} \tag{3.25}$$

3.7 Fiber Pullout

3.7.1 Frictionless Debond

Consider, now, a cracked composite where the fiber is allowed to debond from the matrix through Mode II cracking of the coating. From stress analysis of the concentric cylinder mode shown in Section 8, it is known that the shear stress in the coating is highest near the crack faces in the matrix. Therefore, cracking within the coating will initiate at the ends ($x = \pm h$). The pullout is handled in conjunction with the matrix cracking in the following manner: Suppose a composite is subjected to a strain ϵ, resulting in a crack spacing $2h$ as per the preceding analysis. Holding the strain and crack spacing constant, the maximum magnitude of shear stress in the coating is determined. If this stress is higher than some critical shear stress, then a debond crack is permitted to initiate, and the composite is considered to have the configuration shown in Figure 3.3.

In this model, it is assumed that frictional load transfer between the matrix and fiber across the debond crack is small and can be neglected. Because the matrix in the region $h-\delta < x < h$ cannot be loaded, the area can be neglected from further consideration, and the debonded configuration can be approximated by the configuration shown in Figure *. In this configuration, in the debond region, only the fiber can carry any stress, and the stress state in this region is constant. In the bonded region, load transfer still occurs between the fiber and matrix via shear transfer through the coating, and this region can be represented by a foreshortened concentric cylinder identical to the model in Section 3.5. In this configuration, no stress concentration is considered at the tip of the

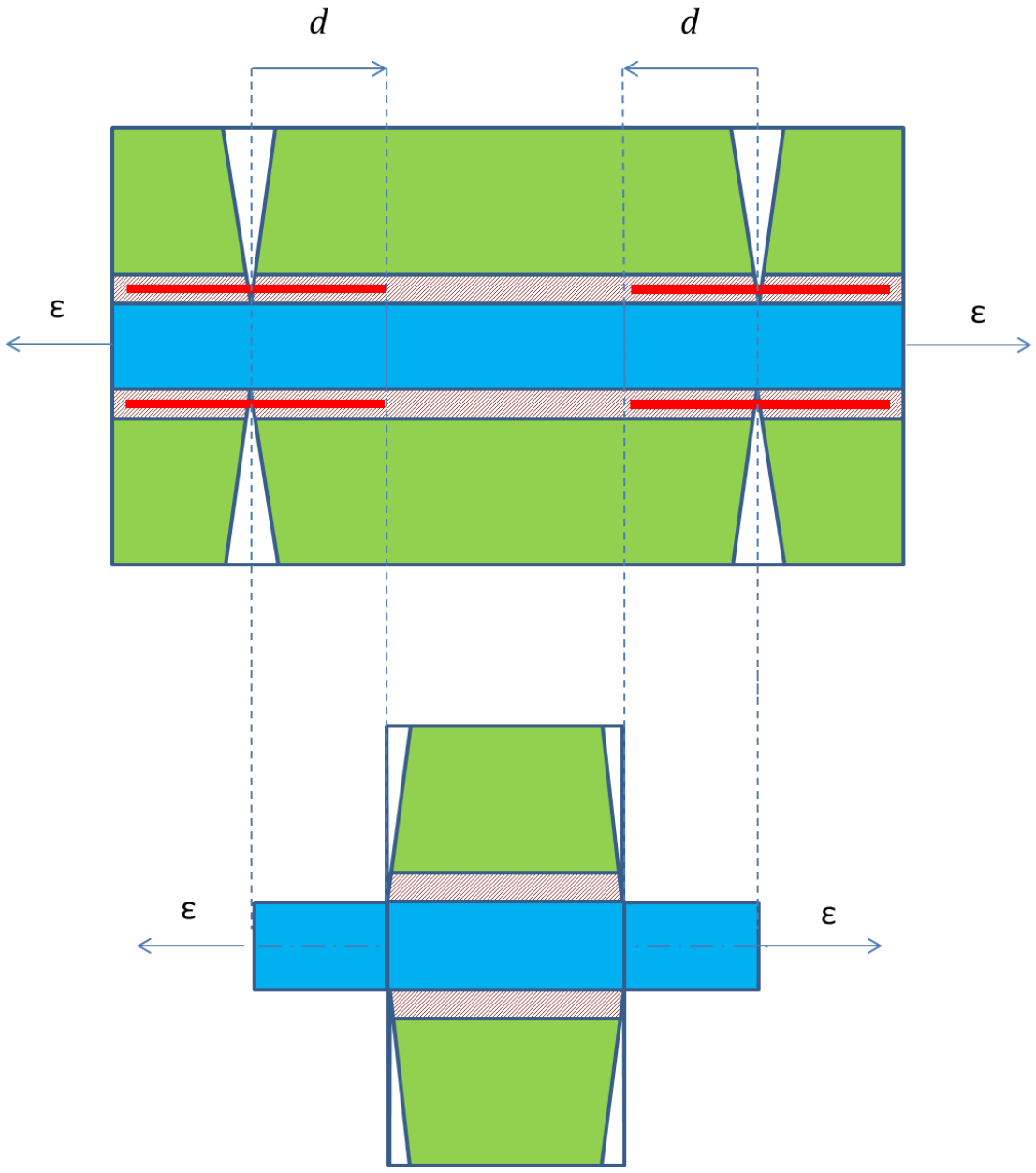

Figure 3.3: Configuration assumed for computing stresses and effective stiffness in the case of fiber debond. Since the region of matrix between the face of the matrix crack and the tip of the debond crack cannot receive any load from the fiber, it is disregarded, and the composite is treated as a combination of free fiber and a shortened region of still-bonded composite in series. Note that the problem is periodic in the axial direction.

debond crack except as a modification to the critical shear stress that would need to be overcome in order to progress the debond.

3.7.2 Solution of the debonded fiber problem

With respect to the configuration in Figure 3.2, subjected to a far field axial strain, ϵ^c, and assuming that the fibers remain uncracked, the composite strain must be equal to the average fiber strain taken along the entire length of the fiber, which can be represented as

$$\begin{aligned} \int_0^{-h} \epsilon_f dx = \int_0^{-(h-\delta)} \frac{\sigma_f^{bond}}{E_f} dx + \delta \frac{\sigma_f^{debond}}{E_f} = \epsilon^c h \\ \int_h^0 \epsilon_f dx = \int_{h-\delta}^0 \frac{\sigma_f^{bond}}{E_f} dx + \delta \frac{\sigma_f^{debond}}{E_f} = \epsilon^c h \end{aligned} \tag{3.26}$$

In the debond region, only the fiber carries axial stress, and this stress is constant in the axial direction.

In the bonded region, the same equilibrium equations as given in Section 3.5 apply in all three constituents.

$$\begin{aligned} \frac{d\sigma_f}{dx} &= -\frac{2}{r_f}\tau_{i-f}(x) \\ \tau_{i-f}(x)\tau_i(x, r_f) &= \frac{r_0}{r_f}\tau_{i-m}(x) \\ \frac{d\sigma_m(x,r)}{dx} + \frac{1}{r}\tau_m(x,r) + \frac{d\tau_m(x,r)}{dr} &= 0 \end{aligned} \tag{3.27}$$

A similar separation procedure as before is used to solve the set of Eqns. (3.27). Now, the matrix in the debond region carries no axial stress, leading to the no-stress condition at the axial location of the debond crack tip, $\pm(h-\delta)$.

$$\sigma_m(x = h - \delta, r) = \sigma_m(x = -(h-\delta), r) = 0 \tag{3.28}$$

The matching condition on the fiber stress at the boundary between the bonded and debonded regions is

$$\begin{aligned} \sigma_f^{debond} &= \sigma_f^{bonded}(x = h - \delta) \\ \sigma_f^{debond} &= \sigma_f^{bonded}(x = -(h - \delta)) \end{aligned} \tag{3.29}$$

Solving the problem with these modified boundary conditions provides the stress/strain state for a given matrix crack density, fraction of debonded fiber, and applied composite strain.

3.8 Combined matrix cracking and fiber debond

To determine the composite response with both matrix cracking and fiber debonding active, the following procedure is used. Starting from an initial assumption of infinitely sparse matrix cracks and zero fiber debond, an increment of strain is applied. First, matrix cracking is checked. Given the current configuration and strain level, the energetically favorable crack spacing is determined. In the routine, this is checked against the current crack spacing: no healing is allowed. After the crack spacing has been determined, then the fiber debond condition is checked. A combined strength/energy approach is used to drive the debond. The maximum interfacial shear stress is determined, and if it exceeds a critical value, then the debond is allowed to grow. Given that debonding is permitted to progress, the debond length, δ, which is a parameter of the problem, the energetically favorable increase in debond length is determined. The debond fraction, defined as the ratio of debond length to crack spacing, is checked: no reduction in the debond fraction is allowed, since healing is not admissible.

It should be noted that it is the debond *fraction* that is conserved, not the absolute debond *length*. As the matrix crack density increases (decreasing matrix crack spacing), the absolute debond length will actually be reduced, unless the progression routine results in an increase in debond fraction. This is due to a limitation of the model that cracks are assumed to be uniformly spaced, and that the model invokes symmetry and periodicity. In other words, if absolute debond length were conserved, then all new cracks would necessarily initiate fully developed debond cracks of their own, causing the fiber to prematurely become completely debonded.

3.9 Frictional Debond

To account for frictional sliding in the debond crack, it is assumed that a constant frictional force less than the coating shear strength is active over the entire debond length. Note that this approach is only valid for monotonic loading at this time. The boundary conditions and equilibrium equations are the same as for the frictionless debond case, with the exception that the equilibrium equation in the debond region is now

$$\begin{aligned} \frac{d\sigma_f}{dx} &= -\frac{2}{r_f}\tau_{i-f}(x) \\ \tau_{i-f}(x)\tau_i(x,r_f) &= \frac{r_0}{r_f}\tau_{i-m}(x) \\ \frac{d\sigma_m(x,r)}{dx} + \frac{1}{r}\tau_m(x,r) + \frac{d\tau_m(x,r)}{dr} &= 0 \end{aligned} \tag{3.30}$$

3.10 Results and Discussion

Figure 3.4 shows the predicted response curve for a unidirectional laminate as predicted by both the ACK model [37] and the present work. The same geometric and material properties are used in each model. As can be seen in the figure, the ACK model provides a good general response, but does not capture the apparent "'strain-hardening-like"' behavior that is captured by the current model. The increase in load-carrying capability in the shear lag model is primarily due to the frictional load transfer in the debonded region of the coating - a mechanism not present in the simpler ACK model.

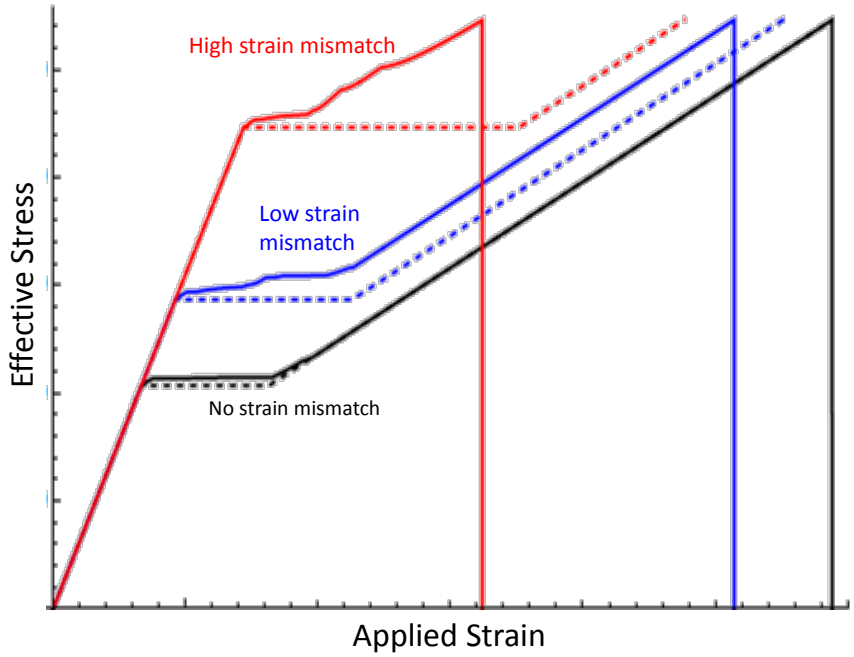

Figure 3.4: Comparison between current model and ACK [37] model for a unidirectional SiC/SiC laminate for various levels of strain-mismatch between the fiber and matrix. Solid lines denote the current model, dashes denote ACK.

3.10.1 Effects of frictional sliding

The addition of frictional sliding in the model causes two major, competing effects on the lamina response. First, increasing the magnitude of the frictional traction decreases the maximum shear stress in the bonded region of the interphase, delaying interphase cracking and reducing debond length. Taken alone, this reduction of damage causes an increase in instantaneous effective modulus and leads to a stiffer overall composite response. However, the increase in friction also leads to an increase in load transfer from the fiber to the matrix. This causes the stress in the matrix to increase, allowing matrix cracking to occur earlier and leading to an increase in crack density and

a subsequent decrease in instantaneous effective modulus. The results of this competition can be seen in Figure 3.5.

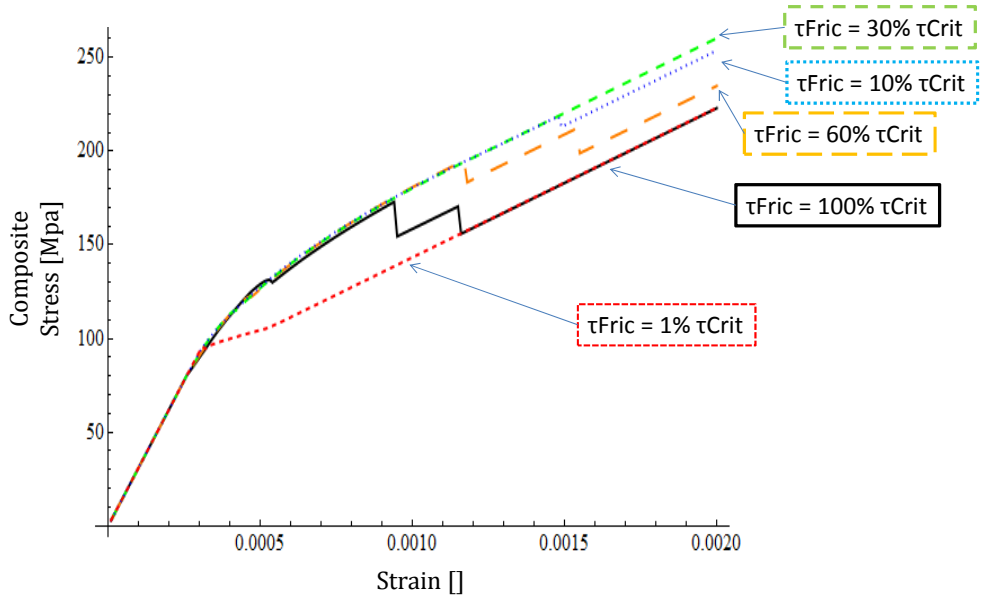

Figure 3.5: The effects of increased friction (enhanced load transfer and reduced debond length) have competing effects on the effective stress-strain curve of the lamina.

In the figure, an increase in the frictional constant initially leads to an increase in the post-proportional limit load carrying capability of the lamina, due to reduced debond, until a maximum response is reached. After this, further increase of the frictional constant leads to a decrease in load carrying capability due to an increase in matrix crack density. Although the effect of sliding friction can be seen to have important effects on the lamina response, it is nonetheless a difficult property to measure. It is perhaps best measured using fiber push-in or pull-out tests, where possible. However, in the absence of the capability to perform these measurements, it would be possible to back this property out of laminate tests, provided good data could be independently obtained on the other mechanical and failure properties of the constituents (i.e. moduli, strengths, and toughnesses).

3.10.2 Effects of the Explicitly Modeled Coating

Several models exist for predicting the cracking of brittle matrix laminates where only two phases (i.e. fiber-matrix) are considered[42, 38, 18, 16]. In these models, it would be necessary to consider an "'equivalent coated fiber"', and thus recursively construct the composite[49]. The plot shows the effective stiffness as a function of crack density as predicted by one of these models as well as that by the current work.

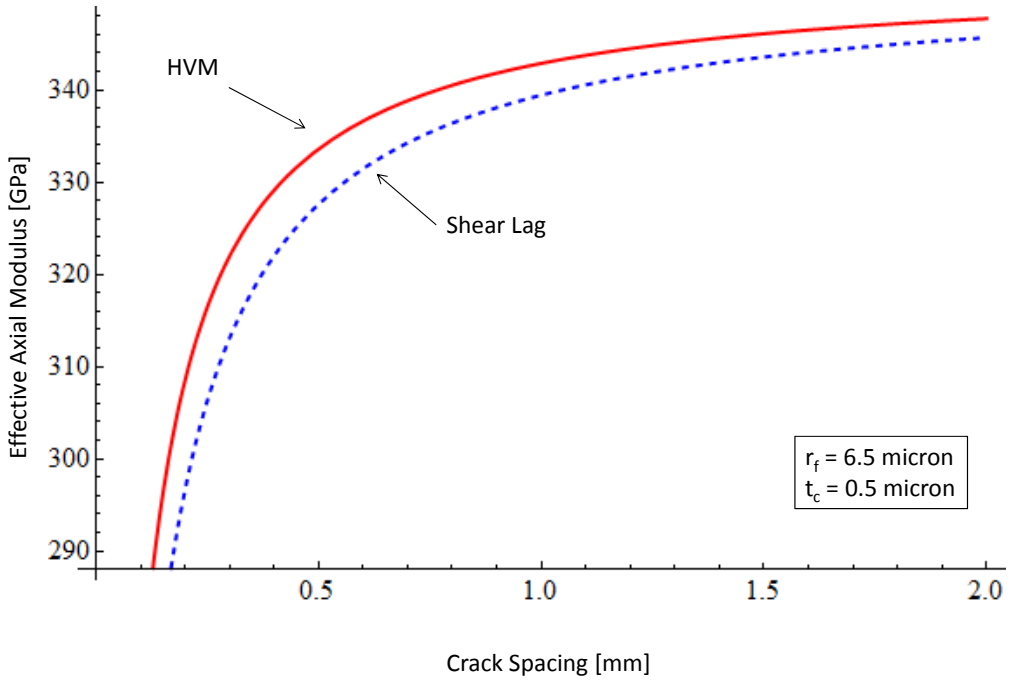

Figure 3.6: Comparison between the current work and an equivalent two-phase model with a thin coating

As can been seen in the Figures 3.6 and 3.7, in the case of a thin coating, the homogenized fiber model is in close agreement with the current work. However, when the coating thickness becomes large compared to the fiber radius, the result diverges significantly. This highlights the importance of explicitly modeling the coating, regardless of the crack progression scheme, for cases where the interphase becomes comparatively thick.

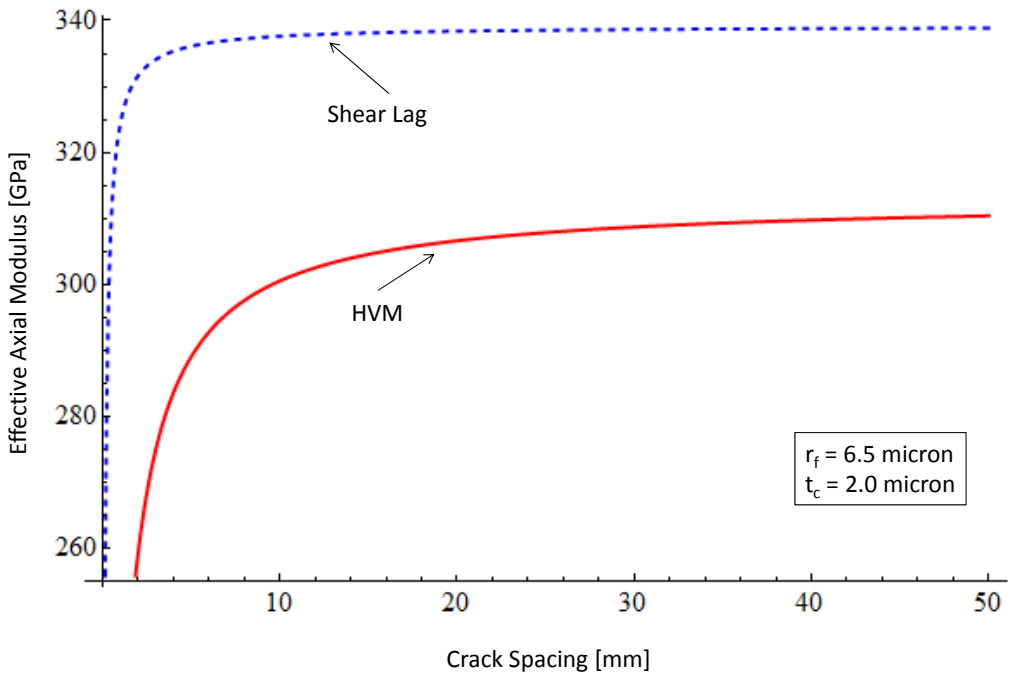

Figure 3.7: Comparison between the current work and an equivalent two-phase model with a thick coating

3.11 Concluding Remarks

In the current work, an approach is given to determine the stress-strain response of a 3-phase lamina within a brittle matrix composite. The current approach is novel in that it includes the effects of a thick interphase that experiences frictional sliding during the fiber pullout process. This work could be incorporated into a multiscale modeling approach as a material model for the longitudinal plies within an analytical laminate cracking model, or as behavior within a multiscale/finite element modeling approach. Although the current approach is tailored to continuous fiber composites, the ideas could be used for short fiber composites by applying the appropriate initial geometry and boundary conditions at the ends of the fiber. Future work on this topic will include the implementation of stochastic methods to simulate the variable nature of brittle matrix composites and the extension of this work to multiaxial stress states.

CHAPTER 4

Multiscale Simulations of CMCs: Combining Finite Element Analysis and the Generalized Method of Cells

4.1 Introduction

Accurately predicting the behavior of CMCs under mechanical load is complicated by the several mechanisms of failure present in this class of materials. "'Smeared"' analyses (ply-level or completely homogenized) may be adequate for linear stress analysis of parts during the design phase, but the variety of failure mechanisms under different loading and environmental cases may lead to a requirement for higher fidelity models. Modeling every fiber in a part would be computationally expensive and only feasible for very small volumes of material. Multiscale modeling techniques offer a compromise between physical fidelity and computational feasibility [50, 48].

In practical usage, any multiscale approach must be built within a commercially available finite element program. Within this framework, a separate micromechanical model is implemented as a material model within the finite element program. The current study comprises a two-scale concurrent multiscale framework. The coupon scale is modeled using ABAQUS 6.11 finite element software [51]. The micro-mechanics are modeled using the Generalized Method of Cells (GMC) [52, 53]. The suite used for the multiscale analysis is the MAC/GMC suite developed and distributed by NASA Glenn Research Center. MAC/GMC is coupled with ABAQUS via FEAMAC, also available from NASA Glenn Research Center [54]

In this framework, a representative unit cell is placed at each integration point within the finite element analysis. At the finite element level, the load is incremented and the incremental strain on each element is computed, using the stiffness matrices from the previous iteration. These strains are then passed from ABAQUS to MAC/GMC, where they are applied as boundary conditions in the microscale domain. Then, within MAC/GMC, the subcell stress and strain states are computed, with any local constitutive or damage laws being taken into account. Once the subcell strains and

stresses are known, MAC/GMC is then able to compute the average "'composite"' incremental stress and the incremental Jacobian matrix for that integration point. The incremental stress and Jacobian are then passed from MAC/GMC to ABAQUS. Once this process has been performed for all integration points, ABAQUS can then compute the global stiffness matrix and proceed to the next iteration. This procedure is outlined in Figure 4.1.

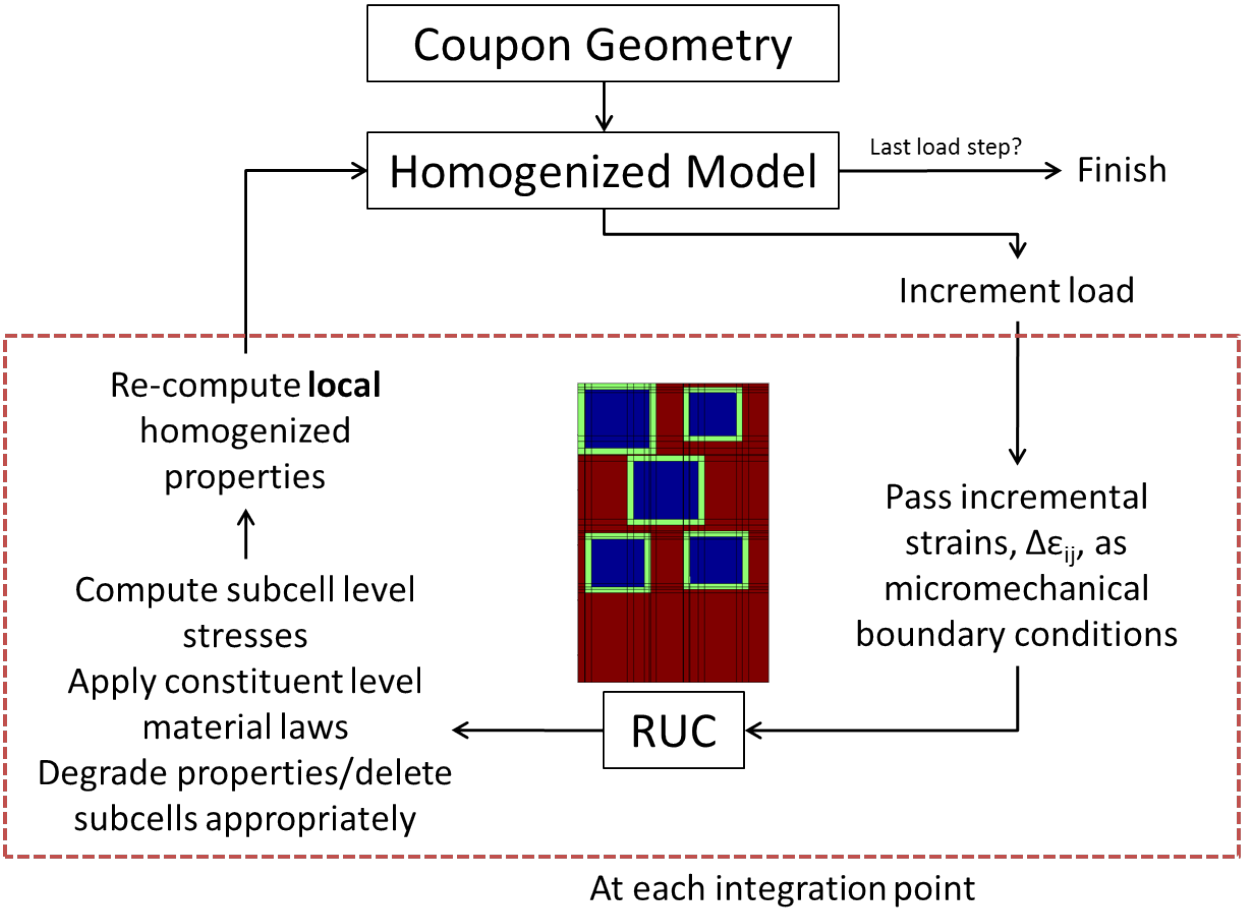

Figure 4.1: Process diagram for FEA/GMC modeling used in this research.

4.1.1 Overview of the Generalized Method of Cells

GMC is a numerical method originally devised for estimating the elastic constants of continuous fiber-reinforced composites [52], as the Method of Cells (MOC). In the original method of cells, the composite it assumed to be represented by a 2x2 rectangular array of cells, making up the Representative Unit Cell (RUC), as shown in Figure 4.2. This array is assumed to be periodic. The method of cells was quickly expanded to apply to more general rectangular arrays, allowing for a finer representation in fiber shape, or for the inclusion of multiple fibers for the purposes

of investigating fiber size or packing effects [39]. The method was also expanded to allow for three-dimensional subcells for characterizing particle-reinforced or short fiber composites. This extension is called the generalized method of cells

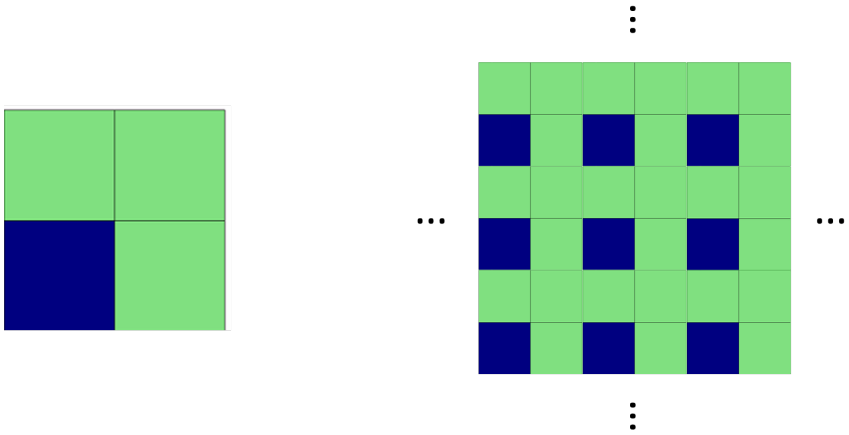

Figure 4.2: The 2x2 rectangular array used to represent the representative unit cell of an FRC in the original Method of Cells (left). The infinite array represented by this RUC (right). This RUC represents a 25% fiber volume fraction unidirectional composite.

A detailed derivation of the GMC equations can be found in [48]; a summary is provided here for context. In the GMC formulation, the displacement field within each subcell is assumed to be linear, resulting in constant stress and strain fields within each subcell. Additionally, continuity of displacements and tractions across subcell boundaries is enforced only in an average sense along the boundary. This is in contrast to node-based discretizations (such as the finite element method) where continuity is enforced exactly at the nodes. The displacement field is thus given by Equation 4.1.

$$u_i^{(\beta\gamma)} = w_i^{(\beta\gamma)} + \bar{x}_2^{(\beta)}\phi_i^{(\beta\gamma)} + \bar{x}_3^{(\gamma)}\psi_i^{(\beta\gamma)}, i = 1, 2, 3 \tag{4.1}$$

where $w_i^{(\beta\gamma)}$ is the displacement at the center of subcell $(\beta\gamma)$ in the x_i direction, and $\phi_i^{(\beta\gamma)}$ and $\psi_i^{(\beta\gamma)}$ are microvariables describing the displacement field in the cell coordinates $\bar{x}_2^{(\beta)}$ and $barx_3^{(\gamma)}$. The definition of linear strain [34] is applied.

$$\epsilon_{ij}^{(\beta\gamma)} = \frac{1}{2}(\partial_i u_j^{(\beta\gamma)} + \partial_j u_i^{(\beta\gamma)}) \tag{4.2}$$

In each subcell, a constitutive law is applied, which is linearized about the current state, as shown in Equation 4.3

$$\sigma_{ij}^{(\beta\gamma)} = \mathbf{C}_{ijkl}^{(\beta\gamma)}(\epsilon_{kl}^{(\beta\gamma)} - \epsilon_{kl}^{T(\beta\gamma)}) \tag{4.3}$$

where $\epsilon_{kl}^{T(\beta\gamma)}$ is the thermal strain in subcell $\beta\gamma$.

Displacement continuity is enforced in an average sense across the boundaries of the subcell. Taken together with the periodicity requirement, displacement continuity can be stated in terms of the displacement microvariables, as in Equations 4.4 and 4.5.

$$w_i^{(\beta\gamma)} + \frac{1}{2} h_\beta \phi_i^{(\beta\gamma)} = w_i^{(\hat{\beta}\gamma)} + \frac{1}{2} h_{\hat{\beta}} \phi_i^{(\hat{\beta}\gamma)} \tag{4.4}$$

$$w_i^{(\beta\gamma)} + \frac{1}{2} l_\gamma \psi_i^{(\beta\gamma)} = w_i^{(\beta\hat{\gamma})} + \frac{1}{2} l_{\hat{\gamma}} \psi_i^{(\beta\hat{\gamma})} \tag{4.5}$$

where $\hat{\beta}$ and $\hat{\gamma}$ are given by Equations 4.6 and 4.7.

$$\hat{\beta} = \begin{cases} \beta + 1, \beta < N_\beta \\ 1, \beta = N_\beta \end{cases} \tag{4.6}$$

$$\hat{\gamma} = \begin{cases} \gamma + 1, \gamma < N_\gamma \\ 1, \gamma = N_\gamma \end{cases} \tag{4.7}$$

Using Equation 4.2, Equations 4.4 and 4.5 can be stated in terms of the subcell strains. These can then be assembled into the matrix equation given in Equation 4.8

$$\boldsymbol{A}_G \epsilon_S = \boldsymbol{J} \bar{\epsilon} \tag{4.8}$$

where $\bar{\epsilon}$ is the global average strains of the RUC, ϵ_S contains the local subcell strains, $\boldsymbol{A}_G$ is the geometric and material influence matrices and $\boldsymbol{J}$ comes from enforcement of displacement continuity.

Traction continuity can be expressed as in Equations 4.9 and 4.10.

$$\sigma_{2j}^{(\beta\gamma)} = \sigma_{2j}^{(\hat{\beta}\gamma)} \tag{4.9}$$

$$\sigma_{3j}^{(\beta\gamma)} = \sigma_{3j}^{(\beta\hat{\gamma})} \tag{4.10}$$

Ultimately, Equations 4.9 and 4.10 are stated in terms of the subcell strains using Equations 4.3, stated in terms of the subcell strains. The results in Equation 4.11

$$\boldsymbol{A}_M \epsilon_S = 0 \tag{4.11}$$

where $\boldsymbol{A}_M$ is the material influence matrix. Finally, Equations 4.8 and 4.11 can be combined into

$$\tilde{\boldsymbol{A}}\epsilon_S = \boldsymbol{K}\bar{\boldsymbol{\epsilon}} \tag{4.12}$$

where

$$\tilde{\boldsymbol{A}} = \begin{bmatrix} \boldsymbol{A}_M \\ \boldsymbol{A}_G \end{bmatrix}$$

and

$$\boldsymbol{K} = \begin{bmatrix} \boldsymbol{0} \\ \boldsymbol{J} \end{bmatrix}$$

Now, the local subcell strains can be related to the globally applied strains through Equation 4.13

$$\boldsymbol{\epsilon}_S = \boldsymbol{A}\bar{\boldsymbol{\epsilon}} \tag{4.13}$$

where $\boldsymbol{A} = \tilde{\boldsymbol{A}}^{-1}\boldsymbol{K}$ is the strain concatenation matrix.

Finally, the instantaneous composite constituent law, $\boldsymbol{B}$ can be obtained from Equation 4.14

$$\boldsymbol{B} = \frac{1}{HL}\sum_{\beta=1}^{N_\beta}\sum_{\gamma=1}^{N_\gamma} h_\beta l_\gamma \boldsymbol{C}^{(\beta\gamma)}\boldsymbol{A}^{(\beta\gamma)} \tag{4.14}$$

where $\boldsymbol{A}^{(\beta\gamma)}$ is the submatrix of $\boldsymbol{A}$ relating the local strain in subcell $\beta\gamma$ to the global strain. In the multiscaling framework, $\boldsymbol{B}$ is the desired instantaneous constitutive law of the RUC that will be passed back to the finite element solver in each iteration.

4.2 Multiscale characterization of uniaxial tension

4.2.1 Residual stress in CMCs

Production of CMCs through melt-infiltration can lead to a strain mismatch during processing. The magnitude of this mismatch is affected by many parameters, including thermal expansion, phase transformation, chemical reactions, and creep during the manufacturing process. While an ideal analysis would be able to account for all of these mechanisms, many times information about the manufacturing procedure is unknown. Major information that may be unknown includes the behavior of precursor materials under creep or stress relaxation consideration and detailed knowledge about the heating and cooling cycles of process. Due to the complex nature of this processing, the current methodology attempts to capture the relevant effects of all of this through

an Effective Processing Strain (EPS) parameter. This parameter is taken as a combination of all of the unknown processing induced strain mismatch sources, and will be used to initialize a state of strain mismatch, and therefore residual stress, within the composite. This stress/strain state is then used as a starting point for determining the mechanical response of the as-received composite.

4.2.2 Simulation details

In the current work, the coupon is modeled in Abaqus using linear solid brick elements with reduced integration (C3D8R). Each ply of the laminate consists of a single layer of brick elements. The finite element mesh can be seen in Figure 4.3. The mesh contains 14,768 elements with a characteristic length of 0.550 mm in the gage section, which was determined to be converged for this problem.

Figure 4.3: Finite element mesh used at the coupon level

4.2.2.1 Random microstructure

Although in many composite analysis techniques, the microstructure is assumed to be periodic, in the real composite, this is not necessarily accurate. In the material used in this research, there is considerable spatial non-uniformity. In an attempted compromise between computational efficiency and accurate representation of this non-uniformity, a multiple-fiber RUC with spatial randomization is used. The microstructural model is represented as a five-fiber RUC, with fibers that are nominally hexagonally packed. To capture the effects of spatial non-uniformity of the composite, the nominal RUC has been perturbed to produce a library of randomized RUCs which are then applied randomly to the elements in the finite element model. The microstructural dimensions that are perturbed are the fiber radius, fiber center location, and coating thickness. For this work, a library of ten RUC was used. By varying the microstructure, the coupon is effectively seeded with weak points and imperfections, which will be shown to strongly affect the qualitative failure response of the material. A few examples of the randomized RUC can be seen in Figure 4.4. Note that the corners of the square fiber representation do not cause stress concentration to the fact that continuity and equilibrium are enforced along the boundaries of subcells in an integral sense, and not at the nodes as they would be in a finite element framework.

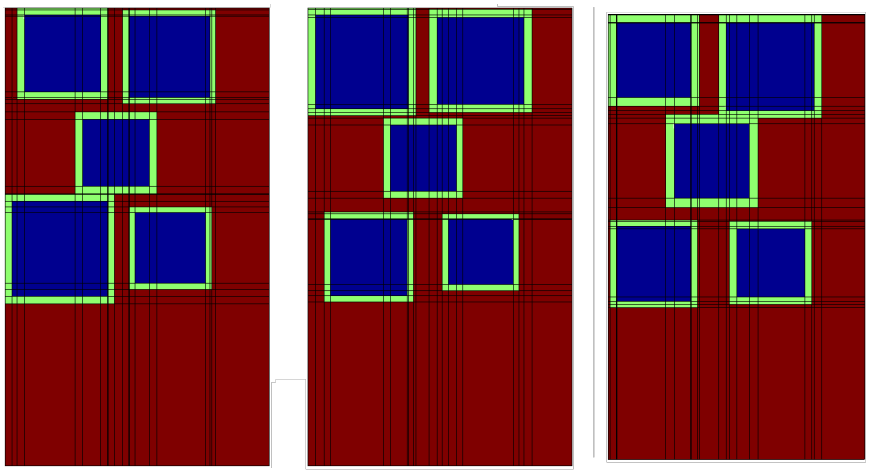

Figure 4.4: Examples of randomized RUCs used at the micromechanical scale.

4.2.2.2 Constituent elastic and failure properties

Both the fiber and the matrix are given a maximum principal stress failure criterion. For the fiber, a failure stress of 2600 MPa has been adopted from the literature [55, 56]. The matrix is also assigned a maximum principal stress criterion. Due to the dependence of strength on manufacturing conditions, the failure stress has been determined through a parametric study to be 300 MPa. For the interface, a maximum shear stress criterion is used. The elastic properties are given in Table 4.1.

The "'effective processing strain"' (EPS) is introduced with the modeling framework as a large, negative thermal expansion coefficient. The magnitude of the EPS is spread over a range of temperatures where these processing effects are relevant. For the fiber and interphase, the Coefficient of Thermal Expansion (CTE) is assumed to be constant throughout the entire simulation range.

Phase	Fiber	Matrix	Interphase
Young's Modulus (GPa)[MSI]	380	340	10
Poisson's Ratio	0.14	0.16	0.19

Table 4.1: Elastic material properties used for simulation of "'old-process"' batch material under uniaxial tension

4.2.3 Stress-strain Behavior

Figure 4.5 shows representative curves for a variety of effective processing strains. The trends resulting from increased EPS can be slit into two regimes, referred to here as the "'Low EPS"' and "'High EPS"' regimes. In the Low EPS regime, two trends are evident. As EPS increases, the Proportional Limit (PL) stress increases while the strain-to-ultimate failure decreases. The reason for this response is as follows. The matrix is in a state of compression that is beneficial to the monotonic tensile performance of the composite. Before the matrix can begin cracking, this residual compression must be overcome by the applied tension; increasing EPS causes this beneficial compression to intensify, delaying the onset of matrix cracking even further. This occurs at the expense of the fibers. Since the fibers must be in residual tension to oppose the compression of the matrix, the fibers in a state closer to their failure stress (and strain) at the beginning of applied loading. Sine some of the fibers' available strain has already been consumed (i.e. the fibers are in a state of extensional strain prior to loading), less additional strain is required for fiber rupture to occur, reducing the strain to failure as measured from the beginning of loading. Once the matrix has failed, only the fibers remain as load carrying components of the composite. Since their ultimate strength is not affected by the residual stress state in this analysis, the load required for fiber rupture to occur is also unchanged.

Once the EPS reaches a critical value, however, the material enters the "'High EPS regime"'. At this point, there is a transition from progressive failure behavior to linear brittle failure. This transition occurs because the EPS causes sufficiently high tensile stress in the fiber that fiber failure actually occurs before matrix failure. As EPS increases further, the state of stress in the fiber at the beginning of loading becomes more extreme, and failure stress and strain of the composite both continue to decrease. Figures 4.6 and 4.7 respectively show the effects of EPS on the proportional limit stress and strain-to-failure. In these figures, EPS has been normalized by the critical transition value, and the PL stress and strain-to-failure have been normalized by their values at the transition

level of EPS. Also note that in Figure 4.6 the ultimate stress is used as the proportional limit stress in the case of linear brittle failure behavior, where apparent strain-hardening does not exist.

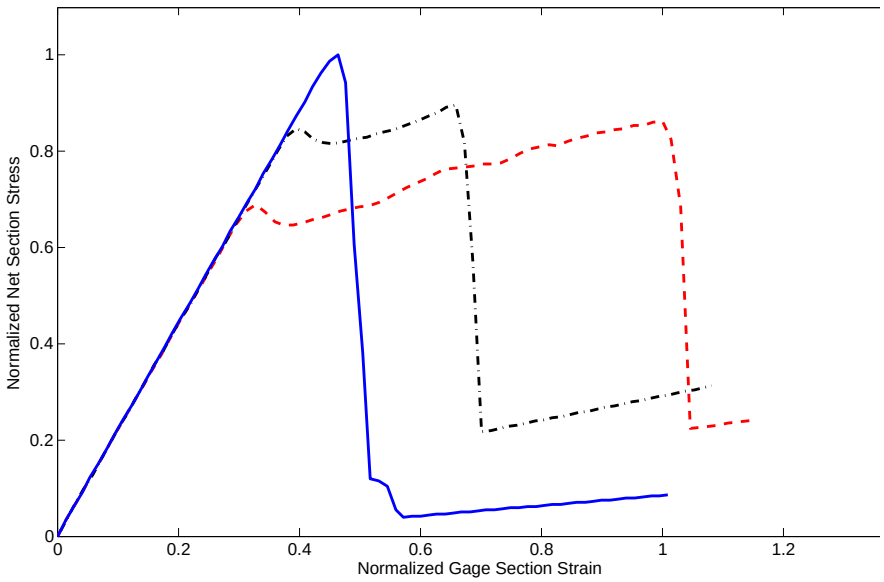

Figure 4.5: Representative stress strain curves with different magnitudes of processing-induced strain mismatch. Stresses are normalized by the maximum ultimate stress. Strains have been normalized by the maximum strain-to-failure.

4.2.4 Failure and Damage Progression

Changing the value of EPS also has an effect on the appearance of failure in the tensile coupon. Figure 4.2.4 shows still images of the damage progression when the residual stress is minimal, starting at the onset of matrix cracking and ending at first fiber failure. The damage initializes at

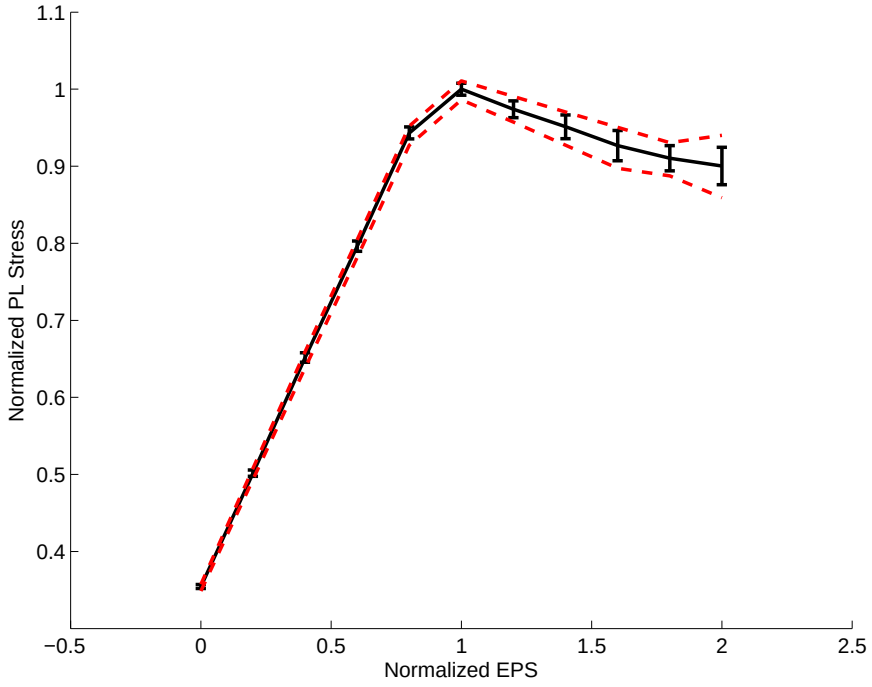

Figure 4.6: Effect of EPS on proportional limit stress. Note that for apparently brittle behavior, the ultimate tensile stress in used in lieu of proportional limit stress.

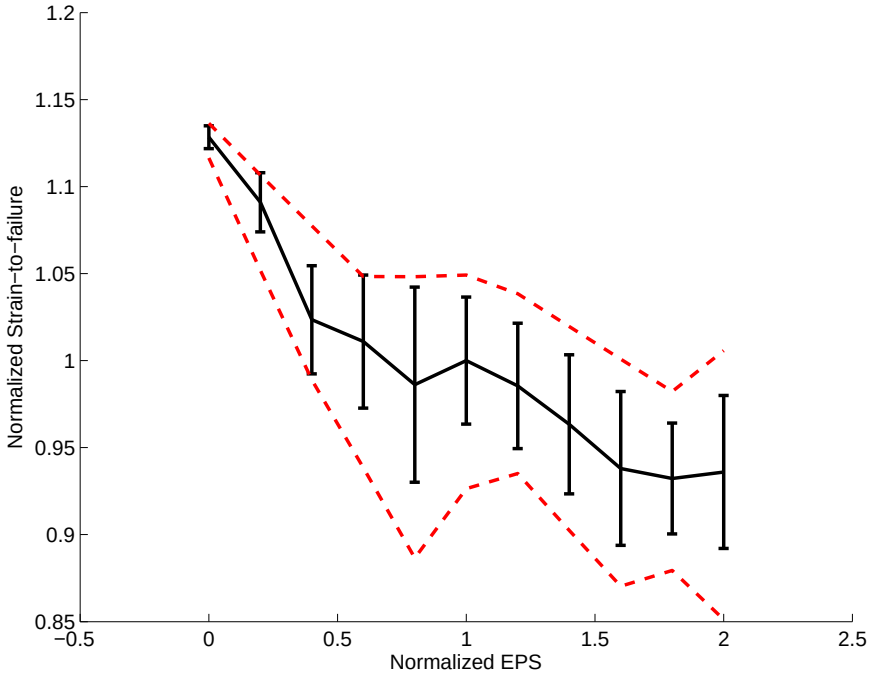

Figure 4.7: Effect of EPS on strain-to-failure

several sites withing the gage section, due to the presence of RUCs with lower effective strength As loading progresses, the initial damage propagates, but arrests upon reaching sites with RUCs possessing a higher effective strength. These cross-section can still carry high loads, and thus damage is allowed to initiate at new sites. This pattern of initiation, progression, and arrest continues until the fiber failure finally occurs.

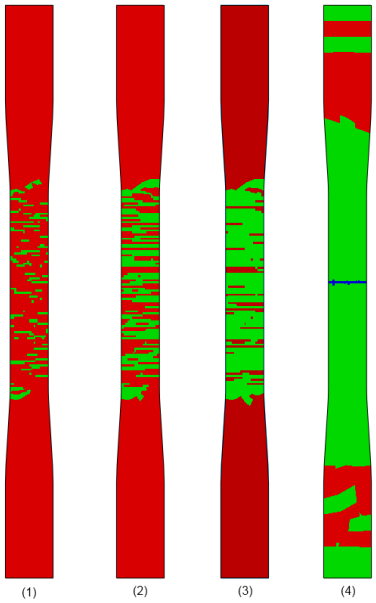

Figure 4.8: Damage progression for the case of minimal residual stress. Note the high density of matrix cracks prior to fiber fracture.

Figure 4.2.4 shows stills of damage progression in the case of a higher initial strain mismatch (i.e. higher residual stress). In this case, failure again initiates at random sites and proceeds through a pattern of progression and arrest. However, the residual tensile stress in the fiber is much higher, and so fiber failure occurs before matrix cracking can fully saturate the gage section.

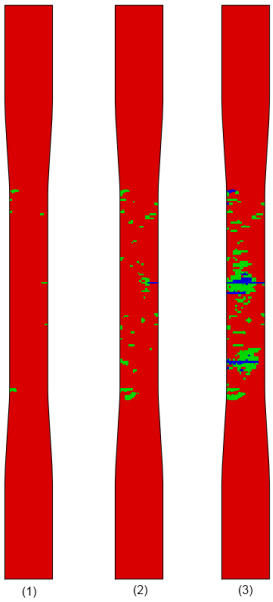

Figure 4.9: Damage progression for the case of high residual stress

4.3 Room Temperature Flexure Simulations

To validate the modeling methodology in the previous section, the room temperature ring-on-ring flexure tests were simulated using a multiscale framework comprising ABAQUS and MAC-GMC at the macro and micro-scales, respectively.

4.3.1 Simulation Details

4.3.1.1 Constituent model

For the simulations, the pre-fracture constituent model is linear elastic and isotropic for all three materials represented in the RUC. For post-fracture behavior, both the fiber and the coating use a directional subcell deletion. In these materials, the stress and strain states in each subcell are resolved into the principal frame of reference. The failure criteria are then expressed in the principal frame. When a failure criterion has been reached in a subcell, the tensile and shear moduli associated with the direction of the principal stress are set to zero; all unassociated moduli are left at their original value. The stiffness matrix in the principal frame is then transformed into the subcell reference coordinate frame.

For the matrix, the post-fracture behavior is modeled using the smeared crack model [57]. In a manner similar to that of the fiber and coating, the stress and strain states are expressed in the principal frame. The modulus associated with the direction of fracture is then reduced according to the smeared crack model. Once the smeared crack model has been invoked, the matrix transitions

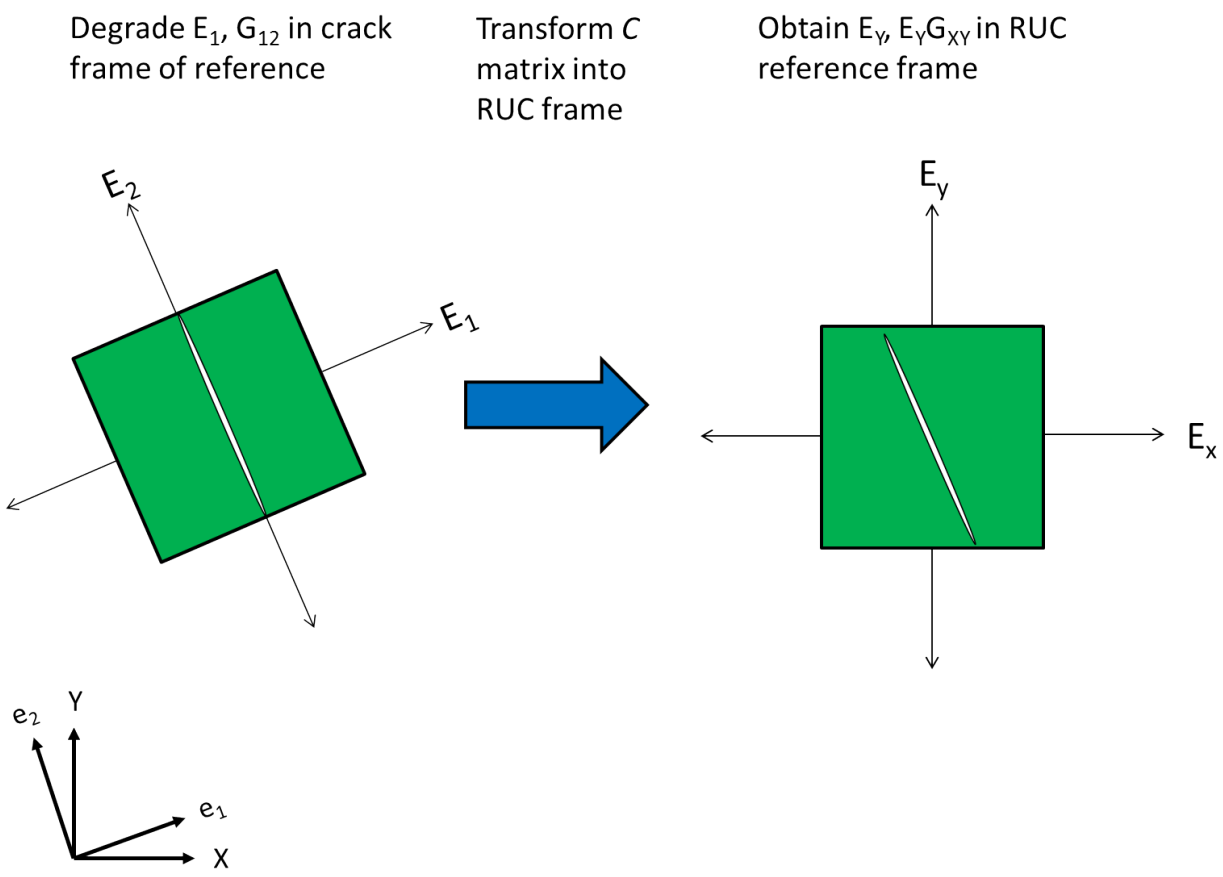

Figure 4.10: Transformation of stresses for post-fracture modeling

from behaving according to a stress-strain relation, and instead obeys a relationship between tractions and displacement (i.e. a traction-separation law). When this occurs, the displacement due to the opening of the crack in the material is "'smeared"' across the entire length of the element (or subcell), and then mathematically treated as a strain. In the current work, the traction-separation law governing the behavior of the matrix is assumed to be linear. A schematic representation of the matrix behavior in shown in Figure 4.11.

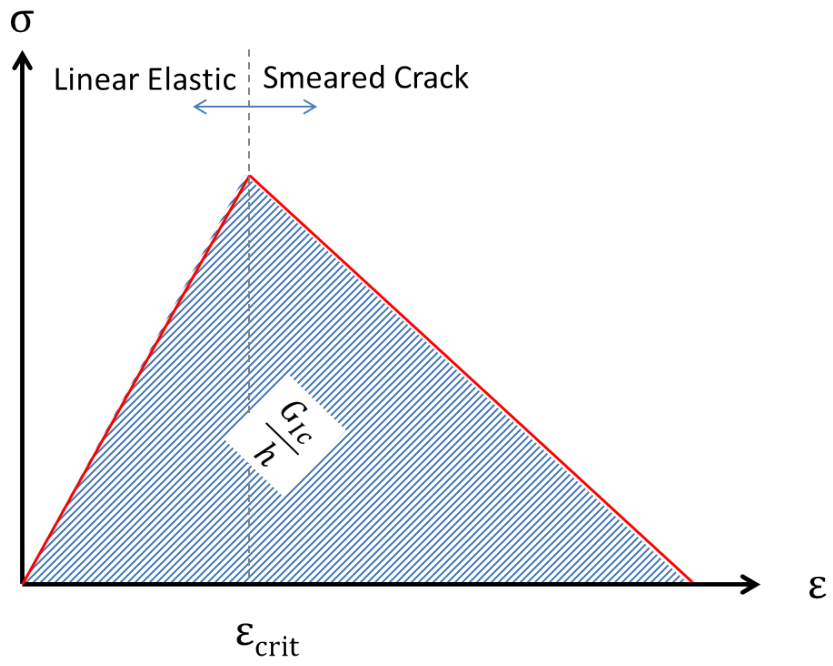

Figure 4.11: Schematic representation of the pre- and post-failure behavior for the matrix, using the smeared crack model (not to scale)

The values used for each of the constituent's properties are given in Tables 4.2 and 4.3 for old- and new-process batch material, receptively.

Phase	Fiber	Matrix	Interphase
Young's Modulus (GPa)	380	340	10
Poisson's Ratio	0.14	0.16	0.19
Failure Criterion	Max Princ. Stress	Max Princ. Strain	Max Shear Stress
Critical Strain Value ($\mu\epsilon$)	n/a	705	n/a
Critical Stress Value (MPA)	2600	n/a	6.6
Post-fracture slope (MPa)	n/a	-7.84 x 10^5	n/a

Table 4.2: Constituent material properties used in room temperature ring-on-ring simulations, for "'old process batch"' material.

Phase	Fiber	Matrix	Interphase
Young's Modulus (GPa)	400	380	10
Poisson's Ratio	0.14	0.16	0.19
Failure Criterion	Max Princ. Stress	Max Princ. Strain	Max Shear Stress
Critical Strain Value ($\mu\epsilon$)	n/a	705	n/a
Critical Stress Value (MPA)	2600	n/a	6.6
Post-fracture slope (MPa)	n/a	-7.84 x 10^5	n/a

Table 4.3: Constituent material properties used in room temperature ring-on-ring simulations, for "'new process batch"' material.

4.3.1.2 Mesh Objectivity: Smeared Crack and Energy Scaling

The smeared crack model is used in this instance to ensure mesh objectivity [48] during brittle fracture. Using normal element deletion results in a pathologically mesh dependent behavior where the results fails to converge even as mesh density approaches infinity [58]. Use of this model ensures mesh objectivity within the micromechanical model [48]. This is due to preserving energy-of fracture, such that the energy dissipated by fracture is scaled according to the element size. However, mesh objectivity at the micro-scale does not necessarily ensure mesh objectivity once the RUC behavior is propagated up to the structural (finite element) level [59]. To ensure objectivity, the physical size of the RUC within an element is scaled according to the size of that element. This ensures that the energy dissipated at the subcell scale appropriately represents the energy dissipated at the finite element scale. In other words, one would expect the fracture of a large element to require more energy than the fracture of a small element. This energy scaling scheme preserves mesh objectivity across length scales [48].

4.3.1.3 Incorporation of residual stress

There are several possible methods to handle the inclusion of residual stresses within a numerical model. While a full process simulation would allow for the most accurate residual stress to be generated, this would require detailed knowledge of the manufacturing process and the behavior of the materials and precursors across the entire environmental range of the processing history, including phase changes and creep. Instead, a simplified method is used in which the net effects of all processing induced strain are quantified by a single value, here called the EPS. This equivalent strain is intended to model all accumulated strain mismatch between the fiber and the matrix, but primarily considers the strain due to crystallization of free-silicon within the matrix and any relative creep that occurs between the fibers and matrix during time spent at elevated temperature. While in principle the EPS could be determined from a detailed process model, in this work it is instead estimated based on the uniaxial results seen in Section 4.2. Practically, the EPS is implemented in the same fashion as in Section 4.2, where it is incorporated as a large, negative thermal expansion

strain for temperatures between 1410°C and 1409°C. outside of this range, the normal value of thermal expansion strain is used.

4.3.2 Mesh Convergence Study

A mesh convergence study of the room temperature biaxial flexure simulations was performed to ensure that the results presented were numerically accurate. For this study, three meshes were considered. These meshes are shown in Figure 4.12. Details of the meshes (element sizes and numbers) are summarized in Table 4.4.

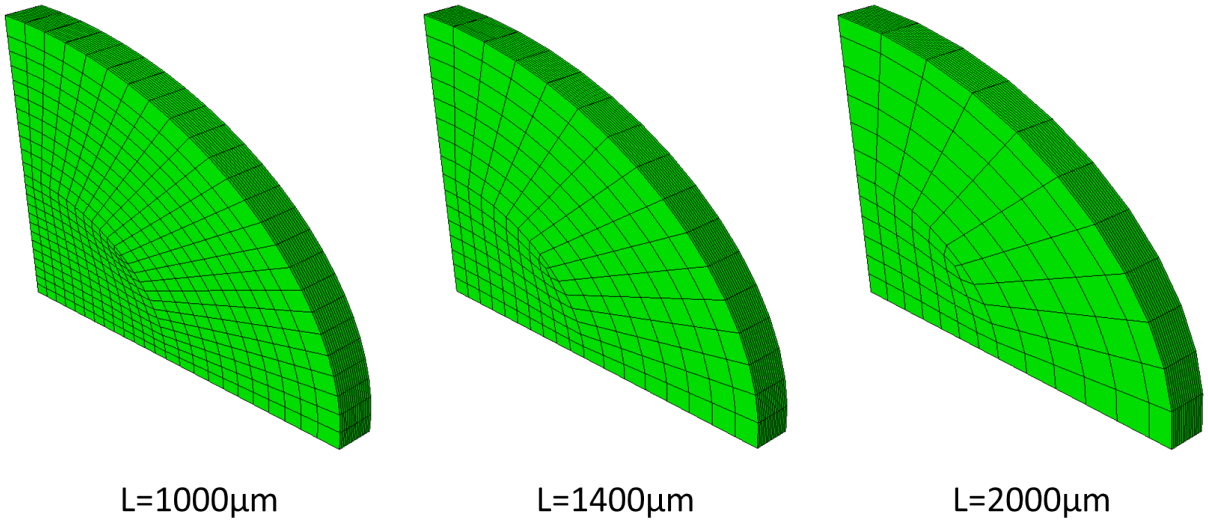

Figure 4.12: Meshes used for Mesh Convergence Study

Average Characteristic Element Length ($\mu\epsilon$)	Number of Elements
2000	1712
1400	3312
1000	10064

Table 4.4: Mesh parameters and computational time for each mesh used in the convergence study.

Figure 4.13 contains the load-displacement curves obtained from the mesh converge simulations. Figure 4.14 shows the damage patterns predicted by these simulations. The load-displacement curves show good agreement for meshes with a characteristic length below 1400 μm. The damage plots also show good agreement for the same set of finer meshes. The locations of failure onset and the paths of additional damage are also closely aligned at the finer meshes. Taken together, this indicates that a mesh with a characteristic element length of 1400 microns is

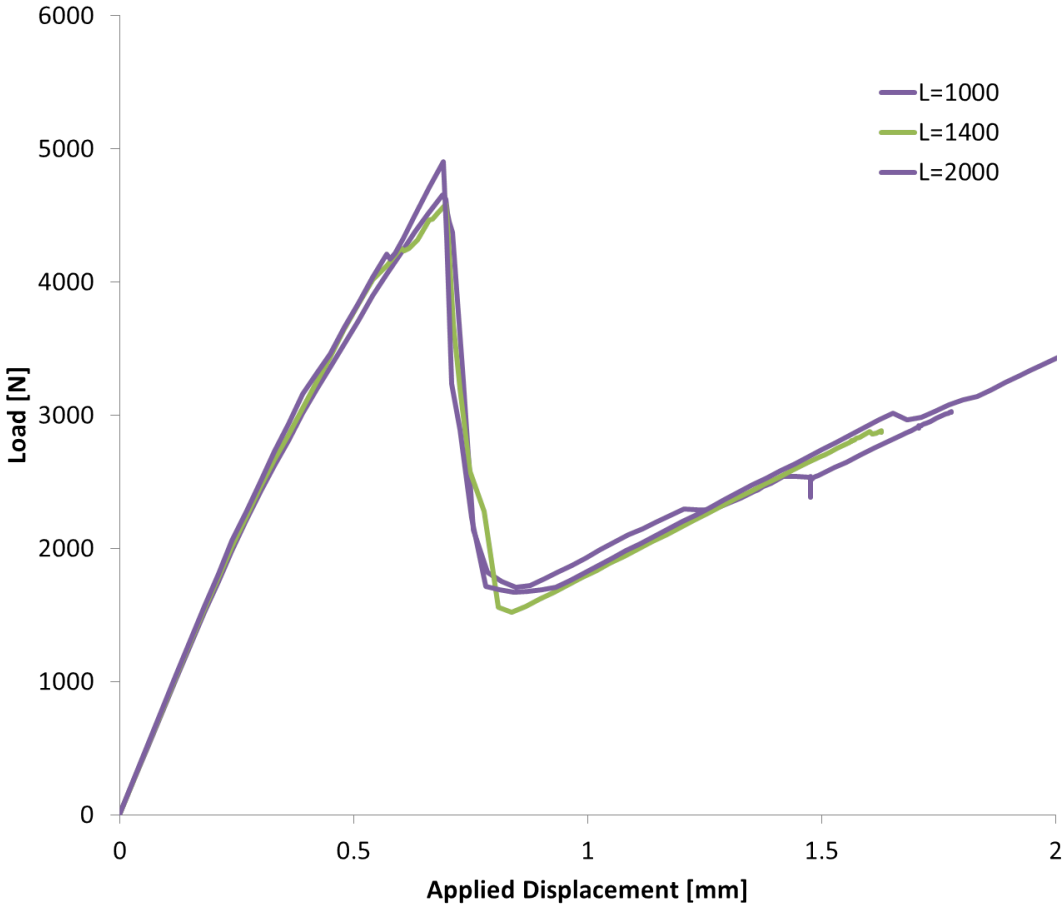

Figure 4.13: Load-displacement curves resulting from each mesh in the room temperature convergence study, indicating a mesh converged for characteristic element length below 1400 microns.

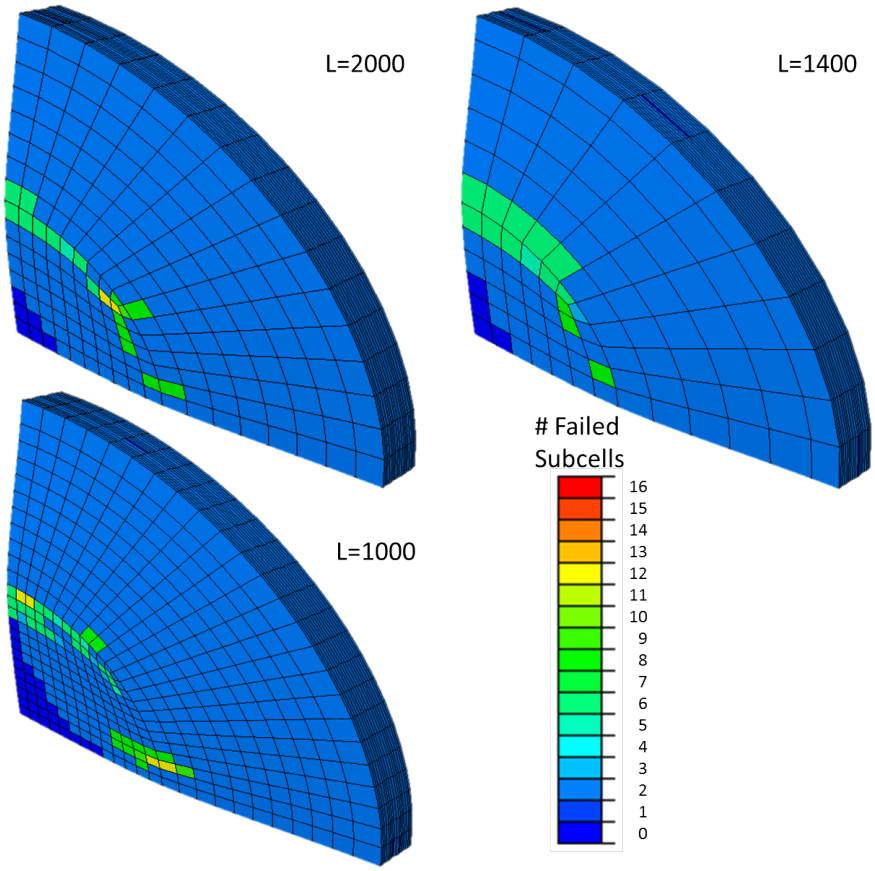

Figure 4.14: Color maps indicating the extent of damage predicted by the simulation. The left column is taken at the proportional limit. The right column is taken at the local minimum load following the major load drop. The color corresponds to the number of failed subcells in the RUC contained within each element. The similarity in damage patterns indicate that the meshes predict the same type of failure behavior.

sufficiently converged for the purposes of this work. This mesh is used for all further simulations of the ring-on-ring test.

4.4 Residual Stress Effects in Room Temperature Ring-on-Ring Simulations

4.4.1 Determination of Residual Stress Magnitude

In order to determine the degree of residual stress present, several simulations were carried out. Two states of residual stress were considered as part of this study, which are outlined experimentally in Chapter 5, Section 5.5. The heat-treated condition was treated as a baseline, in which the only residual stress introduced only in the cool-down phase of the heat treatment cycle, and is solely due to the thermal mismatch of the constituent materials[3]. The goal of this study, then, is to determine the appropriate level of EPS in the as-received specimens from the new process batch of material.

The parameters for these simulations remain the same as those outlined in the previous sections, including the mesh, RUC, and constituent properties. The load-displacement plots for the as-received and annealed simulations are shown in Figure 4.15.

For these curves, the simulation was unable to continue beyond the point at which the fibers began to fail due to non-convergence at the finite element level. Colormaps showing the number of failed subcells in each element are shown for select string points in Figures 4.16 and 4.17 for the as-received and annealed cases, respectively.

From the load displacement curves, it is evident that the proportional limit is increased by the higher residual stress in the as-received case. The PL load in this case has been increased by approximately 9% over the annealed simulation. However, the ultimate load is not strongly affected by residual stress, at least within the regime studied here. Comparisons between the simulations and experiments will be covered in Chapter 6, Section 6.1.

[3]It is still possible that residual stress from processing remains after the heat treatment. This is neglected in this case, and any residual stress remaining at this point would be included in the apparent strength of the matrix. The EPS added in the second phase of this study thus results in an additional residual stress on top of what cannot be annealed out using the procedure outlines in Chapter 5, Section 5.5.

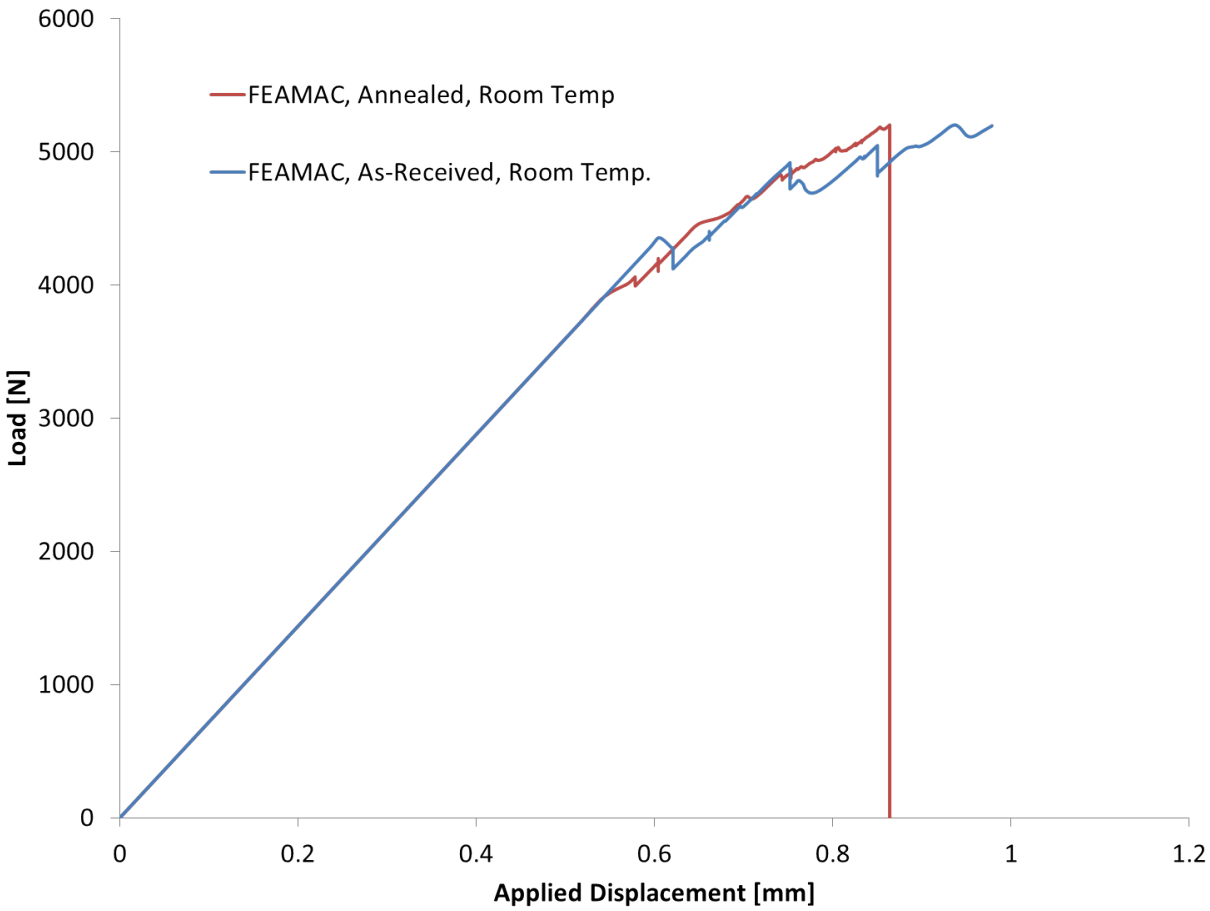

Figure 4.15: Load-displacement curves for as-received and annealed material simulations

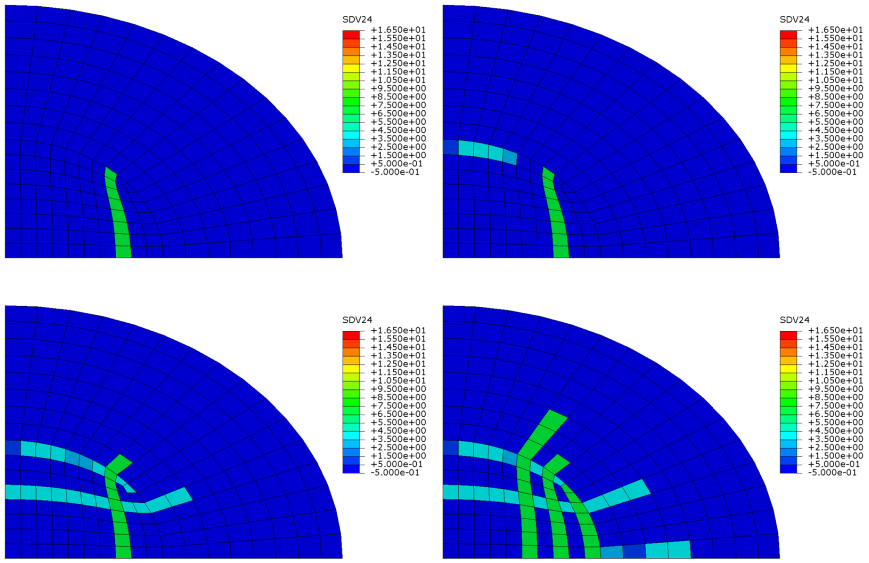

Figure 4.16: Damage colormap for the as-received room-temperature simulation. Colors indicate the number of failed subcells in the RUC in each element.

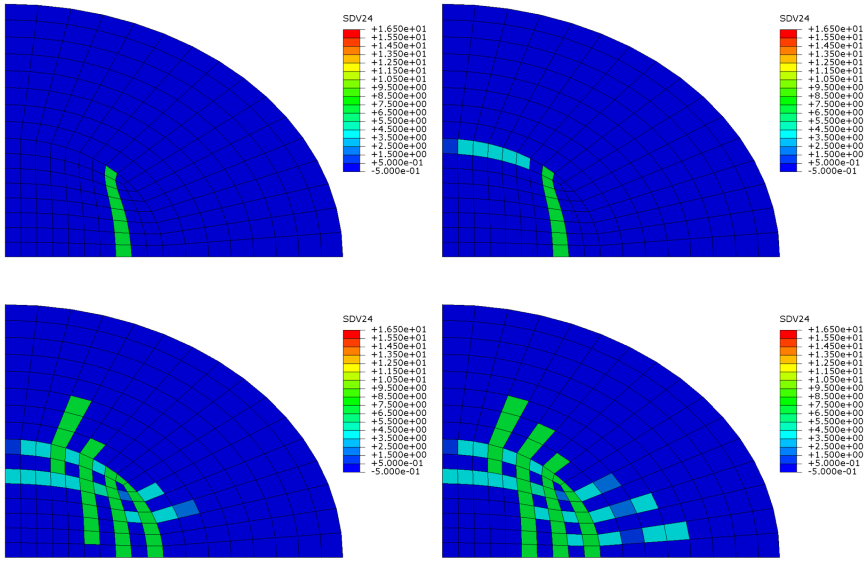

Figure 4.17: Damage colormap for the annealed room-temperature simulation. Colors indicate the number of failed subcells in the RUC in each element.

4.5 High Temperature Flexure Simulations

4.5.1 Simulation Details

For the high temperature simulation, the same procedure, RUC, and finite element mesh were used as in Section 4.3 with minor changes: The step schedule is now

0) Initial Temperature 1410°C

1) Cool to 1409.99°C

2) Cool to 1409.01°C

3) Cool to 1409.00°C

4) Cool to 23°C

5) Heat to 1315°C

6) Apply load

The use of cooling beyond testing temperature before reheating was chosen due to both being closer to the physical history of the specimen as well as ensuring that any damage that may occur during cooling/heat contraction/expansion would be permitted to evolve naturally. It is noted that this may not be necessary in all cases if previous work had shown that no additional damage was expected during this late cool and heating cycle. Omitting this step may save a considerable fraction of the total CPU time. However, this investigation had not been performed a priori, and so the reheating step remained in the simulation shown here.

The constituent values provided in in Table 4.5 used for the high temperature simulations, based on matching the salient features of the load-displacement curves to those of the experiments.

Parameter	Initial Value At Room Temp.	Value at 1315°C
Fiber Tensile Modulus (GPa)	400	380
Matrix Tensile Modulus (GPa)	380	360
Matrix Strain-to-Failure	0.000705	0.000623
Matrix Post-Failure Slope	-7.84 x 10^5	-6.51 x 10^5
Fiber Strength (MPa)	2600	1800

Table 4.5: Constituent properties for high temperature simulations

Using these values, the load-displacement curve in Figure 4.18 was obtained. Figure 4.19 shows the damage colormaps obtained from this simulation.

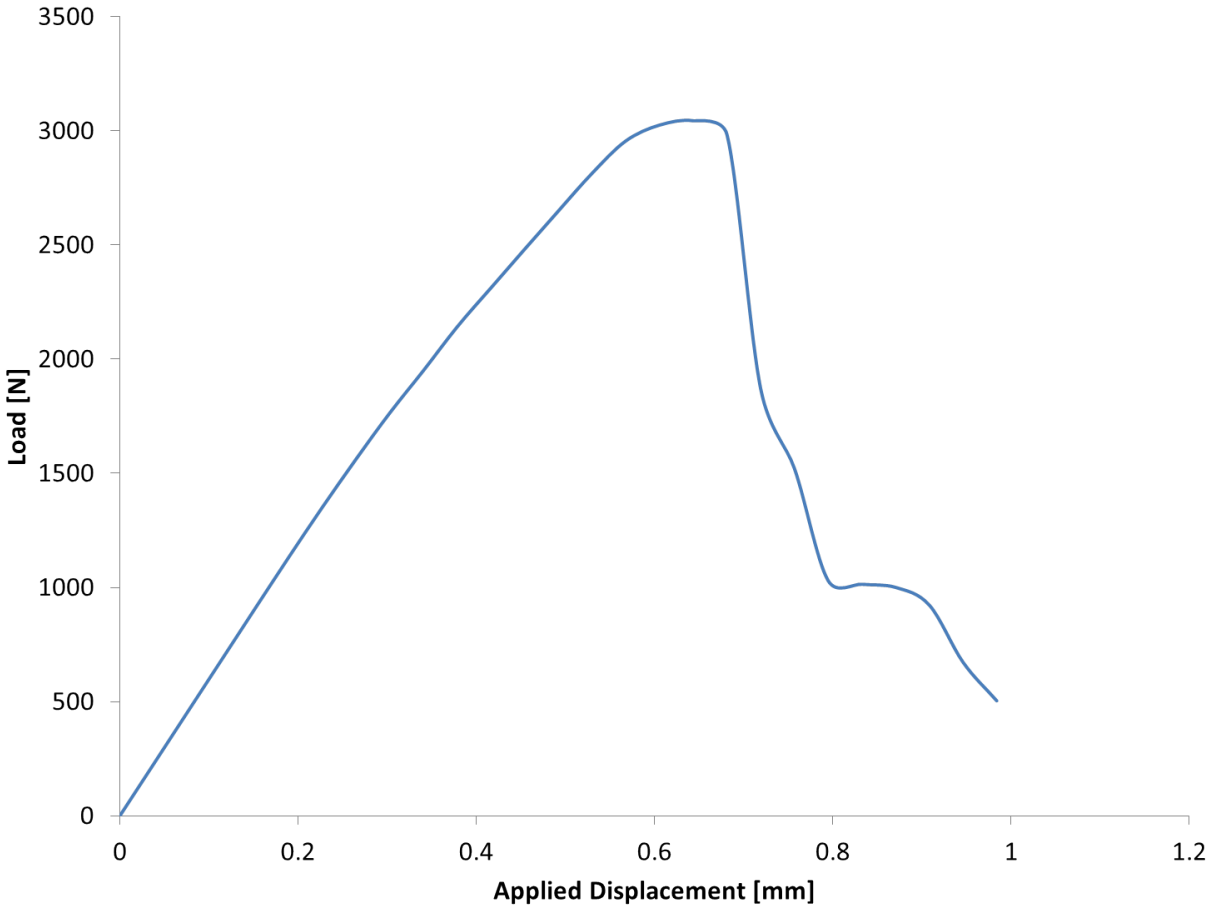

Figure 4.18: Load-displacement curves resulting from high-temperature prediction.

The results of these simulation and their accuracy in representing the experiments will be discussed in greater detail in Chapter 6, Section 6.1.

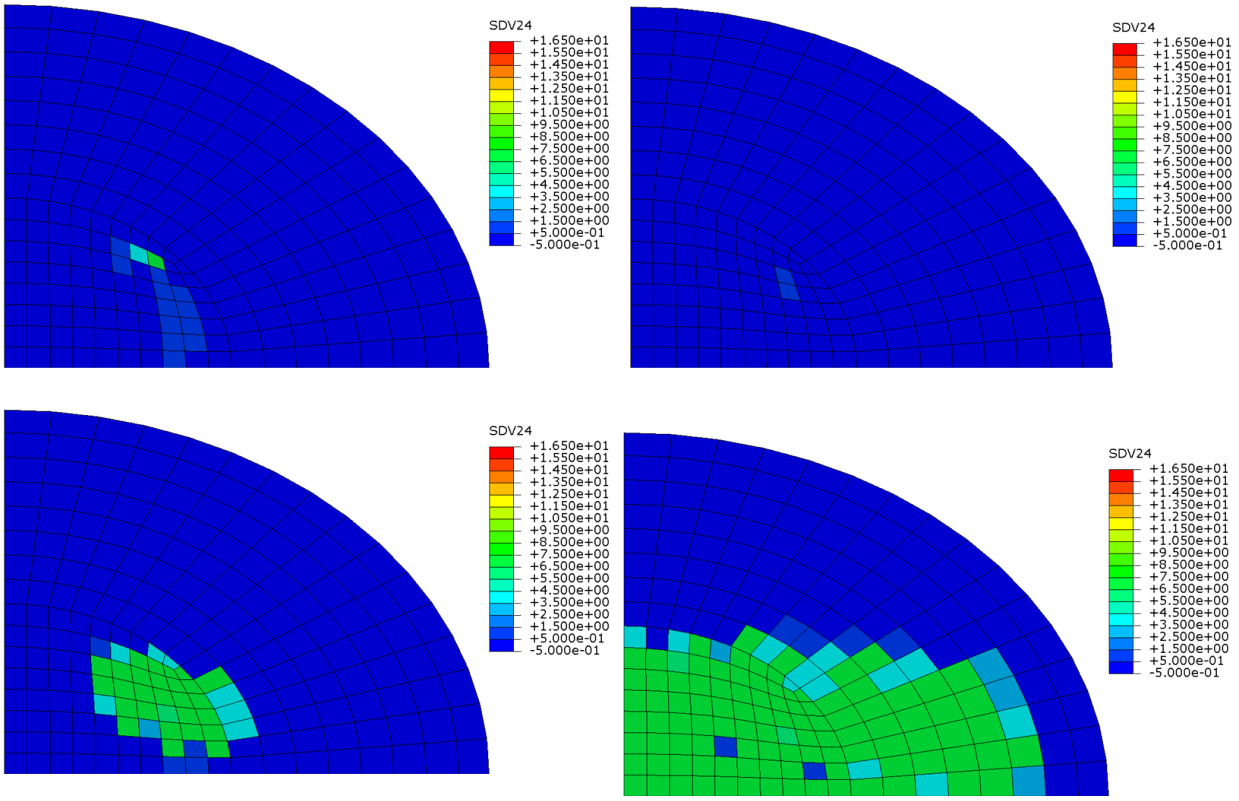

Figure 4.19: Colormap of damaged subcells. Colors represent the number of failed subcells in the RUC associated with each element.

4.6 Concluding Remarks

A multiscale framework is used to investigate the effects of residual stress due to processing-induced strain mismatch on the monotonic performance of ceramic matrix composites. It is found that increasing this strain mismatch can lead to improves monotonic performance (i.e. increased proportional limit stress and delayed matrix cracking) at the expense of reduced strain-to-failure. However, if the strain mismatch exceeds a critical value, the critical failure mode transitions from progressive matrix cracking to catastrophic fiber failure, leading to linear-brittle failure behavior. Beyond this critical point, increased effective processing strains only further degrade the performance of the composite, both in terms of ultimate tensile stress and strain-to-failure. Therefore, there exists an optimum level of strain mismatch, the specific magnitude of which would be dependent on application conditions.

CHAPTER 5

Experiments

Real CMC components in service will experience complex, multiaxial stress states. A large body of work exists for modeling and analyzing CMC behavior under uniaxial stress states, but only a much smaller body exists for multiaxial testing. Due to the difficulty of conducting biaxial tension tests, most work on this topic is based on tension-torsion (refs), or biaxial flexure. For this work, biaxial flexure was chosen as the preferred test technique due to the ease and cost of manufacturing consistent specimens. The configuration used for the current work is a ring-on-ring configuration. This was chosen due to the relatively large region of nearly uniform strain that is induced in the crown of the bend specimen, as opposed to the smaller uniform strain region induced under ball-on-ring configurations. In this regard, the ring-on-ring configuration can be viewed as a biaxial analogue to the four-point bend test. (more refs, etc etc).

For the work presented here, material was provided over several manufacturing batches. These batches were determined to belong to two different groups, separated by time of manufacture, due to a change in processing. These batches will be accordingly referred to as "'old-process"' and "'new process"' material in the following discussion.

5.1 Ring-On-Ring Testing Overview

Testing of any material under biaxial tension is a difficult process. Considerable effort must be taken in the design of specimens for cruciform tension tests to ensure failure occurs in the gage section [19, 20, 60] For this reason, biaxial flexure was chosen instead of biaxial tension to characterize the response of the CMC. Specifically, ring-on-ring flexure was chosen due to the larger region of the specimen that would be subjected to maximal biaxial load (as compared to ball on ring). The ring-on-ring test is an American Society for Testing and Materials (ASTM) standard test for monolithic ceramics, and much of the following testing is based on ideas from that standard. Figure 5.1 shows the ASTM standard reference figure for this test.

All ring-on-ring tests contained in this work take the same basic configuration. The specimens

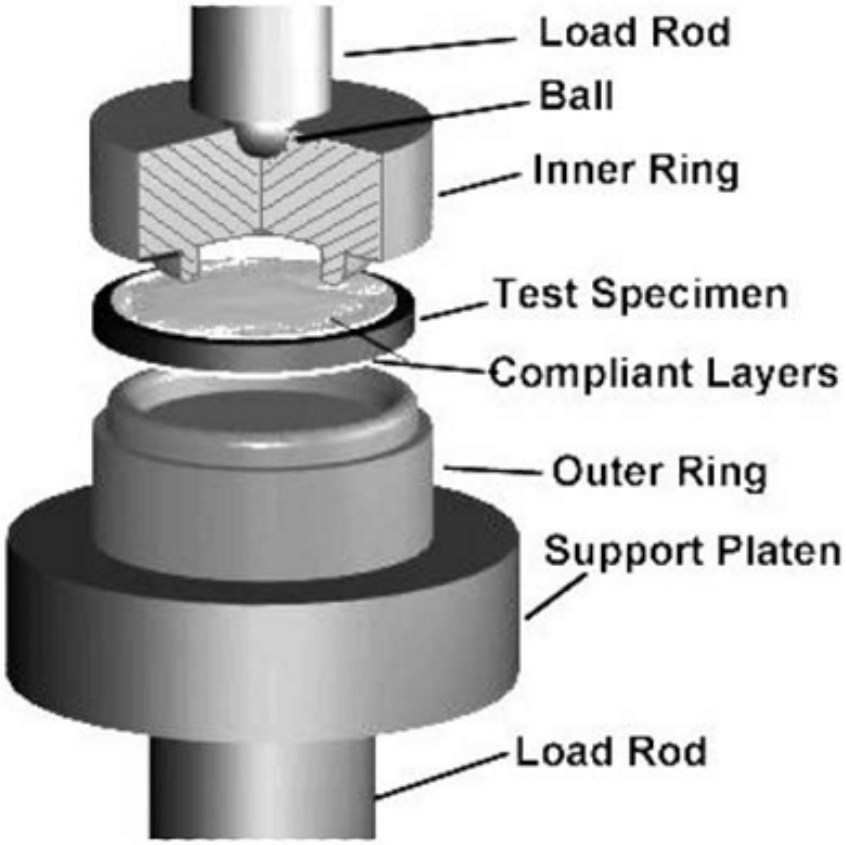

Figure 5.1: ASTM Description of the Ring-on-ring flexure test for monolithic ceramics, from [2]

are discs with a diameter of 43.2 mm (1.7 inches). The thickness of the specimens is taken as received, and is nominally 2.0 mm for old process batch material, and 1.8 mm for new process batch material. These dimensions are summarized in Figure 5.2. For the fixture, the outer supporting ring has a nominal contact diameter of 38.1 mm (1.5 inches). The inner loading ring has a contact diameter of 19.1 mm (0.75 inches). The toroidal radius of the rings is 0.6 mm. These dimensions are summarized in Figures 5.3 and 5.4.

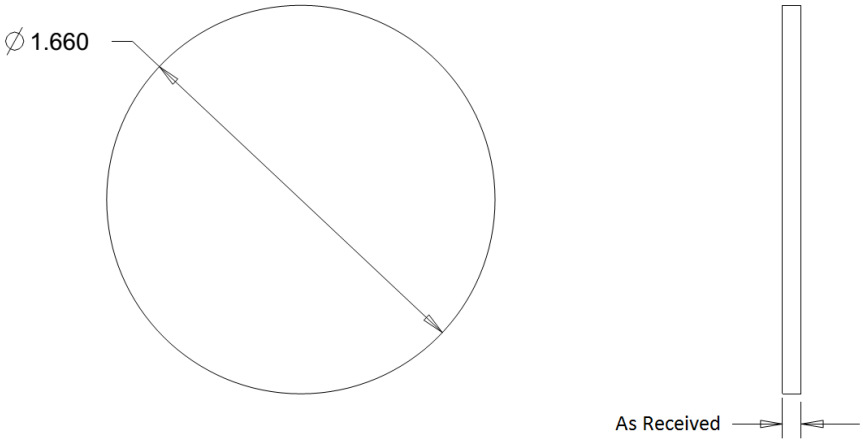

Figure 5.2: Dimensions of the ring-on-ring specimens

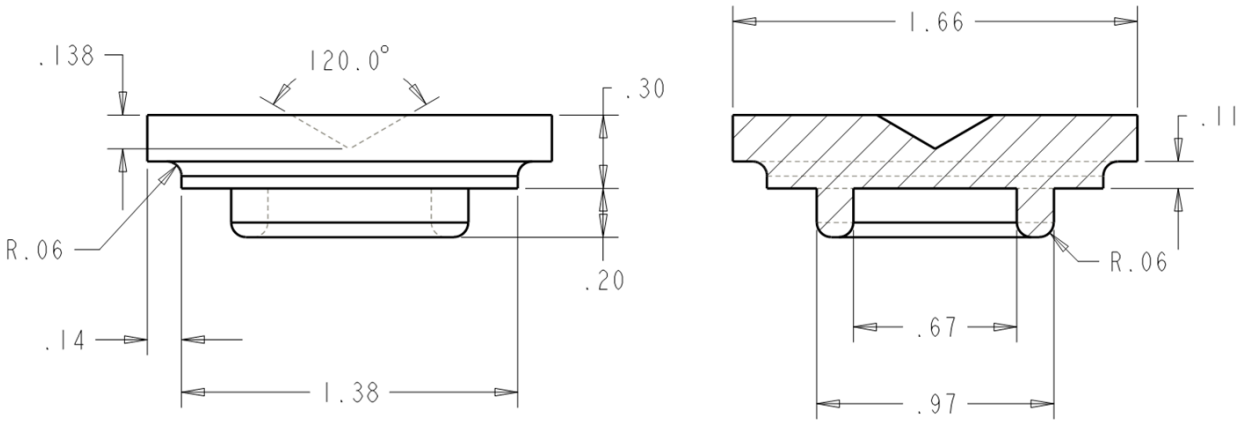

Figure 5.3: Dimensions of the loading ring used for room-temperature ring-on-ring testing

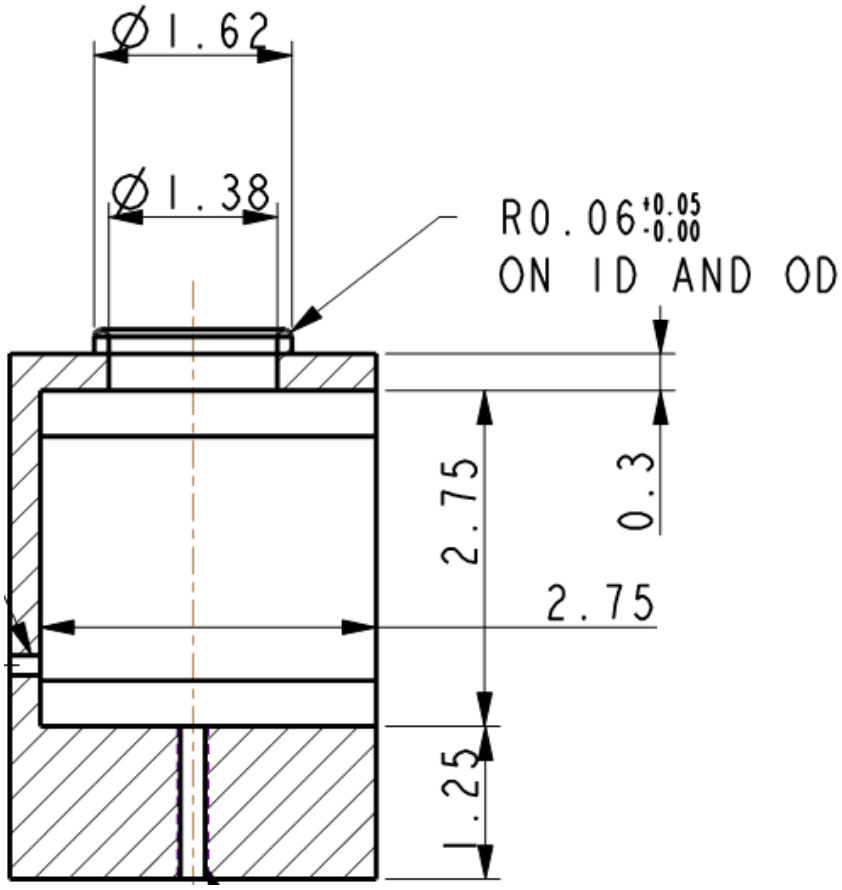

Figure 5.4: Dimensions of the support ring used for room-temperature ring-on-ring testing

5.2 Room-Temperature Testing

To characterize the room temperature response of the composite, biaxial flexure testing was conducted. The tests were performed on an INSTRON universal testing machine under displacement controlled loading at a displacement rate of 0.25 mm/s. A fixture consisting of a supporting structure containing a mirror was used to allow the tension side of the specimen to be imaged for DIC analysis. The fixture is shown in Figure 5.5. A close-in view of the loading fixture can be seen in Figure 5.6. The applied load was measured using a strain-gage-based load cell with a maximum load capacity of 22 kN (5000 lbf). In addition to load and displacement data, the tension side of the specimen had a random speckle pattern applied and surface strains were measured using Digital Image Correlation (DIC). A standard aerosol spray paint was used to applied the speckle pattern. A base layer of white paint was applied first, after which the black speckle pattern was applied. A single camera technique was chosen due to ease of set up[1]. The magnitude of the surface strain is not used in this analysis. Rather, the technique is used to identify the potential onset of damage by identifying localized regions of increased strain in the specimen. This both shows the location of the damage and ensures that the desired failure mode is occurring. In all cases, a subset size of 30 pixels with a step size of 10 pixels was used for the DUC analysis.

The load-displacement curves from the room temperature tests with "'old process"' material are shown in Figure 5.7. The key parameters from this round of testing are summarized in Table 5.1.

Specimen ID	Linear Stiffness [N/mm]	Proportional Limit Load [N]	Ultimate Load [N]
2007-01-0006-1.7-F-1	7918	2675	N/A
2007-01-0006-1.7-F-2	7487	2414	5717
2007-01-0006-1.7-F-3	8123	2652	5771
2007-01-0006-1.7-F-4	8225	2603	N/A
Average Value	7938	2586	5744

Table 5.1: Summary of Key Parameters from tests at room temperature: old-process batch material. Specimens with no ultimate load were stopped early to allow for investigation of damage.

Similarly, the load-displacement curves from the room temperature tests with "'new process"' material are shown in Figure 5.8. The key parameters from this round of testing are summarized in Table 5.2.

The combined old- and new-process batch curves are shown in Figure 5.9. From this chart, some key differences are evident. The new-process specimens have much lower bending stiffness

[1]It is noted that a two-camera stereo-vision setup would provide more accurate strain information on the specimen surface. However, due to the inaccuracy inherent in the method, and the relatively low surface strains experienced by the composite, DIC should not be assumed to provide accurate strain values, even in a stereovision setup. The purpose of DIC in this case is to identify "'strain hotspots"' that would be associated with any form of damage occurring during the test.

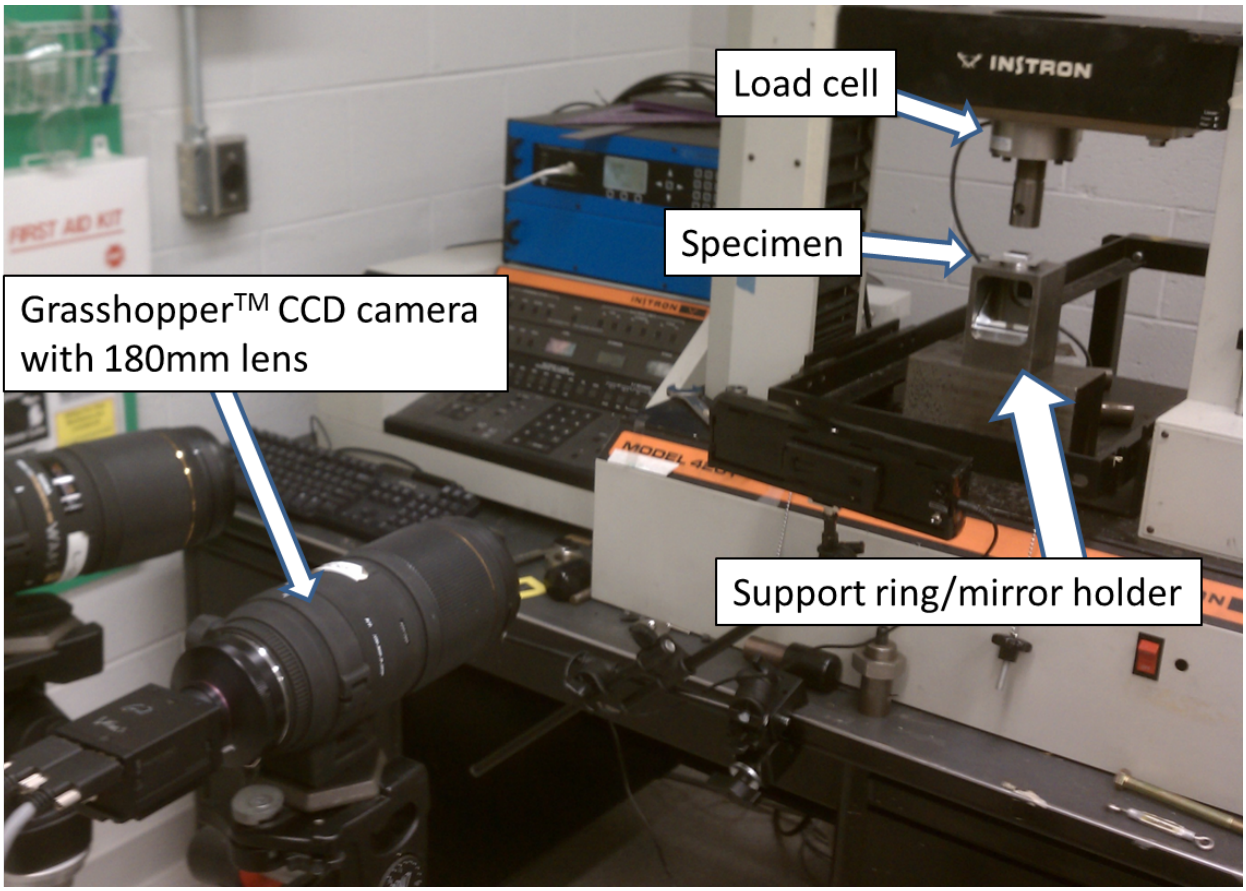

Figure 5.5: Testing setup used for room temperature ring-on-ring biaxial flexure.

Specimen ID	Linear Stiffness [N/mm]	Proportional Limit Load [N]	Ultimate Load [N]
2098-01-0007-F-1	6280	2073	4941
2098-01-0007-F-2	6183	1757	5082
2098-01-0007-F-3	6146	1775	4679
2098-01-0015-F-1	6299	1862	5134
2098-01-0182-2	6690	2420	5717
2098-01-0182-3	6673	2053	5022
2098-01-0183-1	6275	1771	n/a
2098-01-0183-2	6459	1830	5775
2098-01-0183-3	6545	1728	5427
Average Value	6394	1919	5223

Table 5.2: Summary of Key Parameters from tests at room temperature: new-process batch material. Specimens with no ultimate load listed were stopped prior to final failure to allow for damage investigation.

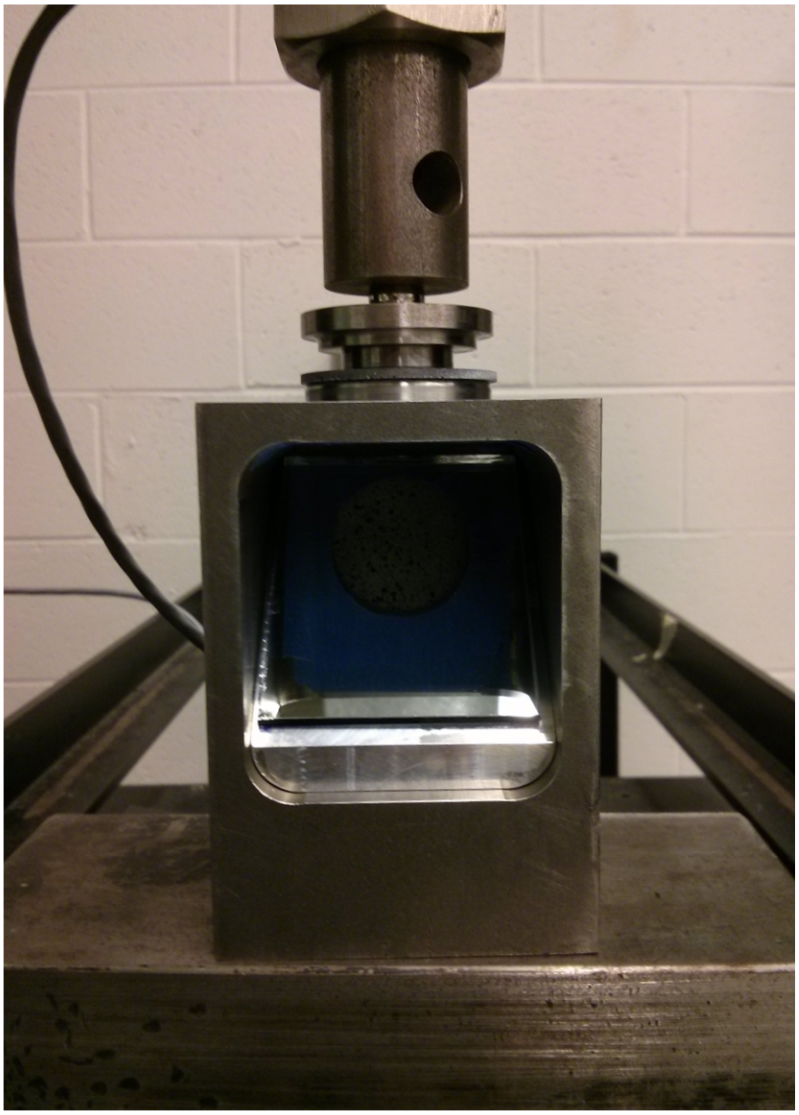

Figure 5.6: Close-in view of the loading fixture used for room temperature ring-on-ring biaxial flexure with DIC.

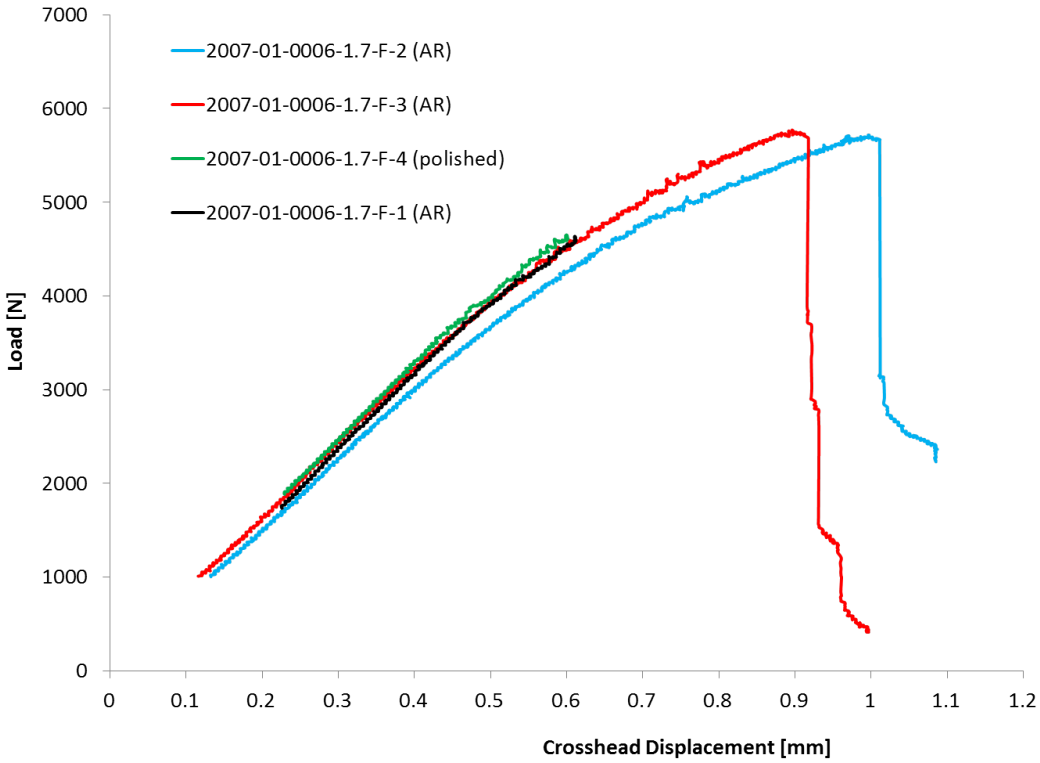

Figure 5.7: Load-Displacement curves from ring-on-ring testing conducted at room temperature: old-process batch material. Note that Specimens 2007-01-0006-1.7-F-1 and 2007-01-0006-1.7-F-4 were interrupted to allow for the damage investigation presented in Section 5.2.1.

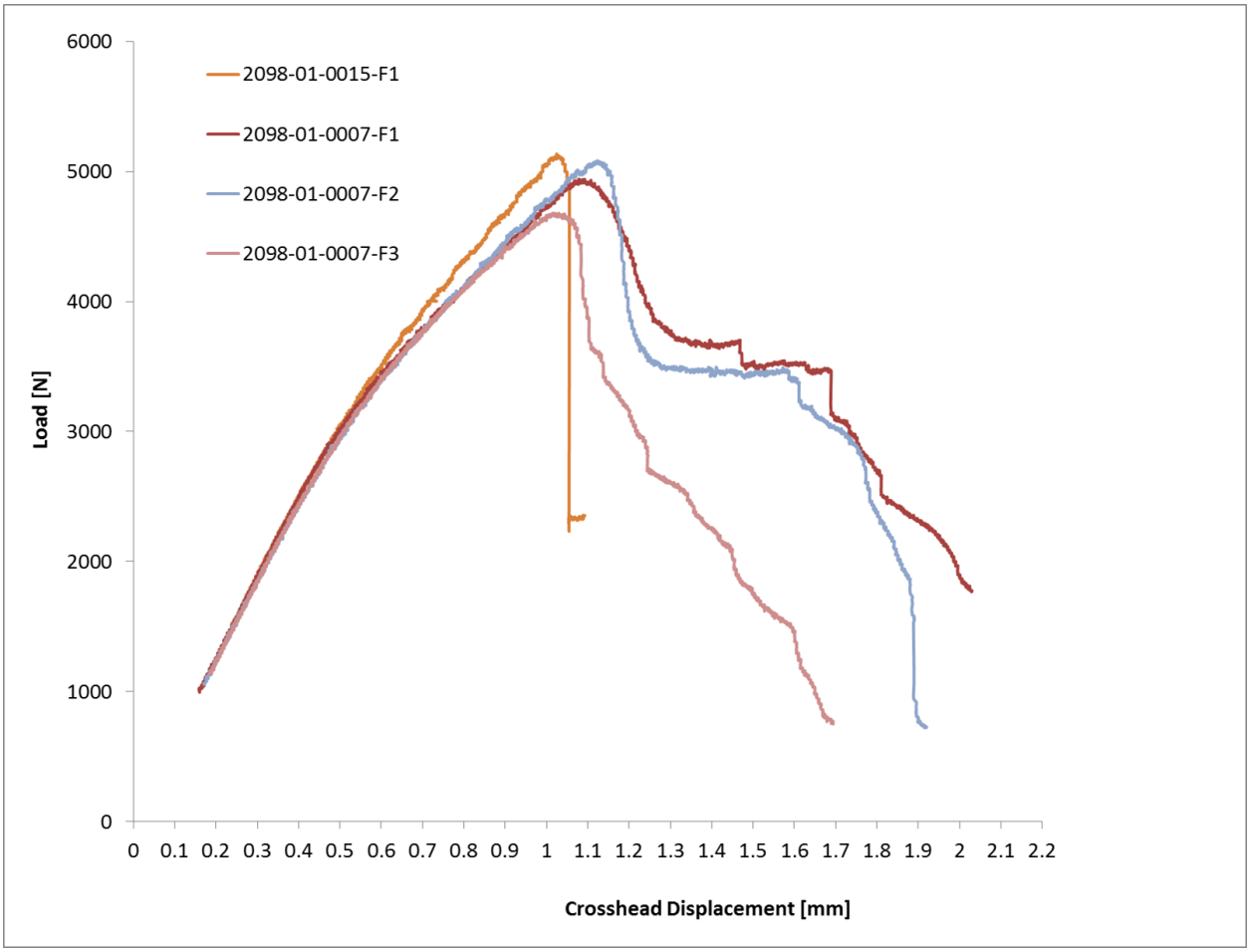

Figure 5.8: Load-Displacement curves from ring-on-ring testing conducted at room temperature: new-process batch material

than the old-process material. The major contributor to this difference is a variation in specimen thickness: the old process yielded specimens with an average thickness of 2.03mm. The new process yields specimens with an average thickness of 1.78mm. This thickness reduction alone would result in a decrease in bending stiffness of 32%. However, the new-process bending stiffness is only reduced by 21%. This implies that an increase in constituent stiffness as a results of the new process material, which must be taken into account during the simulations presented in Chapter 4.

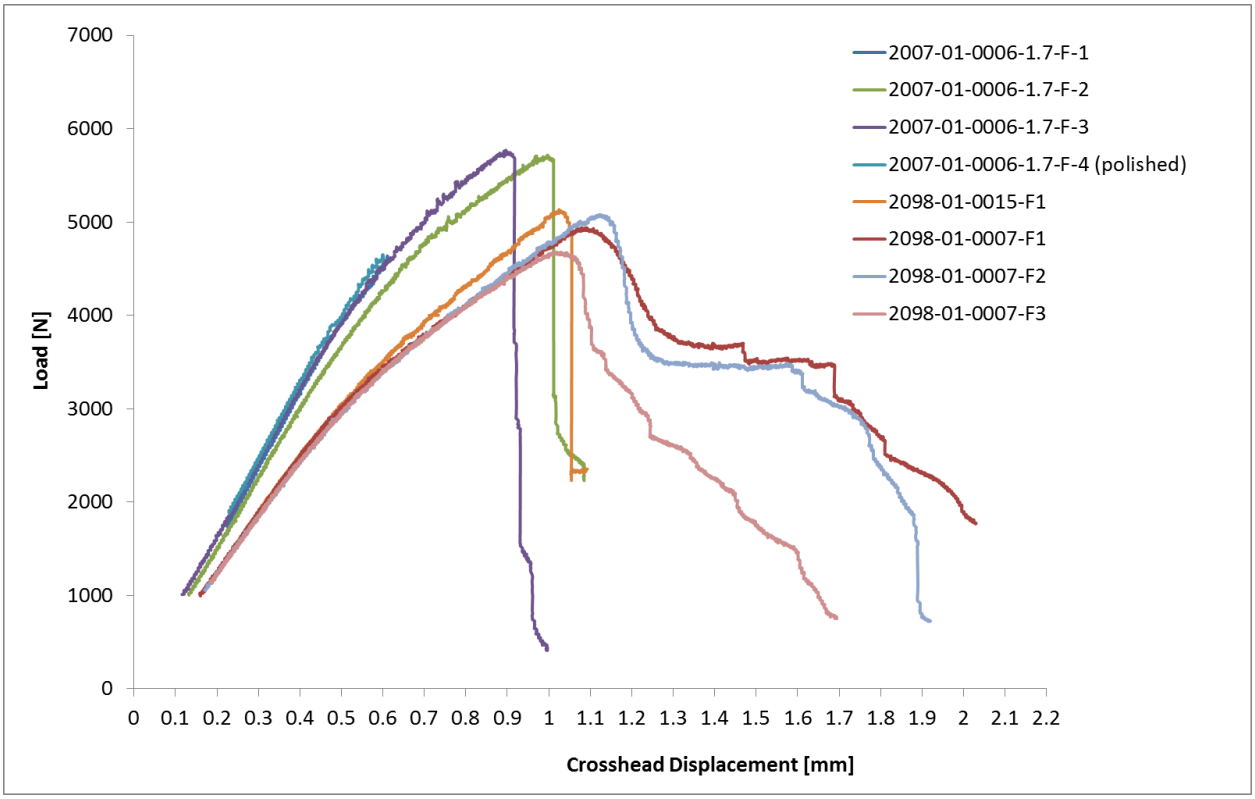

Figure 5.9: Load-Displacement curves from all room temperature: new-process batch material, as-received condition

5.2.1 Room-temperature damage investigation

The final failure of composite specimens loaded well beyond the peak load was seen to take two forms. In one form, the final failure took appearance of a central punch-out on the tension side ply, as as shown in Figure 5.10. The central punch-out appeared to be under the loading ring. On the compression side of the specimen, the circumference of the crack occurs under the loading ring, slightly to the inside. The compression side cracks can be seen in Figure 5.11. An interesting note about the final failure is that the radial cracks in the outer portion of the specimen do not occur parallel or orthogonal to the surface fibers. Instead, they tend to be offset from this frame of reference by 15-20°.

Figure 5.10: Tension side of a room temperature specimen, exhibiting a central punch-out failure mode

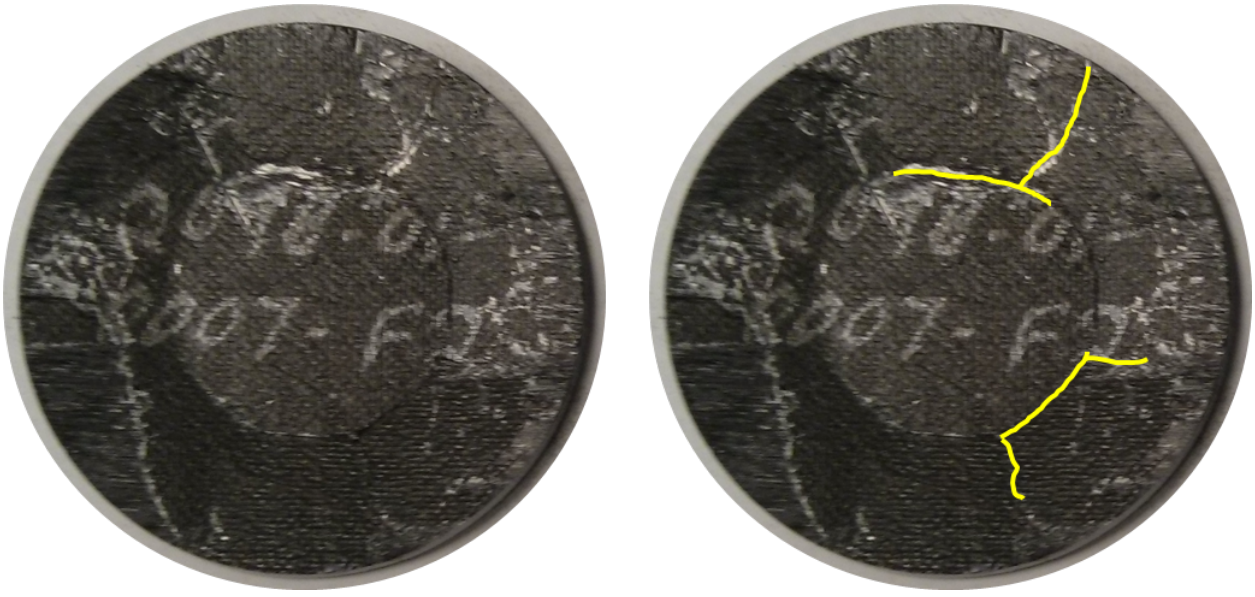

Figure 5.11: Compression side of a room temperature specimen.

Figure 5.12: Tension side of a room temperature specimen, exhibiting a flap-like punch-out failure mode

The second form of final failure was that of a "'flap-like"' punch-out, as seen in Figure 5.12. In this form of failure, instead of a roughly circular crack, there is a roughly half-circular crack, which then extends out to the outside edge of the specimen. The central region is then pushed out, similar to a flap. On the compression side of the specimen, the circumference of the crack does not occur directly under the loading ring, but instead is inside, suggesting a conical interior crack. The compression side cracks can be seen in Figure 5.13. There is no apparent difference in the load-displacement behavior between the flap-like punch-out or the central punch-out.

Prior to final failure, however, DIC analysis revealed cracking in the gage section of the specimens. To qualify this analysis, two specimens viewed under optical microscopy to visually search for cracks. These tests was interrupted at a load corresponding to 80% of the average ultimate load for this batch of specimens, which also corresponds to 75% greater than the proportional limit. Because ceramics experience little to no plastic deformation, it was necessary to cut the specimen into a "'beam-like"' configuration and hold any cracks open in a small bending fixture. This fixture places the sectioned specimen in uniaxial flexure, loaded in a screw-driven displacement-controlled fashion, to force open any cracks that may have been present after testing. Specimens were loaded to a displacement equal to one-half of the displacement at the proportional limit load during test. Limiting the displacement in this fashion reduced the likelihood of additional damage being induced during this post-test analysis. Specimens 012-02-909-2 and 012-02-909-4 were sectioned such that the surface ply was oriented along the bending axis. [4] This allowed for cracks in multiple directions to be viewed.

[4] An additional two specimens sectioned with the surface fibers perpendicular to the loading axis, but this configu-

Figure 5.13: Compression side of a room temperature specimen.

The specimens imaged in this fashion were previously painted for DIC imaging. To aid in the discovery of cracks, most, but not all, of the paint was removed. It was found that the remaining white paint from the base layer of DIC patterning increased contrast with the cracks, allowing them to be more easily identified in the images.

Several cracks can be seen in these images. This indicates that damage did occur in the gage section before the larger "'punch-out"' crack become dominant. In Figure 5.16 in particular, the spacing of cracks can be seen to be between 1.6-2.2mm. This is similar to the spacing between strain-localization regions seen in the DIC results, as shown in Figure 5.17.

ration proved too weak to open the cracks to the point of visibility without inducing further damage to the specimen.

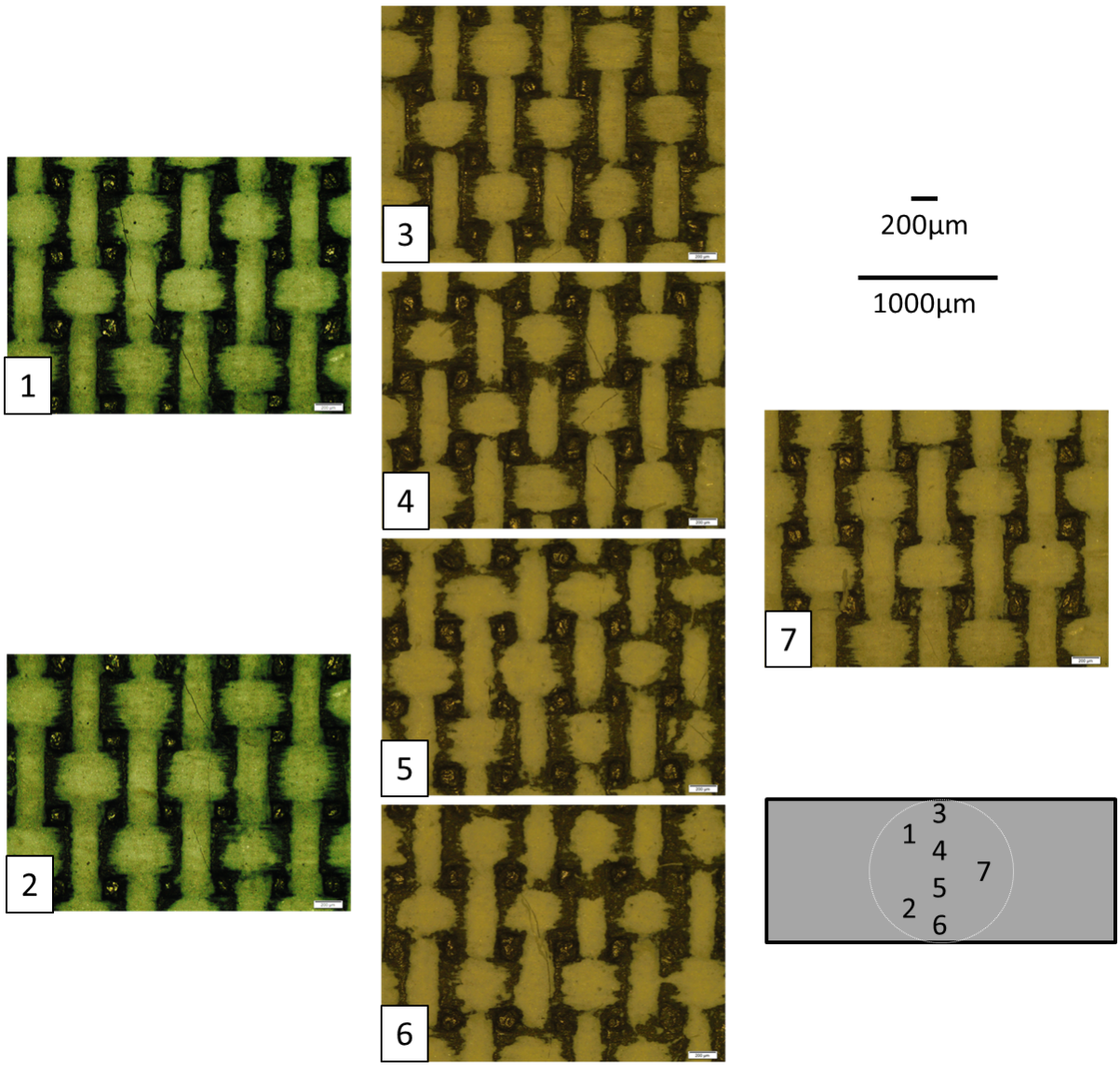

Figure 5.14: Images taken under optical microscopy showing transverse cracks present in the outer-tension ply of Specimen 012-909-3-02. The light regions are remnant paint from DIC patterning, allowing an increase in contrast and easing identification of cracks in the outer matrix layer. Although this image give the appearance of a woven architecture, the surface pattern is due to manufacturing effects. The subfigure at the lower left indicates the approximate location of each micrograph. The white dashed line indicates the location of the loading ring during the test.

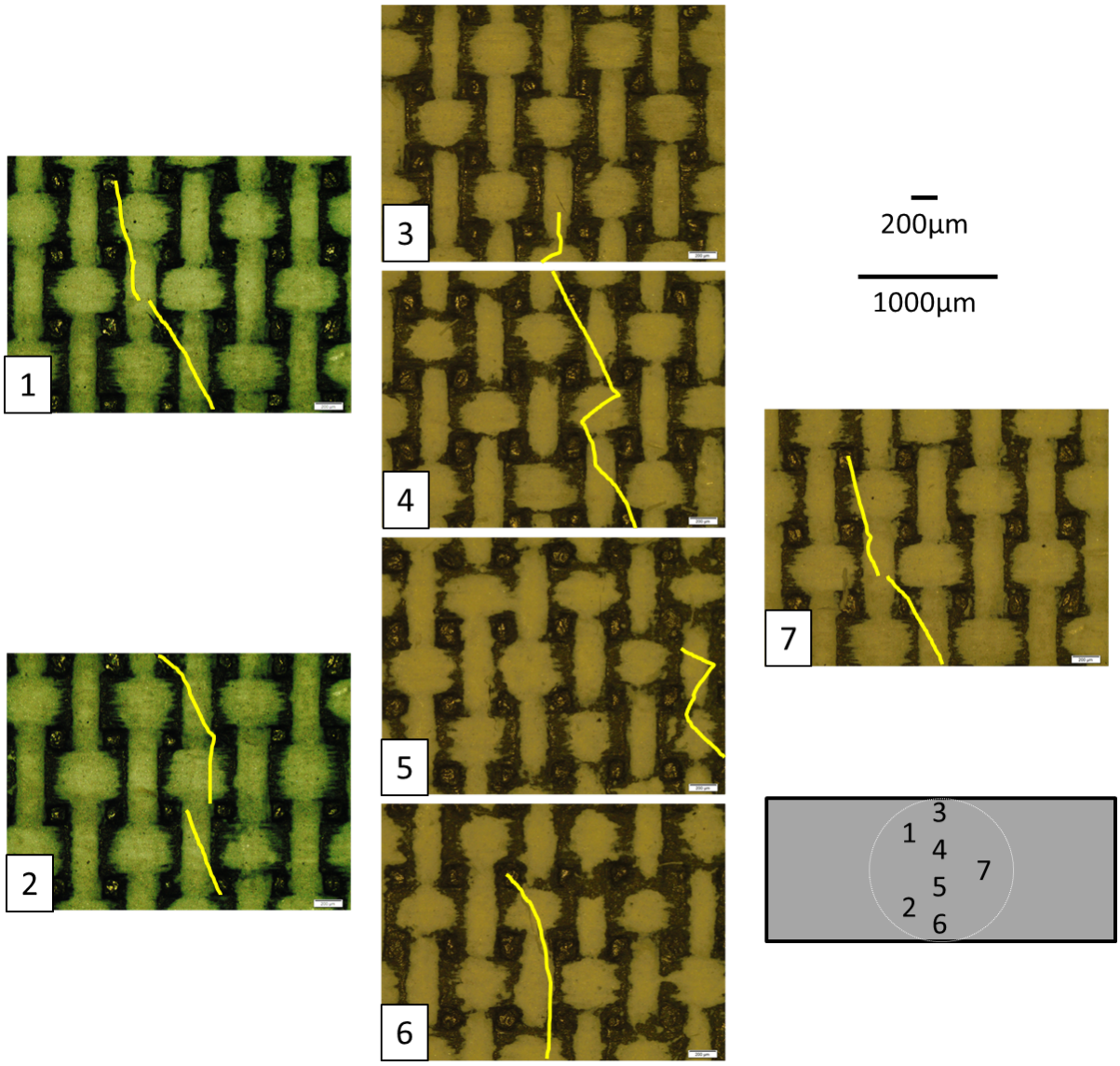

Figure 5.15: Micrographs from Figure 5.14, with cracks highlighted.

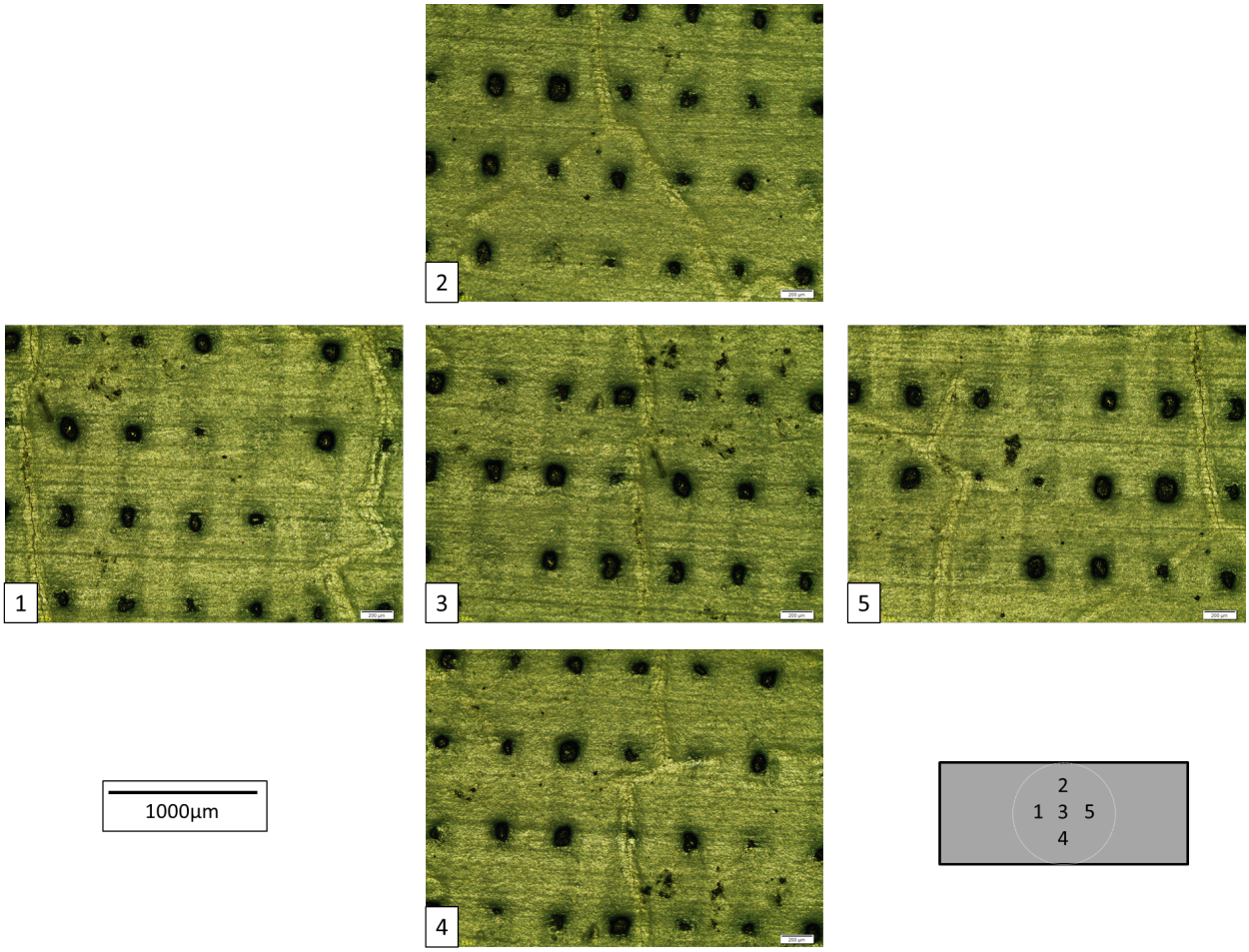

Figure 5.16: Images taken under optical microscopy showing transverse cracks present in the outer-tension ply of Specimen 012-909-3-04. The light regions are remnant paint from DIC patterning, allowing an increase in contrast and easing identification of cracks in the outer matrix layer. Although this image give the appearance of a woven architecture, the surface pattern is due to manufacturing effects. The subfigure at the lower left indicates the approximate location of each micrograph. The white dashed line indicates the location of the loading ring during the test.

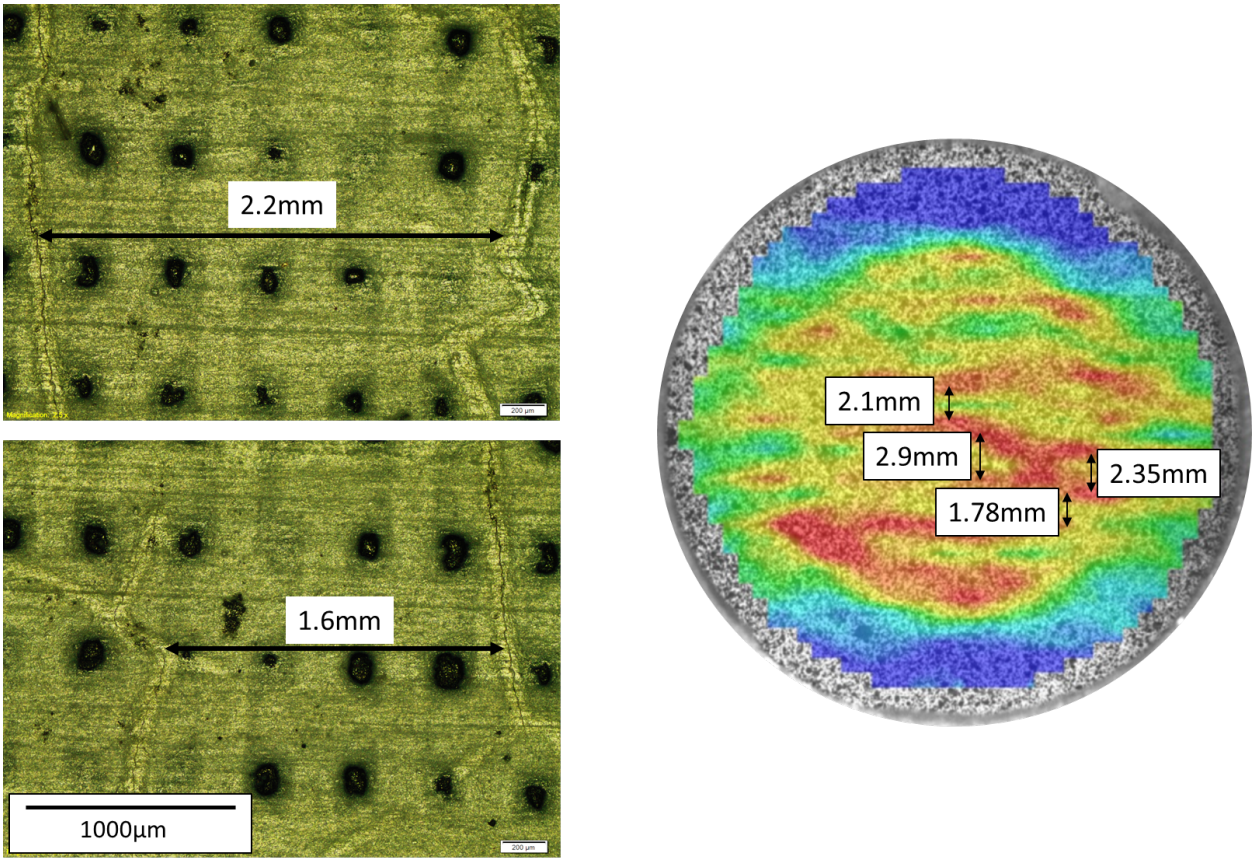

Figure 5.17: A comparison of crack spacing measurements under optical microscopy and high-strain regions identified from DIC measurements. Images from Specimen 012-909-3-4. DIC taken from the last image captured before the loading was aborted. Note the close agreement between strain-localization spacing in both the DIC analysis and optical microscopy.

5.3 Elevated Temperature Testing

To characterize the height temperature response of the composite, biaxial flexure testing was conducted. The tests were performed on an INSTRON Universal testing machine under displacement controlled loading (0.25 mm/min). The fixture is shown in Figure 5.18. The nominal dimensions of this fixture (and specimens) are the same as used in the room temperature tests. The specimen drawing is included again here for reference. The applied load was measured using a 5 kN load cell affixed above the upper push rod. Unlike the room temperature tests, DIC was not used in this round of testing due to the lack of a comparable mirror-based setup that could both withstand the high temperatures in the vicinity of the testing furnace while also providing undistorted images that would provide meaningful results. For the elevated temperature testing, only material from the "'new-process"' batch of material was used.

5.3.1 Elevated-temperature results

5.3.1.1 Results at 1315°C

A total of 4 high- temperature tests were conducted at a testing temperature of 1315°C (2400°F). All specimens in this batch of testing fell into the new-process batch category of specimens. The heating cycle was as follows [1]

1) heat to 1315°C in 2 hours

2) hold at 1315°C for ten minutes

3) conduct test (duration 4 min)

4) remove load

5) cool to 23°C in 4 hours.

The load-displacement curves from this batch of tests is shown in Figure 5.21. The key parameters from this test are summarized in Table 5.3.

Specimen ID	Linear Stiffness [N/mm]	Proportional Limit Load [N]	Ultimate Load [N]
2098-01-0226-F-1	5596	1253	2872
2098-01-0226-F-2	5397	1232	2656
2098-01-0227-F-2	5354	1412	2838
2098-01-0227-F-3	4988	1332	2583
Average Value	5334	1307	2737

Table 5.3: Summary of Key Parameters from tests at 1315°C (2400°F)

[1] For specID, an electrical shutdown (causing a furnace shutdown) led to the specimen being subjected to an heating/cooling cycle prior to being reheated to test temperature. The additional heating cycle was a heat to 1300C in 2 hours, prior to the shutdown, followed by a cool-down to 23°C in 4 hours, following the shutdown. When power was restored, the specimen was heated and tests according to the protocol given.

Figure 5.18: Testing apparatus used for elevated temperature ring-on-ring biaxial flexure.

Figure 5.19: Close-in view of the elevated temperature ring-on-ring biaxial flexure fixtures.

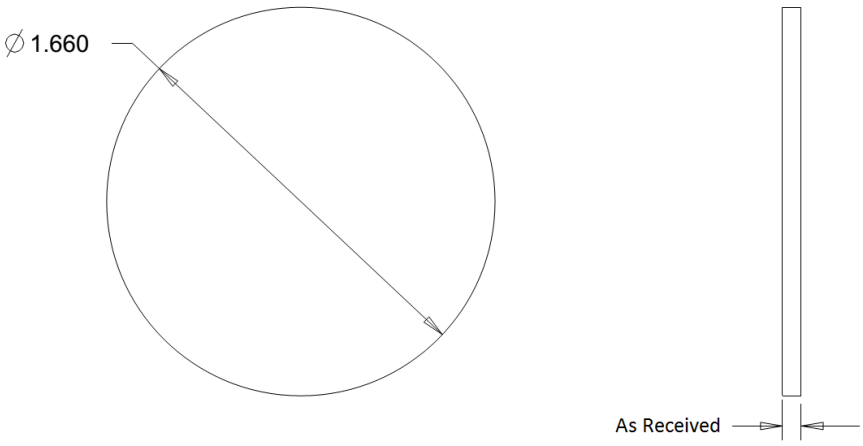

Figure 5.20: Dimensions of the ring-on-ring specimens

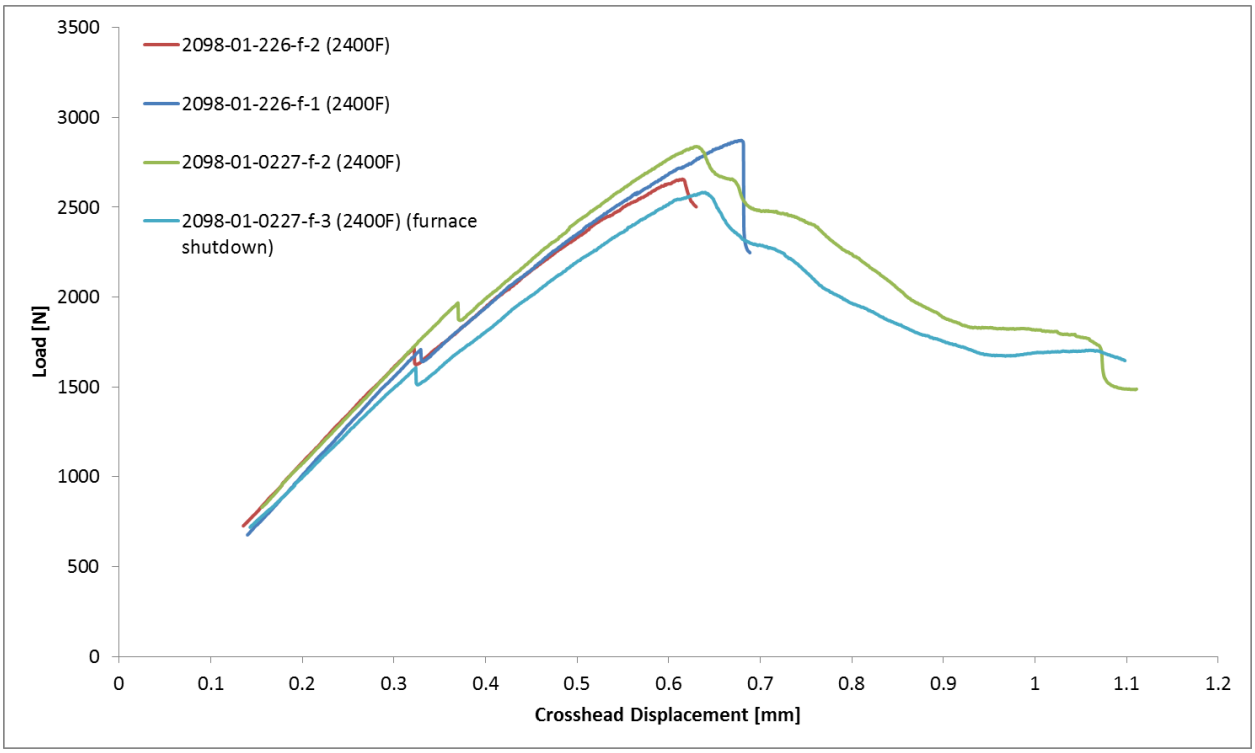

Figure 5.21: Load-Displacement curves from ring-on-ring testing conducted at 1315°C (2400°F): new-process batch material

5.3.2 Elevated-temperature damage investigation

For elevated temperature tests loaded well beyond the peak load, the final form of failure was seen to be a central punch-out, as shown in Figure 5.22. Like the room temperature tests, this took the form of a rough circular crack under the loading ring. The corresponding compression-side crack nearly directly under the loading ring, and has a greater extent along the circumferential direction, as compared to the room temperature test. These cracks are shown in Figure 5.23.

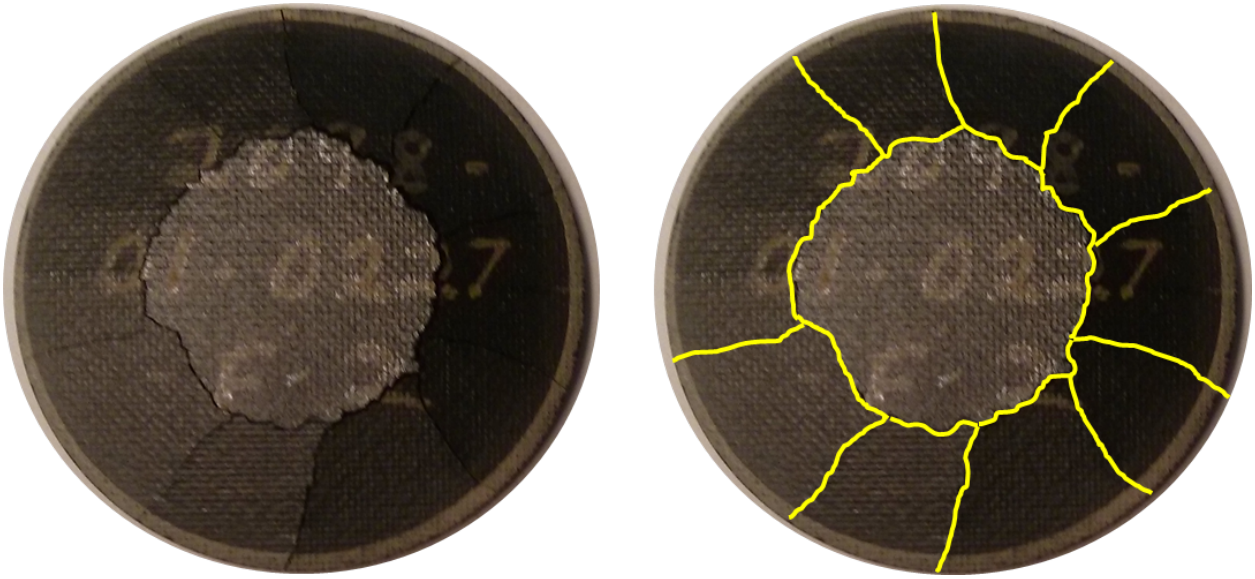

Figure 5.22: Tension side of a typical high temperature specimen, exhibiting a central punch-out failure mode.

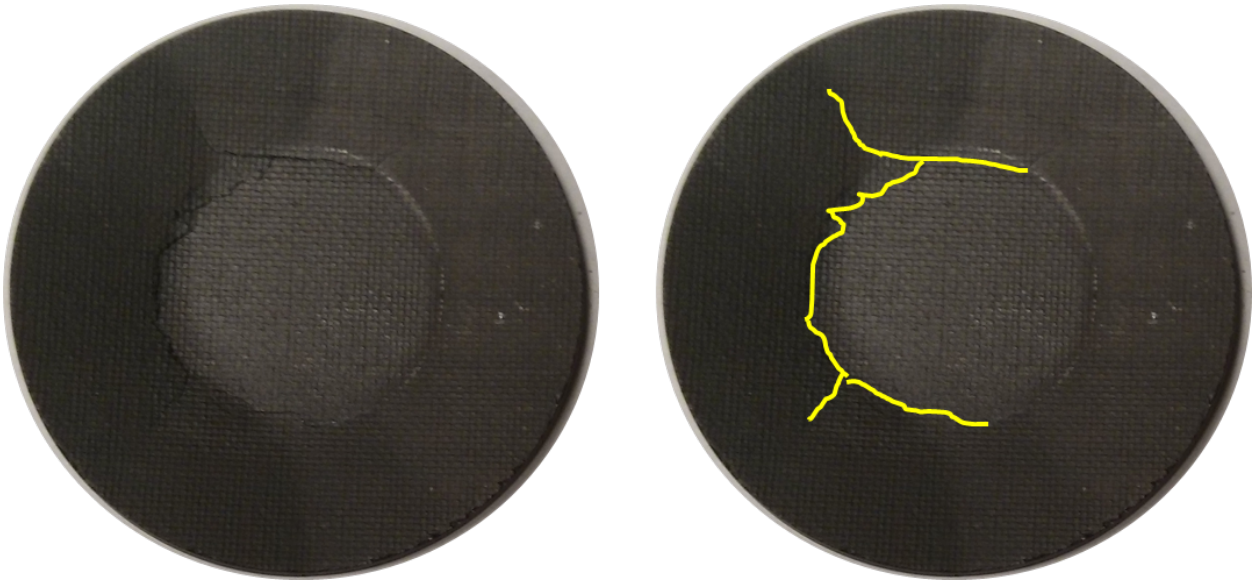

Figure 5.23: Compression side of a typical high temperature specimen.

5.4 Elevated temperature effects

Table 5.4 summarizes the average values of stiffness, proportional limit stress, and ultimate load for the room and elevated temperature experiments conducted on "'new-process batch"' material.

Parameter	Room Temperature Average	High Temperature Average	% Reduction
Stiffness	6394	5334	16.5%
Proportional Limit	1919	1307	31.9%
Ultimate	5223	2737	47.6%

Table 5.4: Reduction in Properties under elevated temperature conditions

5.5 Effects of residual stress on the biaxial response of CMCs

The manufacturing of CMC specimens results in significant residual stresses at the fiber-matrix level. This residual stress state results in a compressive state of stress in the matrix and a tensile stress in the fiber. The effects of these stresses on the response of the composite under biaxial fixture has been studied by annealing the specimens in a furnace to remove as much of this residuals stress as possible. Specimens from the new-process batch of material were annealed in a furnace (under atmospheric environment) at a temperature of 1315°C. Heating and cooling were performed in a linearly ramped fashion, increasing (or decreasing) by 25C per minute. In this study, both standard tensile dogbones under uniaxial tension and discs under biaxial flexure are considered. The tests were performed at room temperature under ambient laboratory conditions.

5.5.1 Characterizing residual stress effects in tensile dogbones

As a point of reference, tensile dogbones (with the dimensions shown in Figure 5.24) were annealed (under atmospheric conditions) at 1315°C (2400°F) for 20 hours. This time and temperature are had been shown to fully anneal the micro-scale residual stresses present in the as-received material [61]. Figure 5.25 shows the stress-strain curves obtained from this round of experiments. Figures 5.26 and 5.27 show two sets of progressive DIC results for a representative as-received and heat-treat specimen, respectively.

The DIC results for both the heat treated and as-received specimens show very similar damage patterns, and the stress-strain curves are of similar shape, indicating that the mode of failure remains the same in both cases. This mode of failure is multiple cracking of the matrix, bridged by the fibers. The heat-treated specimens experience a reduction in proportional limit strength of 15%.

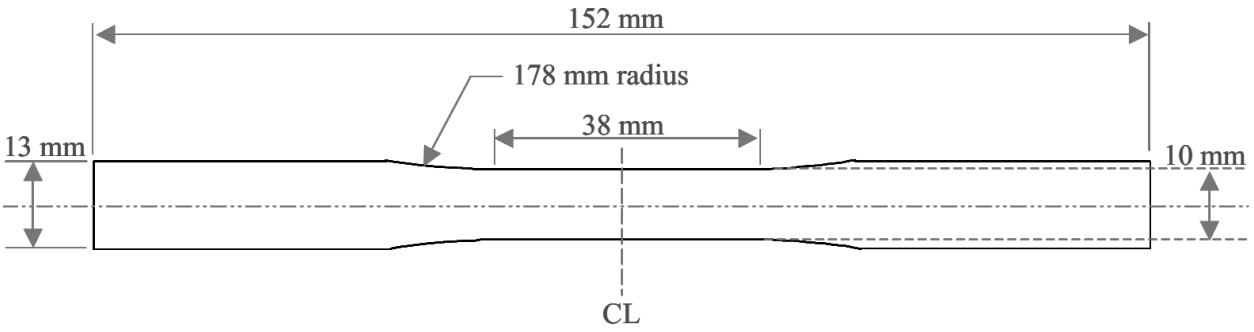

Figure 5.24: Dimensions of the tensile specimens used in the residual stress study [3]

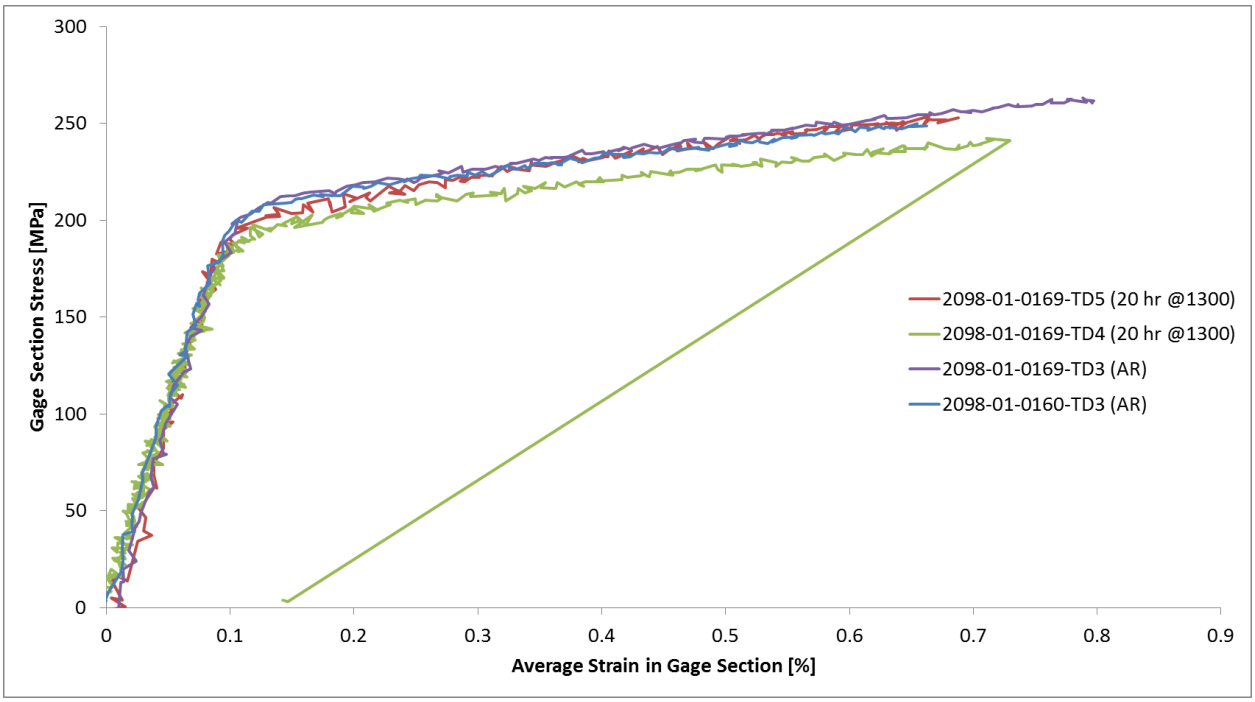

Figure 5.25: Stress-strain curves demonstrating the effect of heat treatment on tensile dogbone results Although the effects are not visually striking, a 15% reduction in proportional limit stress has been determined

Specimen ID	Condition	Proportional Limit Load [N]	Proportional Limit Stress @ PL [MPa]
2098-01-0160-TD2	As-received	2615	144.6
2098-01-0160-TD3	As-received	2944	162.8
2098-01-0169-TD3	As-received	3229	178.5
Average			162.0
2098-01-0160-TD1	Annealed	2958	163.6
2098-01-0169-TD4	Annealed	2734	151.2
2098-01-0169-TD5	Annealed	1765	97.6
Average			137.5

Table 5.5: Summary of Key Parameters from tensile tests at room temperature

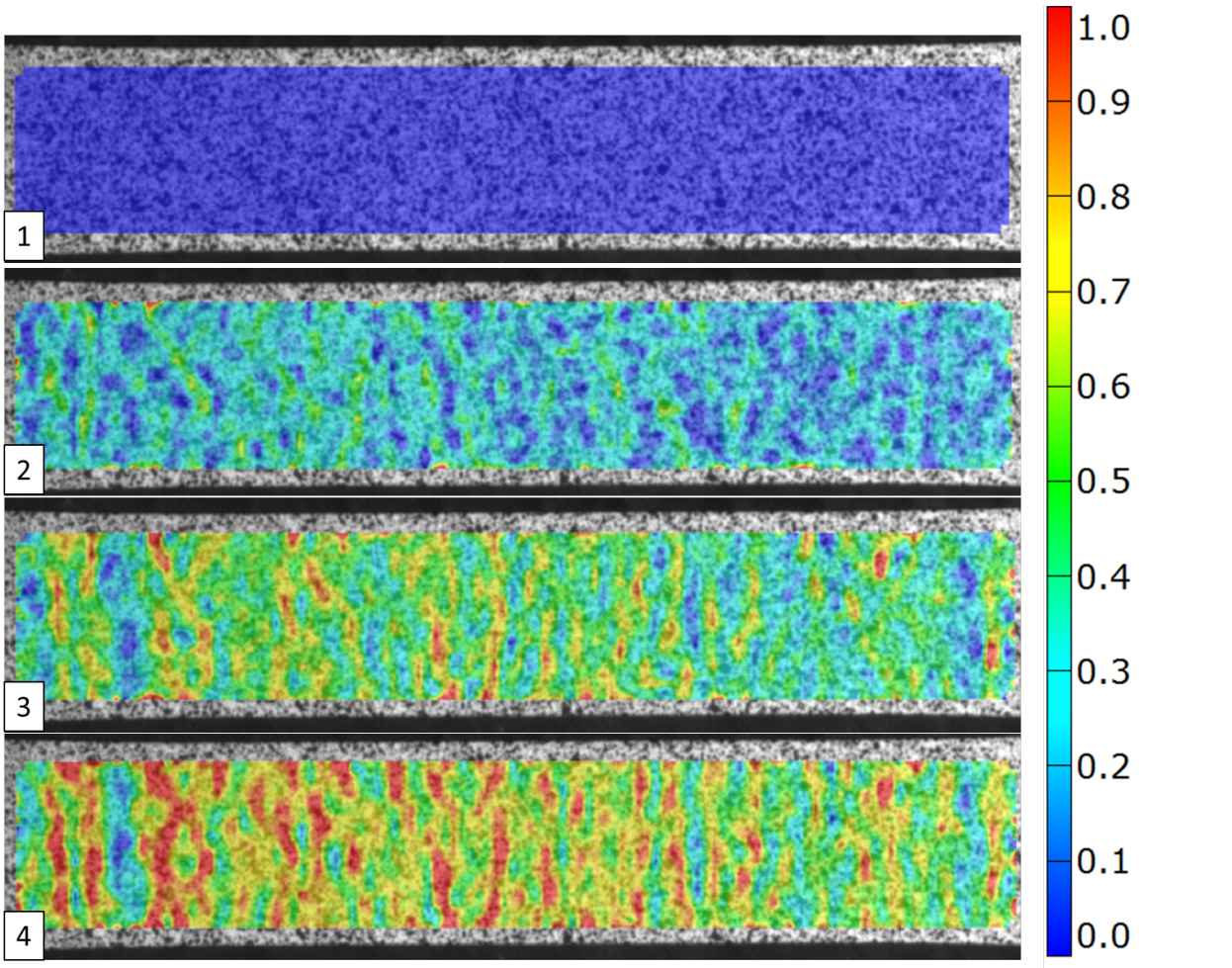

Figure 5.26: DIC results for a representative tensile dogbone test of an as-received specimen

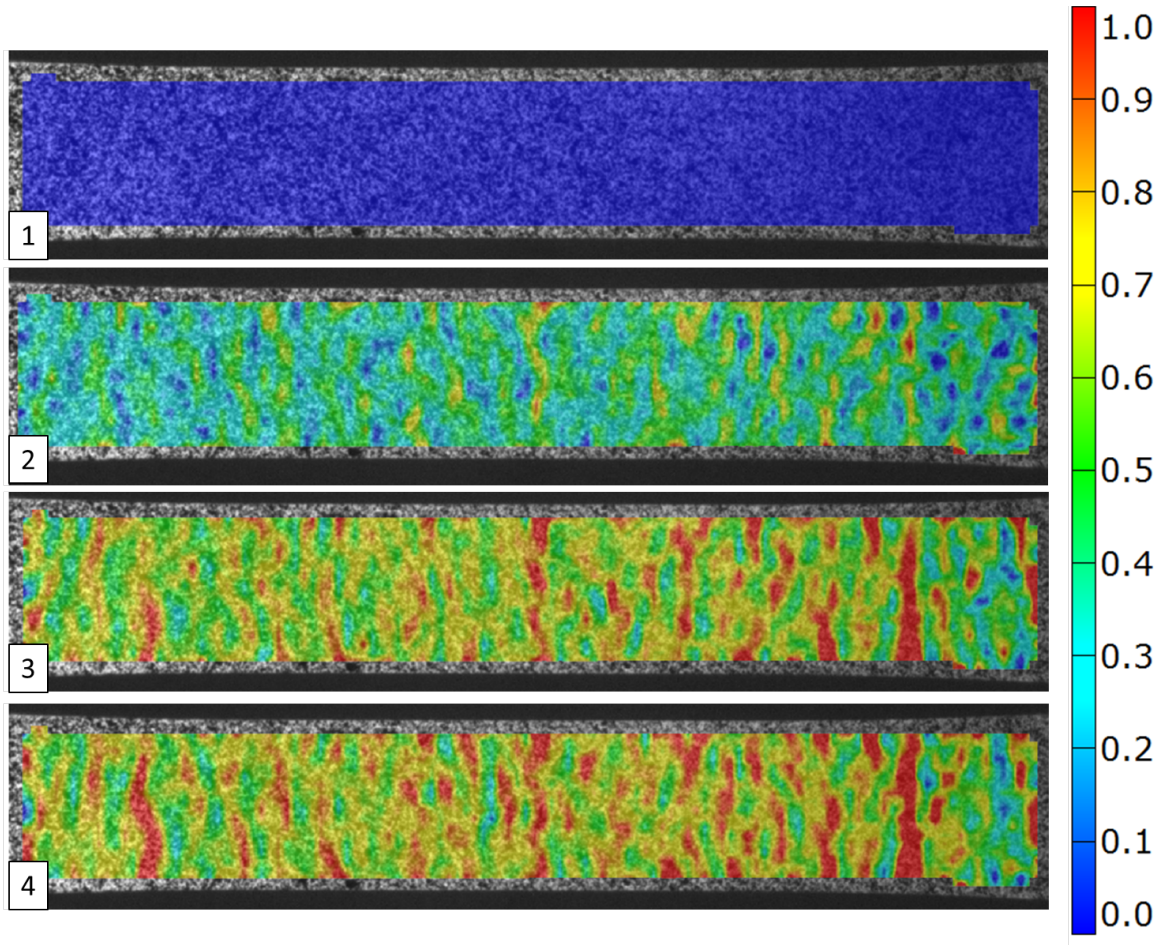

Figure 5.27: DIC results for a representative tensile dogbone test of a heat-treated specimen

5.5.2 Characterizing residual stress effects in flexure specimens

To characterize the effects of residual stress on the biaxial response of the composite, several ring-on-ring specimens from the same process batch of material were subjected to the same heat treatment as the dogbones in the previous section. These specimens were annealed (under atmospheric conditions) for 20 hours at 1315°C (2400°F). Specimens were then tested under ring-on-ring biaxial flexure. Load-displacement curves from these tests are shown in Figure 5.28. Representative DIC plots for as-received and heat-treated specimens are shown in Figures 5.29 and 5.30, respectively.

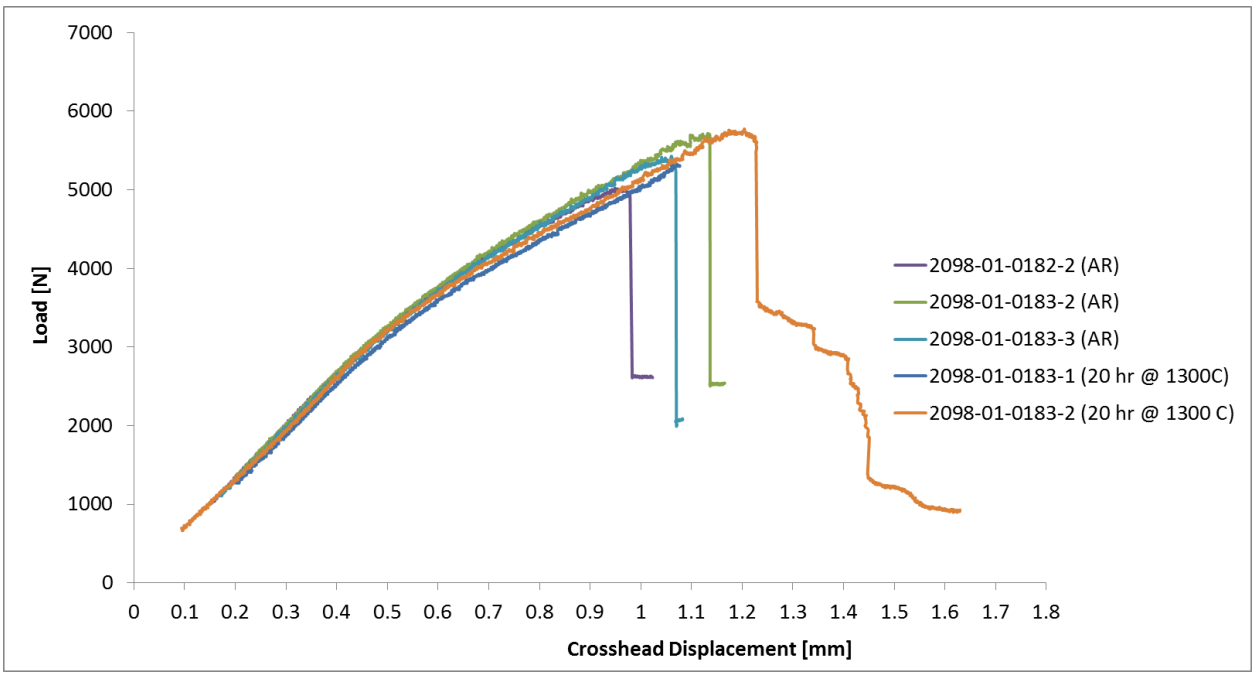

Figure 5.28: Load-displacement curves demonstrating the effect of heat treatment on tensile dogbone results

At first glance, there does not appear to be a strong difference between the as-received and heat-treated flexure response curves. However, a more careful analysis does reveal a decrease in proportional limit load of 13%. From the DIC plots Figures 5.29 and 5.30, the damage mode between the as-received material and heat treated material appears to be similar. From the load-displacement curves, it appears that the biaxial response of the composite is slightly less strongly affected by the residual stress state than is the tensile response. The reduction in fiber-direction stress in the tension side ply at the proportional limit under biaxial flexure is only 13%, compared to 15% for the uniaxial tests

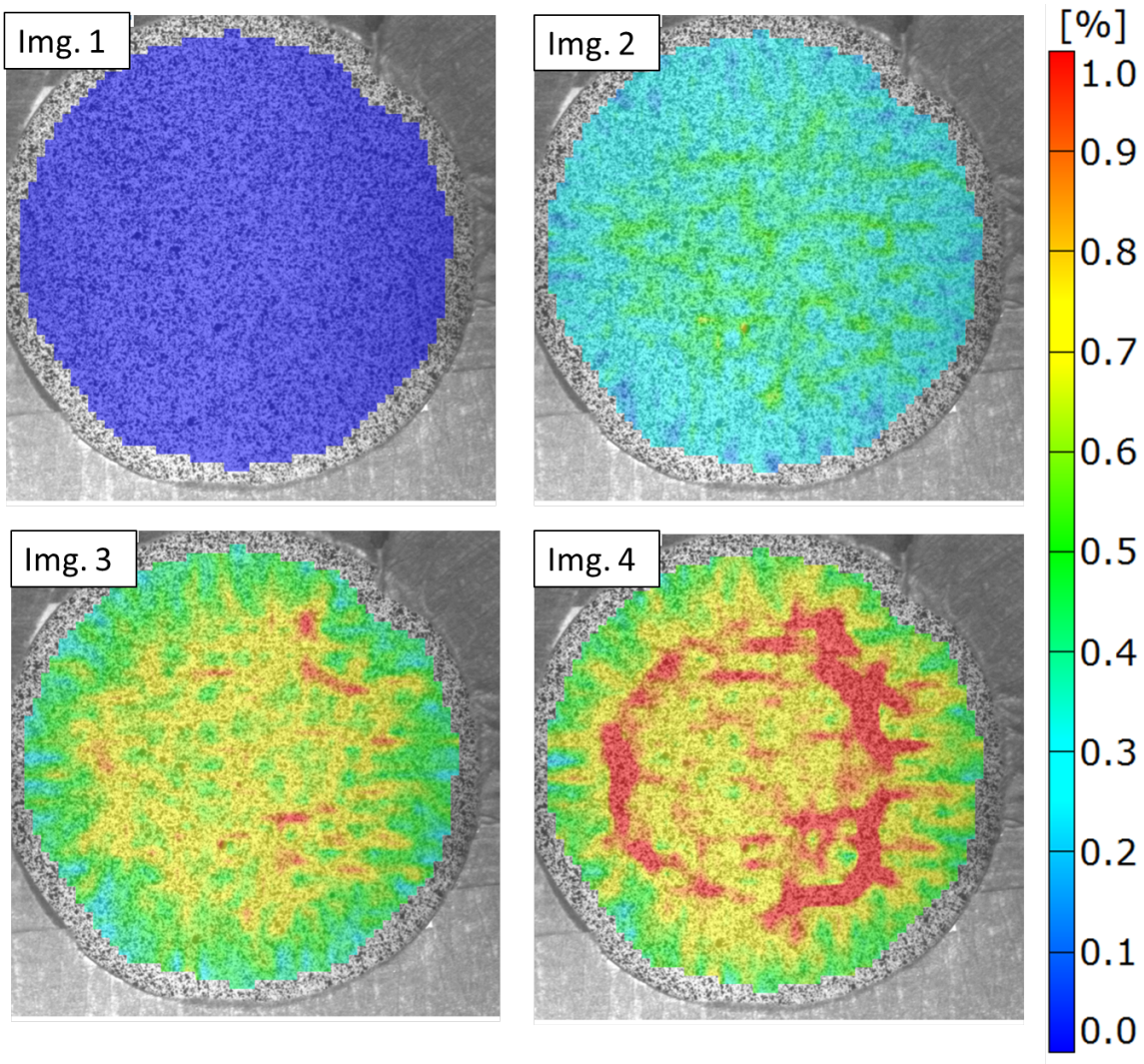

Figure 5.29: DIC results for a representative flexure test of an as-received specimen

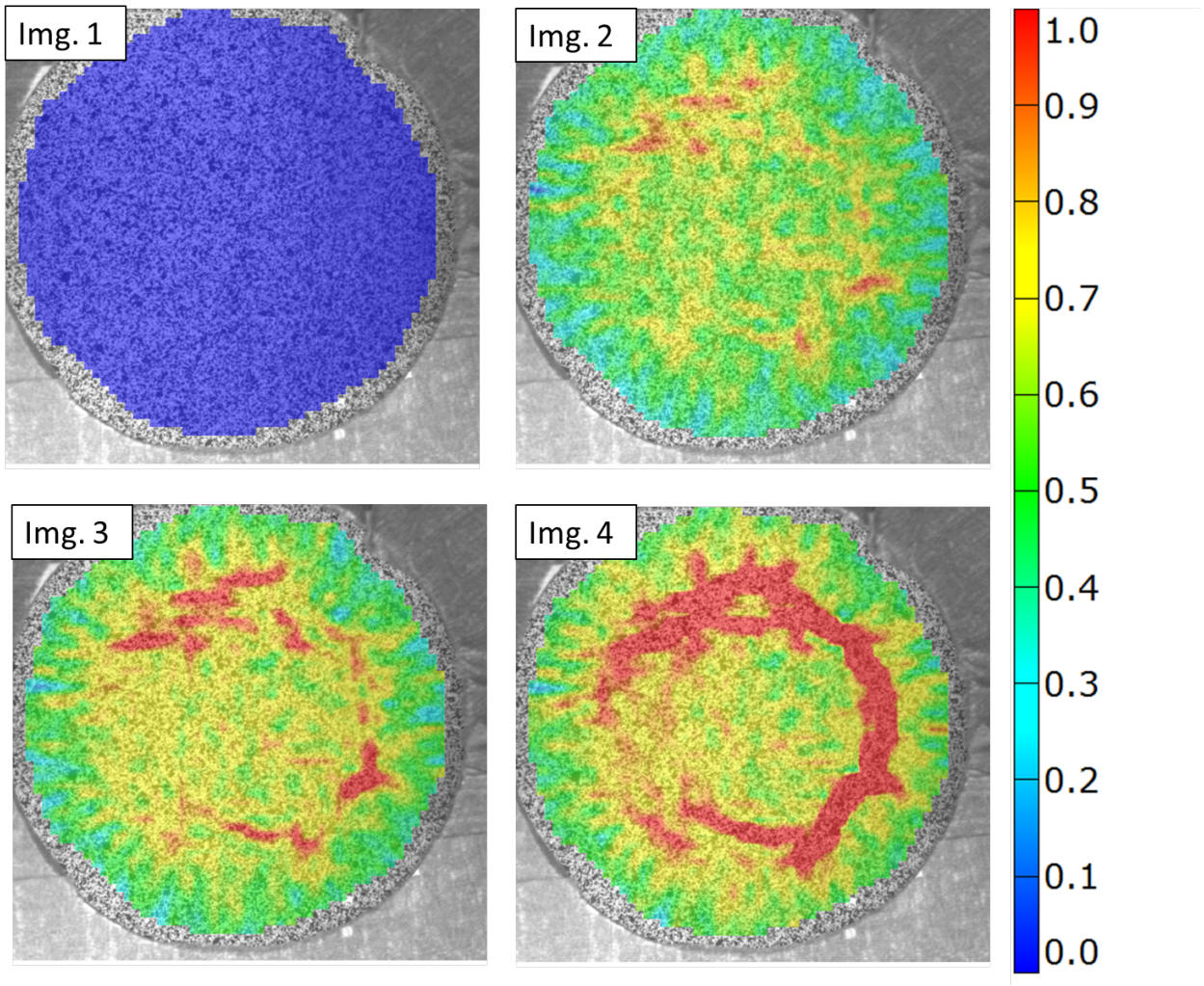

Figure 5.30: DIC results for a representative flexure test of a heat-treated specimen

5.6 Determination of constituent failure criteria from experiments

Ply-homogenization or laminate homogenization scheme require the determination of complex failure criteria for the ply (or laminate) to be used in failure analysis. There are many such criteria; some common ones in the literature include Hill [62, 25], Tsai-Hill [63], and Tsai-Wu [24]. However, the goal of this research is to determine much simpler constituent level criteria to be used in a multiscale analysis. The fiber in use is a well documented fiber [55, 64, 65], and as such any investigation can used strength values available in the literature as a starting point in such analyses.

The matrix, however, is a less well documented material. The detailed behavior of the matrix will depend on the processing conditions, and as such may be highly variable depending on the resulting composition and grain size, among other possible properties. Therefore, the failure criterion for the matrix must be backed out from experimental data.

To this end, a the simple RUC shown in Figure 5.31 was created in standalone MAC/GMC. The major assumption made in this analysis is that the proportional limit stress of the composite ply is driven by first "'substantial"' matrix cracking. It has been shown [66], that matrix cracking does occur below the proportional limit stress of the CMC. However, due to the size of the subcells used in this analysis, any failure that occurs must affect the stiffness by a measurable amount, and thus, for the failure of these subcells only the later, more substantial events are considered to have any bearing on the response of the composite.

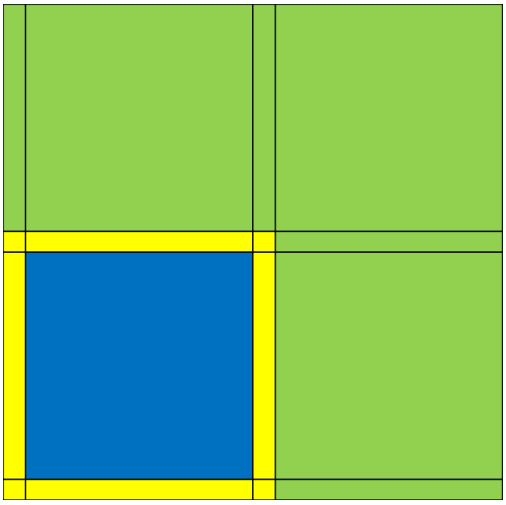

Figure 5.31: RUC used for failure envelope analysis

The candidate failure criteria for the matrix are maximum principal stress and maximum principal strain. Based on the ply-level stress at the proportional limit in a room-temperature tensile test, the worst case stress and strain states in the matrix subcells were determined. The appropriate

value of maximum principal stress (or strain) was then used to construct a failure envelope for each criterion in the tension-tension quadrant. The envelope is shown in Figure 5.32.

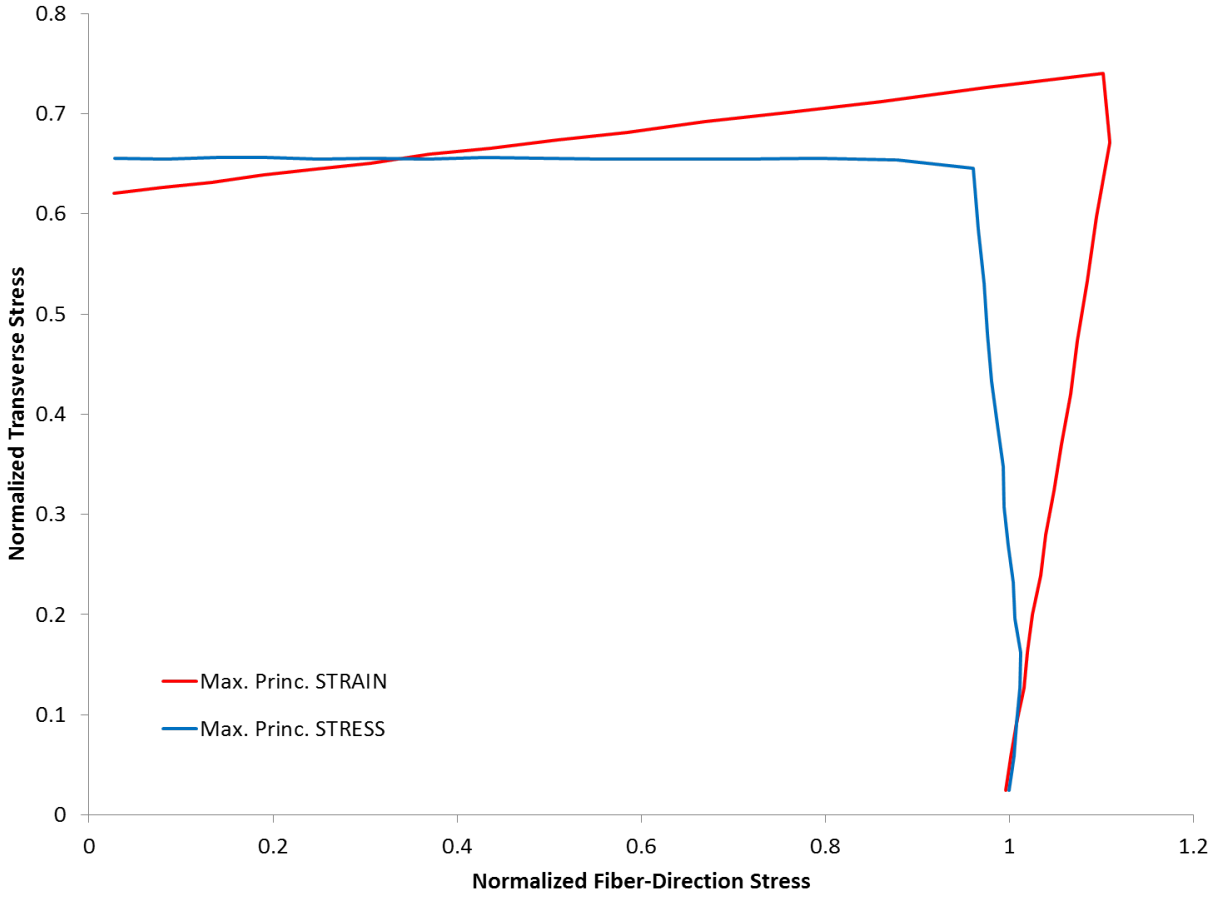

Figure 5.32: Failure envelope for a CMC ply assuming a matrix failure criterion of maximum principal stress and maximum principal strain. This model has been calibrated to the uniaxial proportional limit. Stress values are normalized by the fiber-direction composite stress at the uniaxial proportional limit.

Then, the ply-level stress state at the proportional limit load in the room-temperature biaxial flexure tests was computed, and the stress points plotted against these failure envelopes in Figure 5.33. It is apparent from this figure that using maximum principal stress in the matrix will cause a premature prediction of failure in the biaxial test. The maximum principal strain envelope, on the other hand, falls within the bounds of the experimental data, and thus appears to be the appropriate failure criterion for this material.

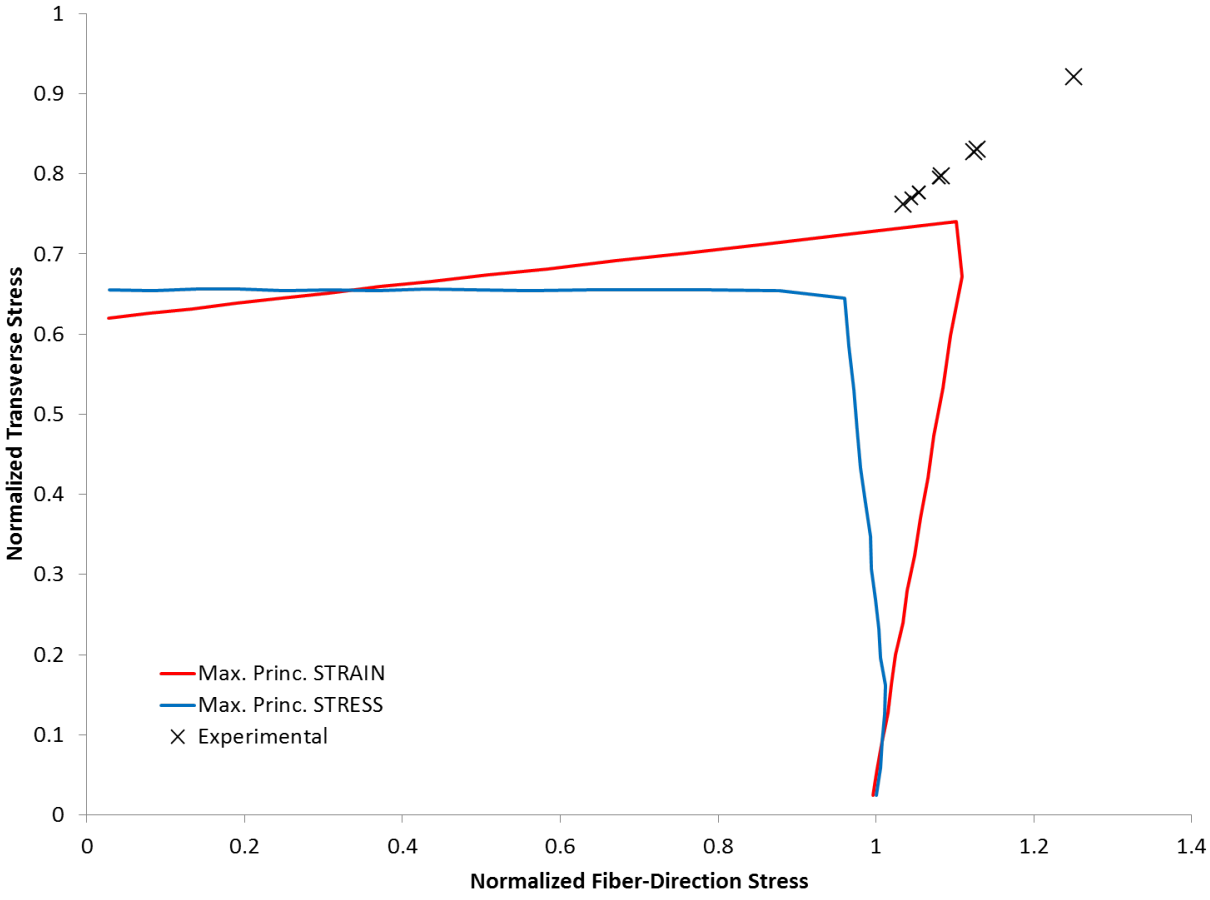

Figure 5.33: Biaxial flexure data plotted on the MAC/GMC failure envelopes. 'X's indicate experimentally determine stresses, as determined from the tension-side ply stresses at the proportional limit.

5.7 Concluding Remarks

A series of experiments has been carried out to asses the behavior of CMCs under biaxial flexure. The average proportional limit load under as-received conditions was determined, and from this, the proportional limit stress state in the tension-side ply was determined. The average PL stress for this material was found to be 317 MPa in the fiber direction, 233 MPa in the transverse direction for room temperature tests. The knockdown factor under elevated temperature conditions of 1315°C was found using a high temperature testing rig. This knockdown factor was determined to be 31.8%. Finally, a set of experiments was carried out to determine the effect of annealing out the residual stress present in the specimen during processing. The annealing of this residual stress reduces beneficial compression in the matrix, allowing fracture of the matrix to occur earlier under loading conditions. For uniaxial tension, annealing was determined to have decreased the proportional limit by 15%. The effect on the biaxial proportional limit stress was slightly lower, with a knockdown factor of 13%.

CHAPTER 6

Results and Discussion

6.1 Comparison of Multiscale Models and Experimental Results

6.1.1 Room Temperature: New Process Batch

Figure 6.1 contains the experimental and simulated load-displacement curves under room temperature test conditions. The multiscale model slightly over-predicts the stiffness, and significantly over-predicts the proportional limit. The post-PL response, however, appears to have a slightly lower slope than that of the experiments, indicating that the onset of failure has been artificially delayed, but the effects of this failure tend to proceed faster than the experiment. Ultimate load is slightly under-predicted (9%).

Figure 6.2 shows side-by-side pictures of the DIC strains and surface strains at several points on the load-displacement curve. The damage plots are in good agreement with the DIC results from the experiments. In both cases, initial failure occurs slightly inside the loading ring, due to the combination of tension (due to bending) on the tension side of the specimen combined with the thru-thickness shear carried by the material in the vicinity of the loading ring. The final failure is also in good agreement with the experiments. The large radial cracks outside the loading ring are accurately represented, including the fact that these cracks do not line up directly with the fiber orientation.

Figure 6.4 contains the experimental and simulated load-displacement curves under room temperature test conditions. The multiscale model slightly over-predicts the stiffness, and significantly over-predicts the proportional limit. The post-PL response, however, appears to have a slightly lower slope than that of the experiments, indicating that the onset of failure has been artificially delayed, but the effects of this failure tend to proceed faster than the experiment. Ultimate load is slightly under-predicted.

Figure 6.5 shows side-by-side pictures of the DIC strains and surface strains at several points

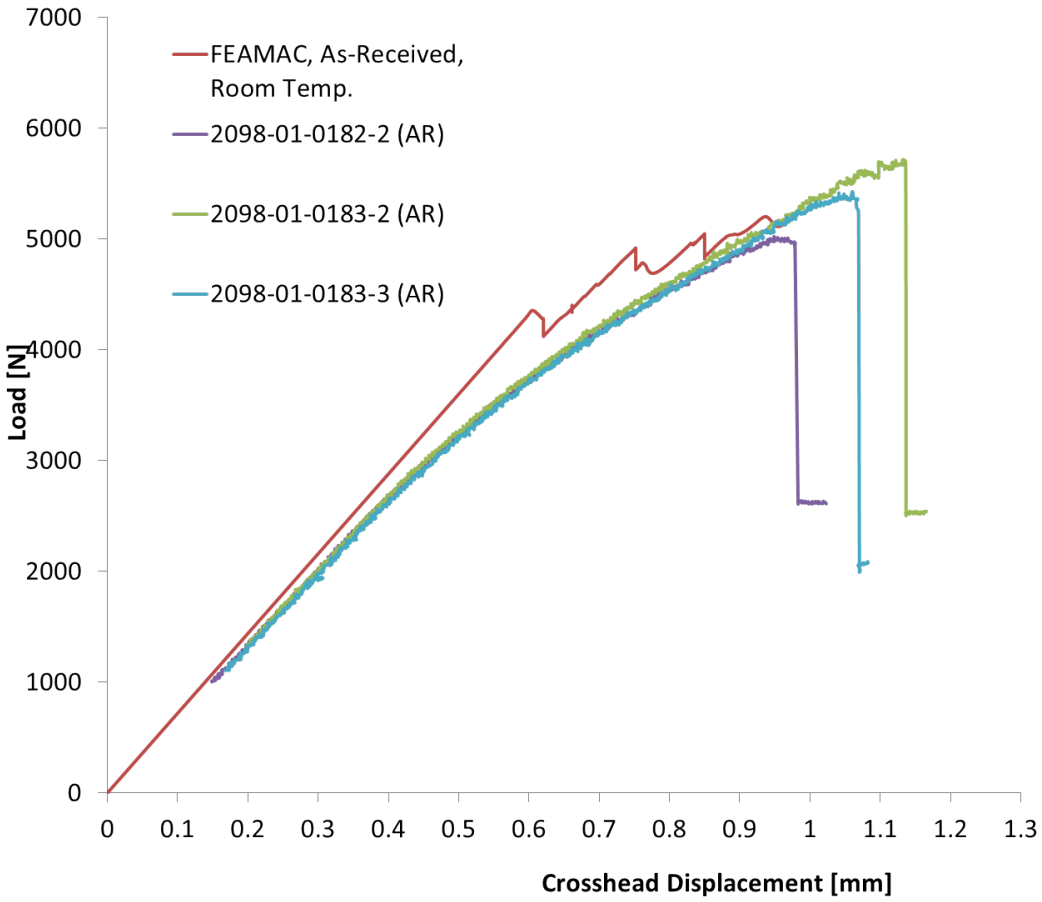

Figure 6.1: Experimental and simulated load-displacement curves for room temperature tests using "'new process"' batch material, as-received condition.

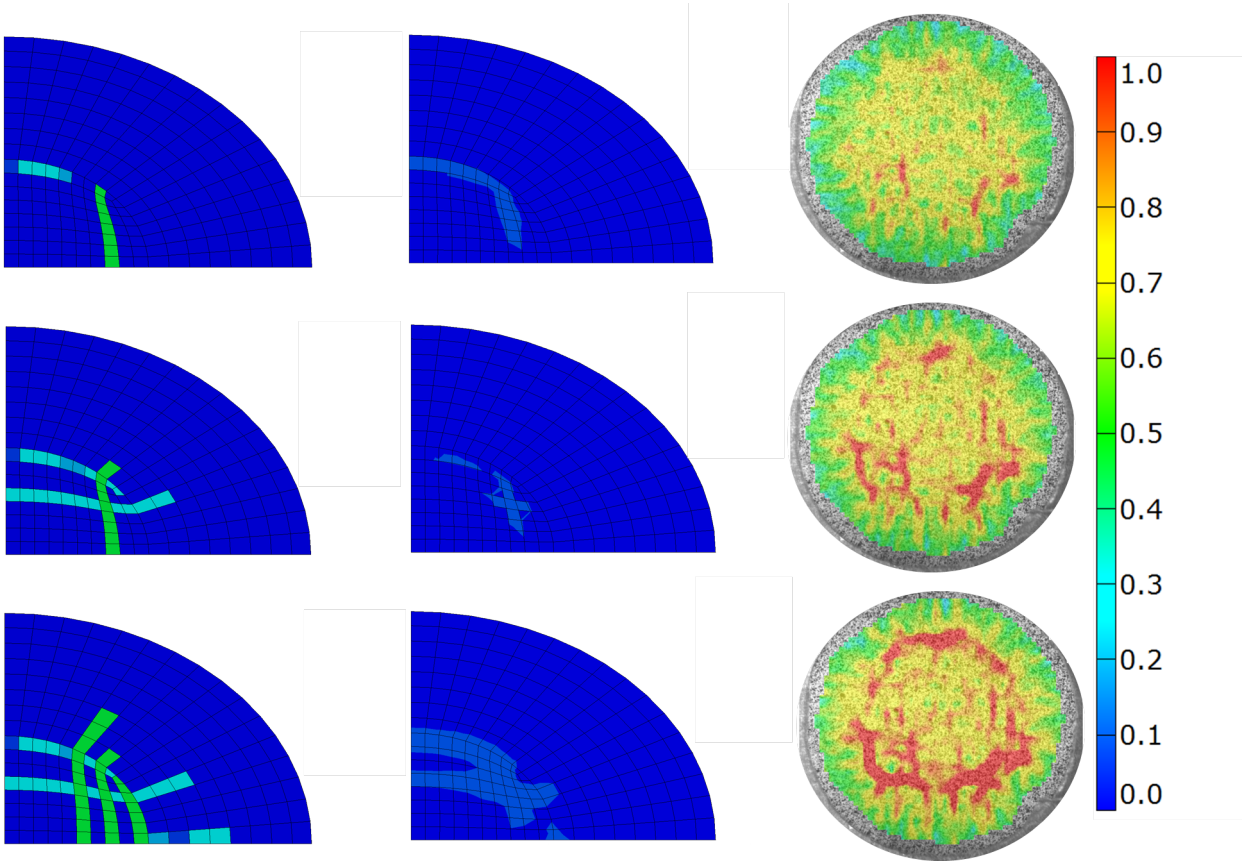

Figure 6.2: Experimental (right) and simulated (center) surface strains for room temperature tests using "'new process"' batch material, as-received condition. Contours show maximum principal strain. Simulated damage plots included at left for reference. Surface fibers are running horizontally in all images.

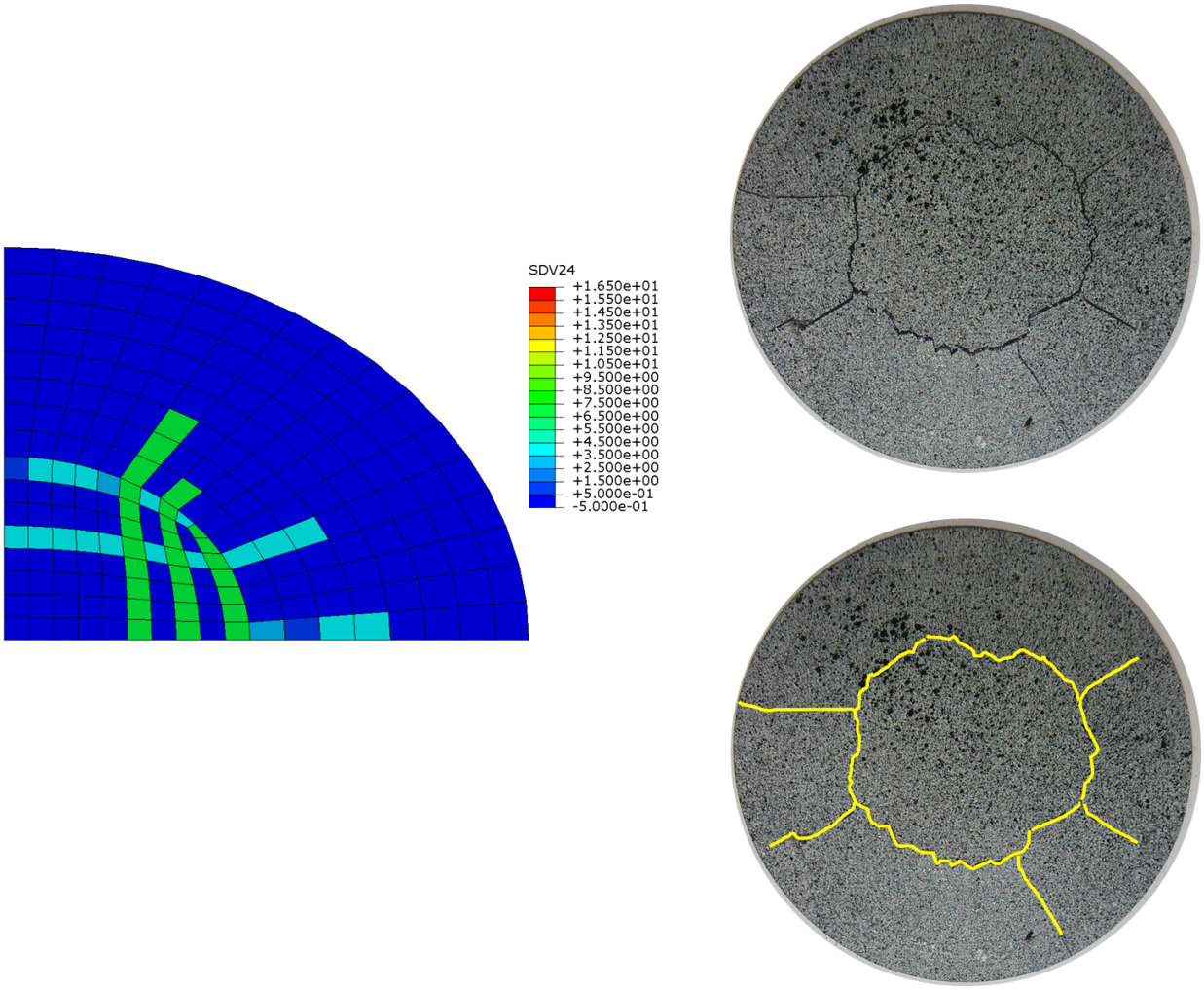

Figure 6.3: Experimental and simulated final damage patterns for room temperature tests using "'new process"' batch material, as-received condition.

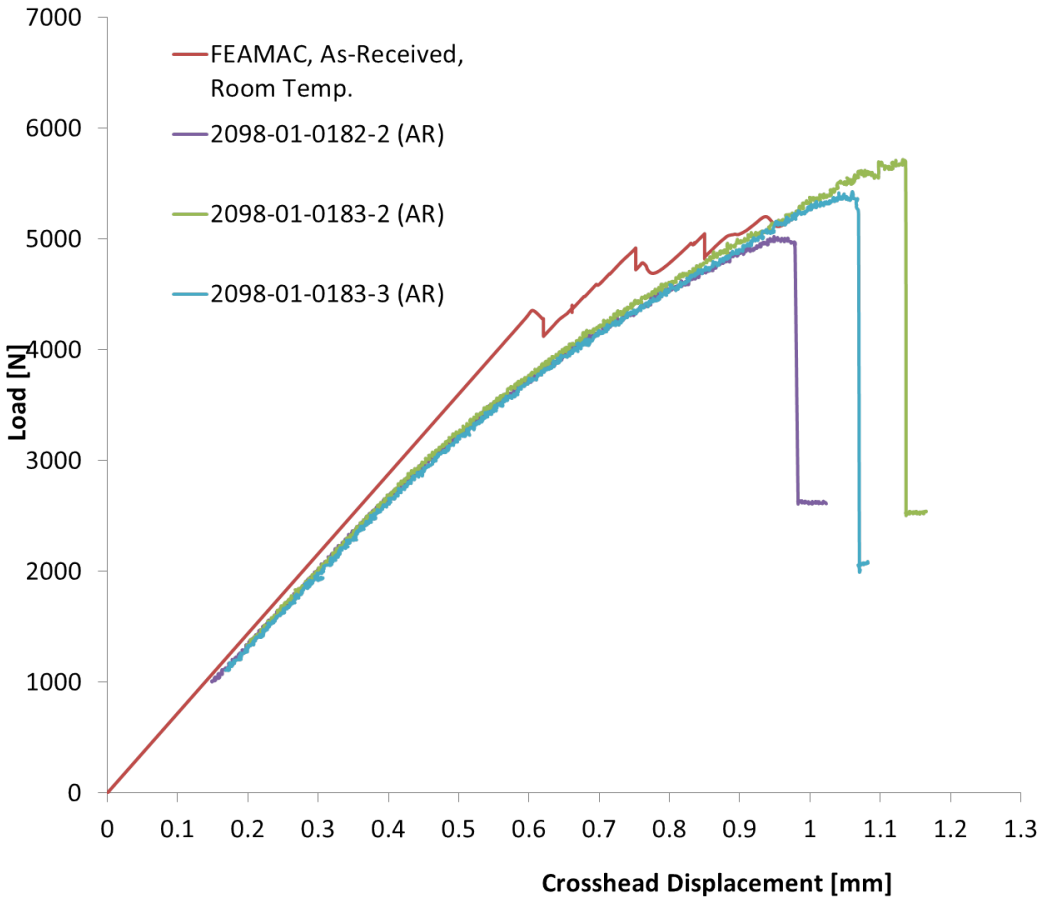

Figure 6.4: Experimental and simulated load-displacement curves for room temperature tests using "'new process"' batch material, annealed condition.

on the load-displacement curve. The damage plots are in good agreement with the DIC results from the experiments. In both cases, initial failure occurs slightly inside the loading ring, due to the combination of tension (due to bending) on the tension side of the specimen combined with the thru-thickness shear carried by the material in the vicinity of the loading ring. The final failure is also in good agreement with the experiments. The large radial cracks outside the loading ring are accurately represented, including the fact that these cracks do not line up directly with the fiber orientation

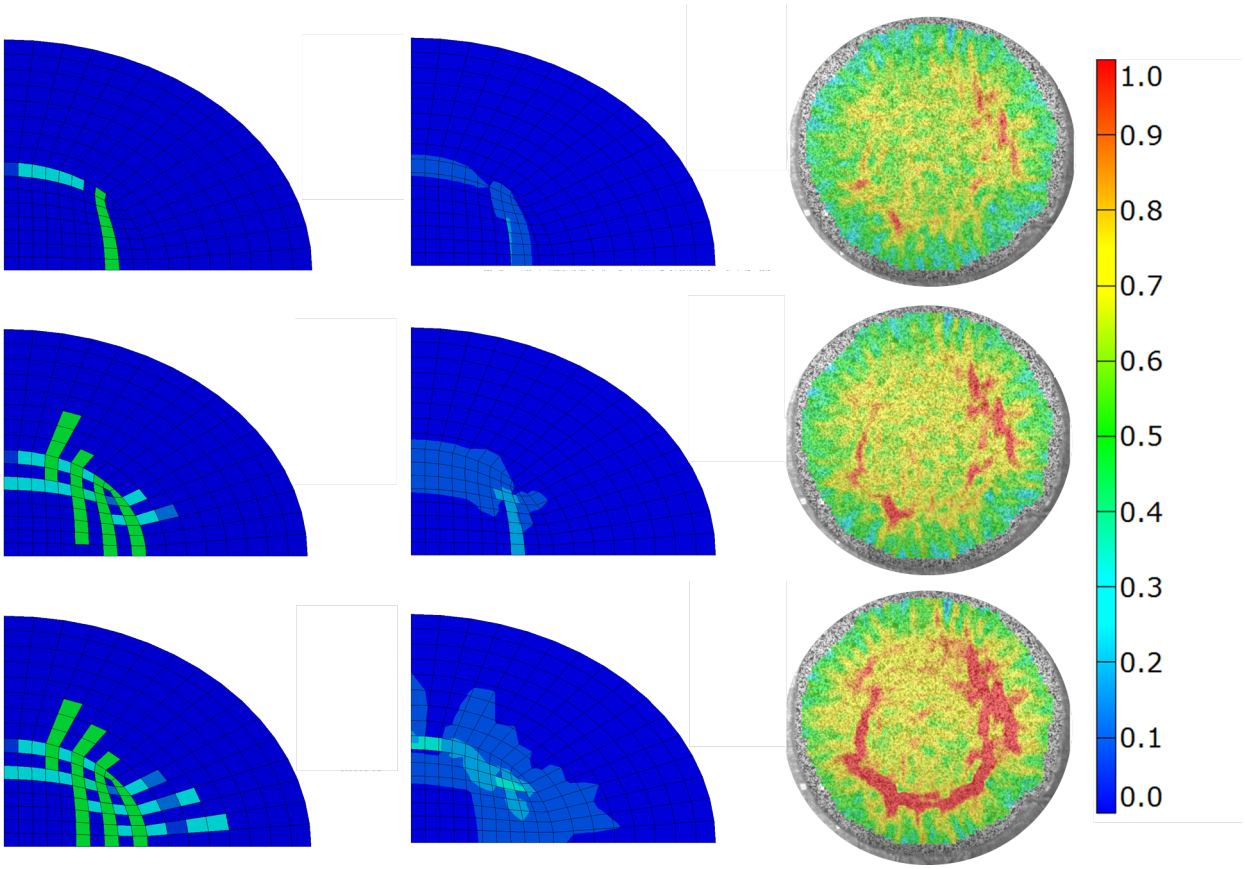

Figure 6.5: Experimental and simulated surface strains for room temperature tests using "'new process"' batch material, annealed condition. Simulated damage plots included at left for reference. Surface fibers are running horizontally in all images.

6.1.2 High Temperature

Figure 6.7 contains the experimental and simulated load-displacement curves under elevated temperature test conditions. Initial stiffness is slightly over-predicted. Further, the simulation does not capture the small drop in load in the early portion of the load-displacement curve. However, the overall response of the composite is well captured. The sharpness of the peak load is slightly

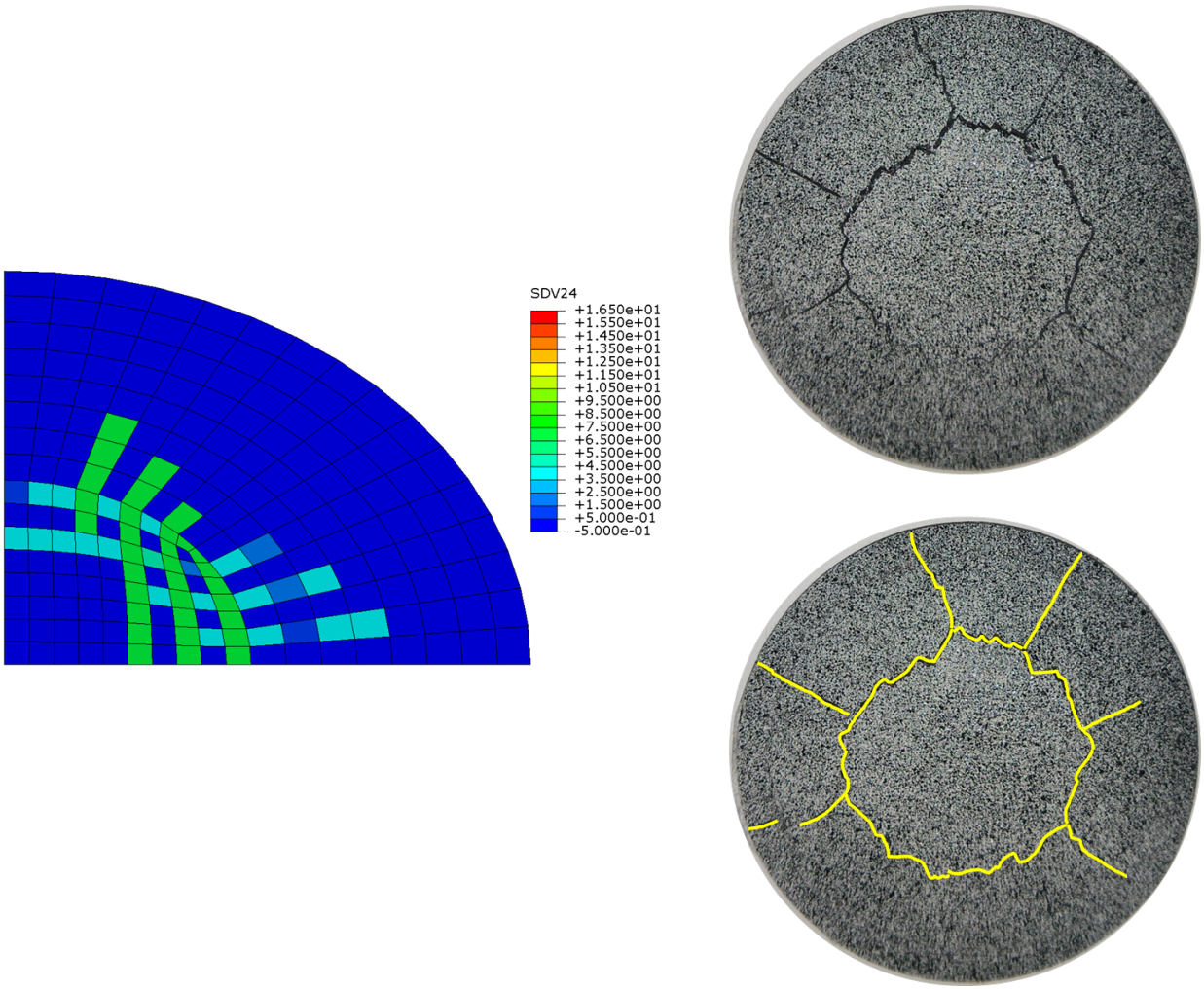

Figure 6.6: Experimental and simulated final damage patterns for room temperature tests using "'new process"' batch material, annealed condition.

rounded, but the peak load itself is within 6%. The drop in load immediately following the peak load is somewhat larger than seen in some of the experiments. However, the aborted test, 2098-01-0227-f-1, does show a more substantial load drop than the other specimens, so this load drop is not outside the realm of possibility. It is thought that the load drop may be due to a lack of fiber pullout, which is more active in high temperature experiments [67].

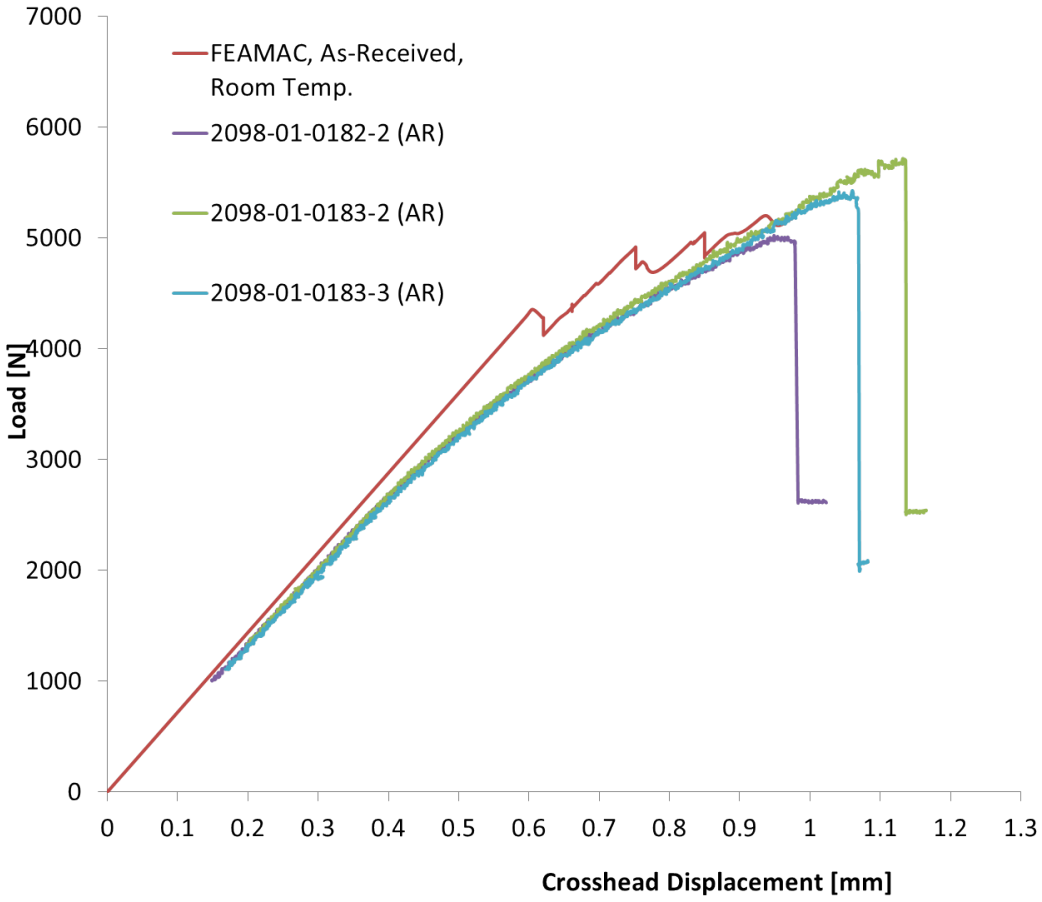

Figure 6.7: Experimental and simulated load-displacement curves for high temperature tests

Figure 6.8 shows the final damage pattern from the experiment and the damage colormaps from the simulation. The simulation predicts a region of damage reaching beyond the gage section in the direction of the fibers. One aborted test did show a large crack running in this direction, as indicated in Figure 6.8. However, the simulation fails to predict the singular nature of this crack, instead spreading the damage over a wide region. This may be due to the increased toughness used for the elevated temperature simulations.

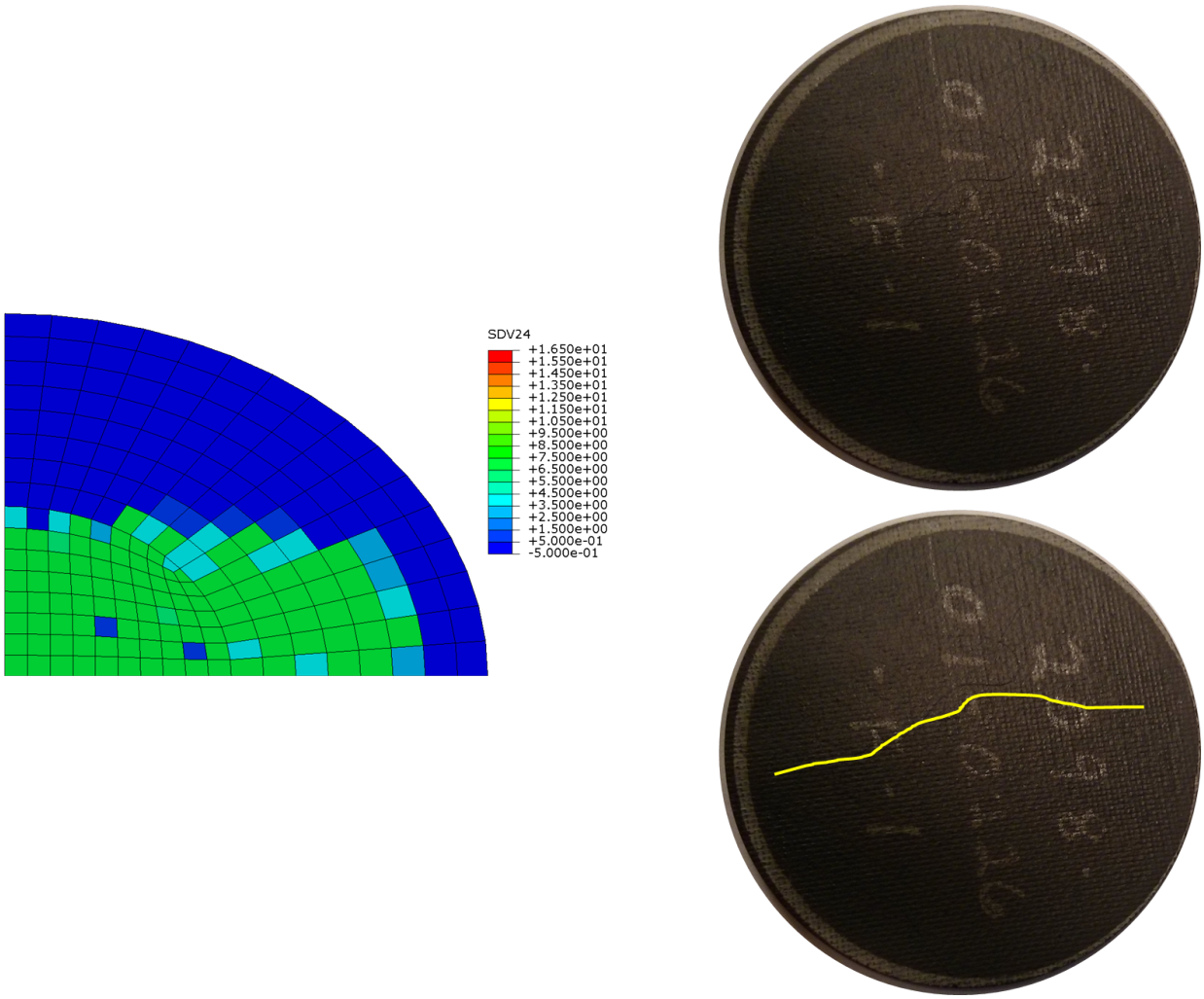

Figure 6.8: Experimental and simulated final damage patterns for high temperature tests. Surface fibers are running horizontally.

6.2 Multiscale Modeling vs. Homogenized Models

Multiscale models provide richer physics than are available in homogenized models, at the cost of increased computational time. Figure 6.9 compares the load-displacement curves obtained from both the multiscale simulation and a Ply-Level Homogenization, Ply-level homogenized (PLH) model utilizing the crack-band model of matrix failure. The PLH model uses the same mesh as the multiscale models for ease of comparison. In this model, the composite is homogenized at the ply level; there is no micromechanical model present. The elastic properties of the homogenized materials are computed using MAC/GMC. The same subcell as the multiscale simulations is used to compute the elastic properties of the homogenized material. Thus, the elastic stiffness of both finite element models is identical: any differences between the models is due entirely to the change in failure and post-failure behavior of each model. redThe post-failure behavior of the PLH model is an implementation of the smeared crack model. The initial failure strain in all direction is matched to the initial fialure strain in the FEAMAC model.

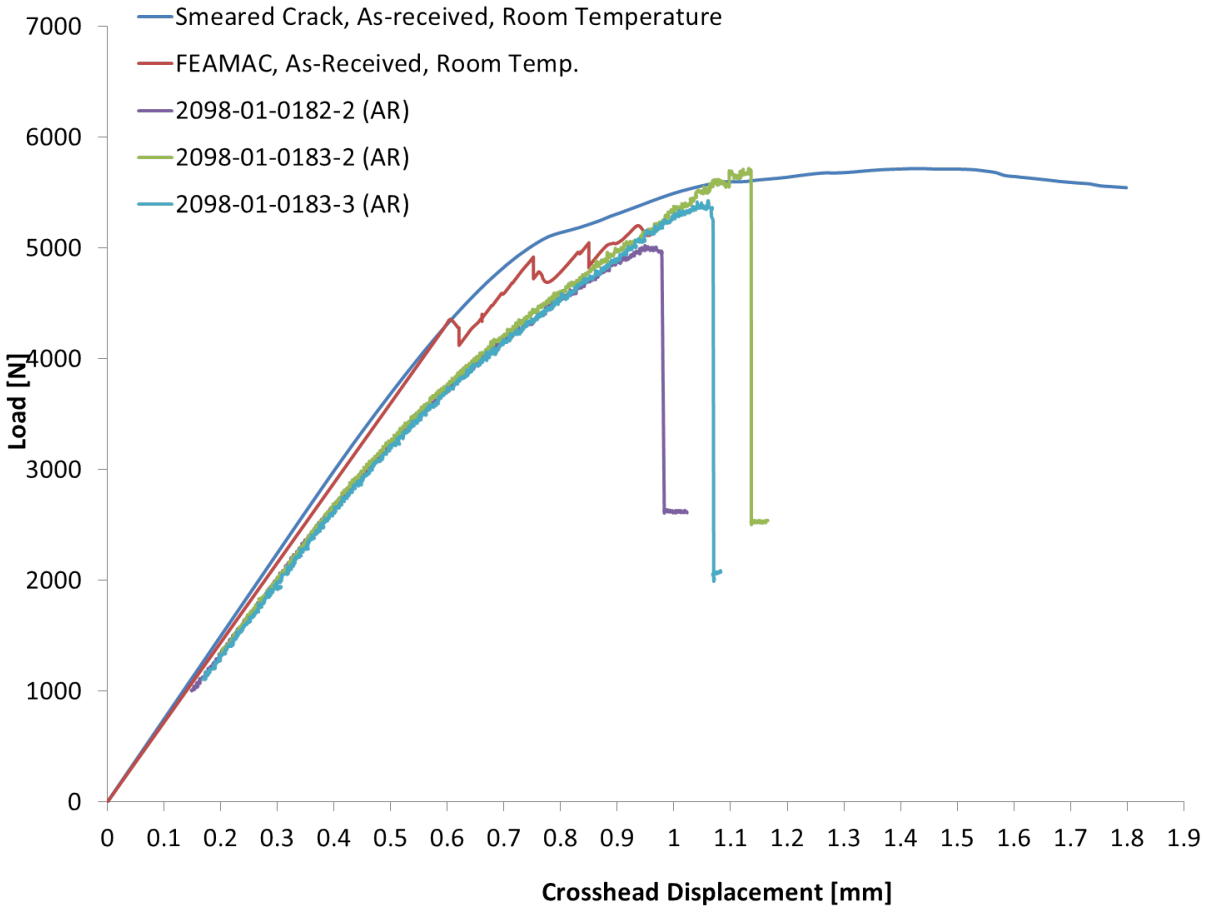

Figure 6.9: Load-displacement curves from the multiscale and PLH simulations for room temperature simulations in the as-received condition

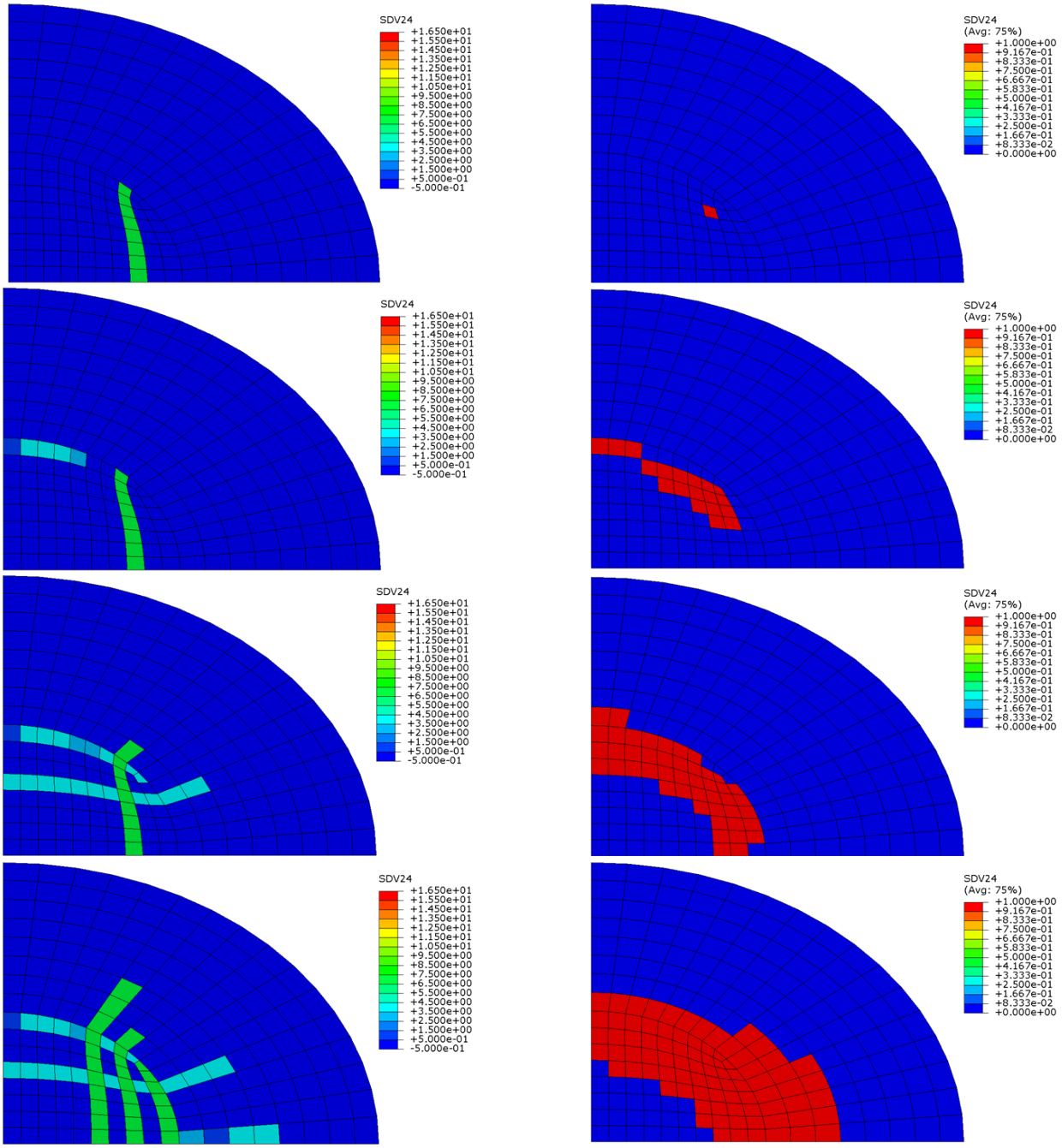

Figure 6.10: Colormaps of damaged elements from the multiscale (left column) and PLH (right) simulations for room temperature simulations in the as-received condition

A similar set of simulations were done for the simulations of the high temperature tests.

These figures show that the multiscale approach provides a much more realistic load-displacement curve. After the peak load is reached, the load drop is able to occur due to fiber failure. This does not occur in the smeared crack model, despite having the same total strain-to-failure as the multi-scale RUC. However, the more striking difference is in the pictures containing the failed subcells.

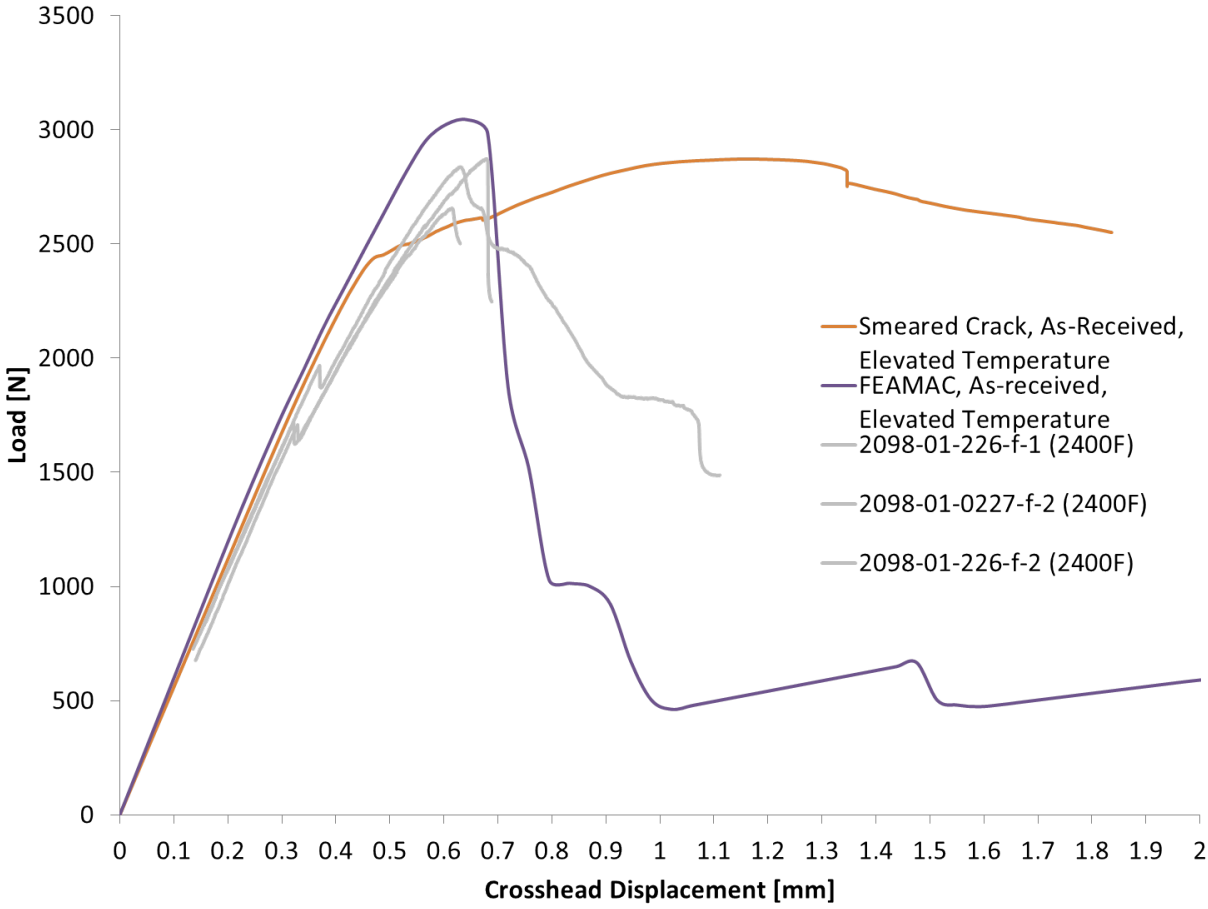

Figure 6.11: Load-displacement curves from the multiscale (left column) and PLH (right) simulations for high temperature simulations in the as-received condition

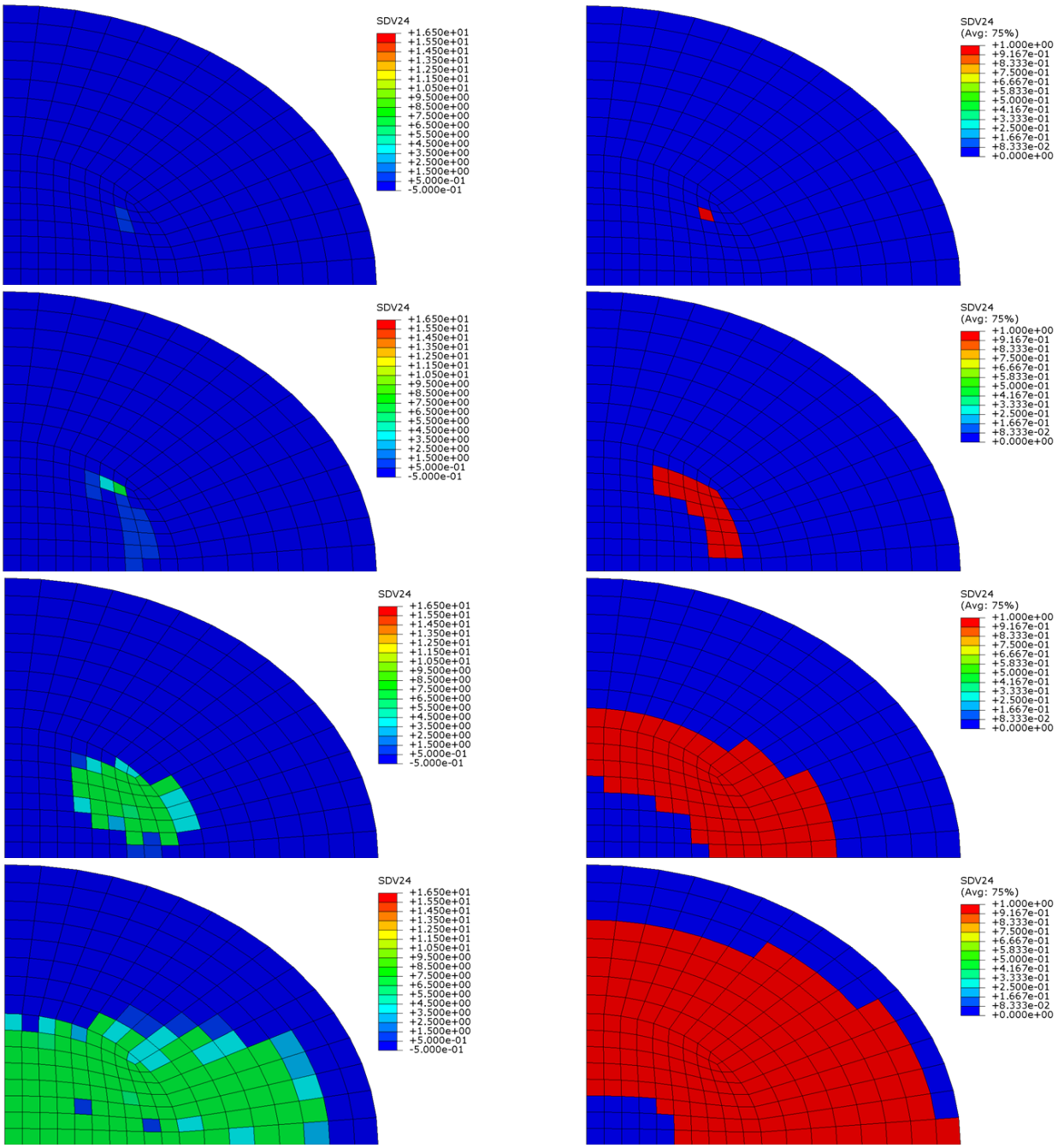

Figure 6.12: Colormaps of damaged elements from the multiscale and PLH simulations for high temperature simulations in the as-received condition

In the PLH modeling scheme, the damage, once initiated, as a tendency to spread out from the damaged region in a fairly uniform fashion. By contrast, the multiscale models have much more discrete damage patterns, with individual cracked regions extending to the perimeter of the specimen once damage spreads beyond the gage section. Further, the details of the initial damaged region near the loading ring is different. Where the multiscale simulations show a single crack normal to the fibers initially occurring inside the gage section, the PLH model shows slightly more of a "'punch-out"' type of behavior. These differences would be critical in future analysis of oxidation or corrosion in specimens or parts exposed to hot, oxygen or water containing environments.

CHAPTER 7

Summary and Future Work

7.1 Summary of Contributions

Two micromechanical models for predicting the properties of laminated CMCs have been presented. The first is a method for determining the elastic constants of an FRC with a thick fiber coating. This method calls for the inclusion of the fiber coating in an explicit manner, and also implements an equivalent homogenous outer phase which posses the properties of the composite being sought. The inclusion of this phase provides for he proper mixed boundary conditions on the composite cylinder: use of a traction free boundary condition underestimates the stiffnesses, and use of a fixed boundary conditions overestimates stiffness. The increased accuracy of this model over other, nested-type models is shown for the material of interest of this research.

The second model is a model of progressive cracking and fiber pullout in FRCs with a brittle matrix and substantial fiber coating. This model has its root in shear lag analysis of FRPs, and expands upon this framework through the inclusion of a coating phase and the inclusion of Mode II cracking along the coating-fiber interface. The progression of damage is handled in a energetic sense, with the cracking of the matrix being primarily driven by the balance of work-of-fracture with the stored elastic energy. The coating cracking (resulting in fiber pullout) is driven primarily by stresses. it is noted that due to the simplifications made in the stress state, the stress concentration does not occur at the crack tip, and a pseudo-strength can be used instead of fracture toughness. The results of this model are then used to inform the longitudinal behavior included in the homogenized and multiscale models.

An experimental investigation of the behavior of CMC laminates under multiaxial load states has been carried out. This was done through the use of biaxial ring-on-ring flexure testing at room- and elevated temperature. Ring-on-ring flexure was chosen for its ease and low cost of specimen manufacturing as well as its extendability to fatigue and creep testing. The room temperature testing allowed for optical imaging of the tension-side ply, which had been treated with a speckle pattern for digital image correlation. a single camera setup was used for this testing, justified by the

need only for information about strain localization, and not for quantitative values of strain. Room temperature testing and subsequent imaging of the post-failure surface revealed that a network of cracks occurs on the tension side ply, and that the specimen carries significant load after cracking begins due to the apparent toughening provided by the fibers. High temperature tests are subsequently carried out, and the reduction in properties due to elevated temperature are quantified. The results of the test are used to evaluate candidate constituent-level failure criteria. Ultimately, maximum principal strain was concluded to be the appropriate failure criterion to use for the matrix. An experimental investigation into the effects of residual stress was also conducted. In this study, tensile dogbones and ring-on-ring discs from similar processing batches were used, Half of these specimens were tested in the as received conditions; the other half were subjected to a 20 hour annealing cycling at 1315°C (2400°F)

A multiscale methodology for testing CMCs has also been developed. The implementation presented in this research was based on the Generalized Method of Cells, as implemented into Abaqus using the MAC/GMC and FEAMAC software suites available from NASA Glenn Research Center. The approach here calls for random variations in subcell geometry to be applied in different elements throughout the structural domain. This prevented the initial site of damage from dominating the response, and thus allowed for many locations to experience damage, accurately representing the distribution of damage in the real CMC specimens. Additionally, a method for implementing the effects of residual stress induced by crystallization strain is presented. This method calls for the concatenation of all processing induced strain (including phase-change strains, creep mismatch, and any other strains that may occur) into one quantity (termed "'effective processing strain"') which can be calibrated from the room temperature tests. The use of larger representative unit cells with varying geometric properties was shown to have a significant effect on the physical accuracy of the model, especially with regards to the prediction of the distribution of damage throughout the specimen. The spatial variance in microstructure allows damage to initiate at multiple locations. Initial damage at elements containing effectively weak RUCs is then arrested by effectively strong RUCs in the crack path, allowing damage elsewhere in the domain to initiate or grow. By contrast, the use of uniform RUCs throughout the domain tends to cause a single location of initial failure. Subsequent damage in the domain then spreads from this single initiation point.

7.2 Future Work

For future work on the experimental side of this topic, there are many ranges of additional testing that could be done. Only one elevated temperature was considered during this work. With greater specimen availability, a broader range of temperature should be used in testing to understand the behavior of the material through its entire service range, not just near the endpoints.

Another possible extension of this work would be testing with of elliptical, rather than circular rings. By varying the eccentricity of the ring, one could, obtain non-equibiaxial strain states at the crown of the specimen. A significant barrier to such testing is the significant shear stresses that develop off of the major and minor axes of the specimen. A clever design may be able to overcome these limitations. More data points around the failure envelope could be obtained by conducted saddle shear testing.

Most parts in service are limited not by monotonic strength, but instead are limited by fatigue or creep, or a combination of the two. The relatively simple practical nature of the ring-on-ring test would lend itself well to fatigue testing carried out in the zero-to-maximum-tension or minimum-to-maximum-tension R-ratio regime. Such a fixture could also be easily used in a load-controlled creep frame, and dwell fatigue could be used to test effects of combined loading. One limitation to any flexure-based fatigue test is the asymmetry of the load across the specimen thickness. Changes to the behavior of the compression-side plies could change the load state at the crown. The other major limitation to ring-on-ring in fatigue is the inability to enter a compressive regime on the primary ply side (the tension ply in the monotonic case). Other specimen configurations would be needed to test multiaxial fatigue that includes both the biaxial tension and biaxial compression regimes.

Related to this, the shear-lag model presented in Chapter 3 can be extended to include time-dependent behavior. A possible model for creep has been developed in a standalone sense, and is presented in Appendix B. These models could be combined to develop a combined creep-rupture model for CMCs. A more difficult task would be the inclusion of fatigue. Polymer- and metal-matrix composites can be modeled in fatigue by considering the cyclic behavior of the constituents. However, monolithic ceramics do not experience fatigue as it is typically understood. Thus, the mechanics for fatigue in CMCs (which has been demonstrated) would need to be better understood in order to include this behavior in micromechanical and multiscale models.

For future numerical work, the five-fiber randomized microstructure approach has not yet been shown to be converged (in terms of the number of fibers represented) for the multiscale simulations. A study could be conducted using larger RUCs, varied using similar methodology as the five-fiber model, to determine the number of fibers required to most accurately replicate the salient features of the experimental results. The major limitation of such a study would be the greatly increased computational cost of including a larger RUC (which necessarily requires a greater number of subcells). Additionally, it may be possible to instead introduce the effects of randomness not by varying the architecture, but by varying the strength of constituent materials associated with different elements at the FE scale. One possible approach to this problem would be to simulate many randomized subcells on a stand-alone basis and determine a relationship between architectural parameters and effective cell strengths. The statistical distribution of cell properties could

then be matched by choosing the correct distribution of subcell strengths. By implementing such as effective relationship, computational time could be reduced by reducing the number of fibers (and thus the number of subcells per RUC) necessary to capture the distribution of RUC behavior.

APPENDIX A

Summary of Tests

Spec. ID	Spec Type	Heat Treatment	Test Temperature
012-909-3-1	Biaxial Flexure, Square	None	Room
012-909-3-2	Biaxial Flexure, Square	None	Room
012-909-3-3	Biaxial Flexure, Square	None	Room
012-909-3-4	Biaxial Flexure, Square	None	Room
012-909-3-5	Biaxial Flexure, Square	None	Room
012-909-3-6	Biaxial Flexure, Square	None	Room
2007-01-0006-1.7-F-1	Biaxial Flexure	None	Room
2007-01-0006-1.7-F-2	Biaxial Flexure	None	Room
2007-01-0006-1.7-F-3	Biaxial Flexure	None	Room
2007-01-0006-1.7-F-4	Biaxial Flexure	None	Room
2098-01-0007-F-1	Biaxial Flexure	None	Room
2098-01-0015-F-1	Biaxial Flexure	None	Room
2098-01-0182-2	Biaxial Flexure	None	Room
2098-01-0182-3	Biaxial Flexure	None	Room
2098-01-0183-3	Biaxial Flexure	None	Room
2098-01-0007-F-2	Biaxial Flexure	10 hr @ 1315°C	Room
2098-01-0007-F-3	Biaxial Flexure	10 hr @ 1315°C	Room
2098-01-0183-1	Biaxial Flexure	20 hr @ 1315°C	Room
2098-01-0183-2	Biaxial Flexure	20 hr @ 1315°C	Room
2098-01-0226-F-1	Biaxial Flexure	None	1315°C
2098-01-0226-F-2	Biaxial Flexure	None	1315°C
2098-01-0227-F-1	Biaxial Flexure	None	1315°C
2098-01-0227-F-2	Biaxial Flexure	None	1315°C
2098-01-0226-F-2	Biaxial Flexure	Furnace Shutdown	1315°C
2098-01-0169-TD3	Tensile Dogbone	None	Room
2098-01-0160-TD3	Tensile Dogbone	None	Room
2098-01-0169-TD4	Tensile Dogbone	20 hr @ 1315°C	Room
2098-01-0169-TD5	Tensile Dogbone	20 hr @ 1315°C	Room

APPENDIX B

Concentric cylinder model for creep of Unidirectional CMCs

For materials intended for bearing load in elevated temperature environments, one must be able to analyze the creep response of the structure. To this end, the concentric cylinder model discussed in Chapter /refchap:eccm was adapted to approximate steady-state creep of unidirectional CMCs.

In this model, the microstructure considered is a three phase assembly of concentric cylinders: no outer phase with equivalent composite properties is used due to the nonlinear nature of the response. The microstructure considered is shown in Figure B.1.

For this model, only steady-state creep is considered, and the creep law given in Equation B.1 is taken as the starting point.

$$\frac{d\epsilon_c^{k,i}}{dt} = C^i e^{\frac{-Q^i}{k^i T}} (\sigma)^{m^i} \tag{B.1}$$

where constants C^i, Q^i, k^i, and m^i are the material constants for steady state creep for the i^{th} phase.

Two major simplifications are considered in this model, the first is that the incremental creep strain is distributed in a manner proportional to the elastic strain, shown in Equation B.2. This is done to allow the continued use of the CCM solution and maintain a closed form solution in space.

$$\epsilon_c^{k,i}(r,\theta) = \kappa^{k,i}(\epsilon_e^{k,i}(r,\theta)) \tag{B.2}$$

In Equation B.2, $\epsilon_c^{k,i}(r,\theta)$ is the accumulated creep strain in the i^{th} phase in the composite in the x_k direction, $\epsilon_e^{k,i}(r,\theta)$ is the elastic strain, and $\kappa^{k,i}$ is a proportionality parameter that will become the solution variable of the creep response.

The second assumption is that the incremental creep strain is driven by the *volume averaged* stress in each phase, rather than the locally resolved stress fields, as shown in Equation B.3

$$\Delta\bar{\epsilon}_{c,t+\Delta t}^{k,i}(r,\theta) = \Delta t(C^i e^{\frac{-Q^i}{k^i T}} (\sigma_{avg,t})^{m^i}) \tag{B.3}$$

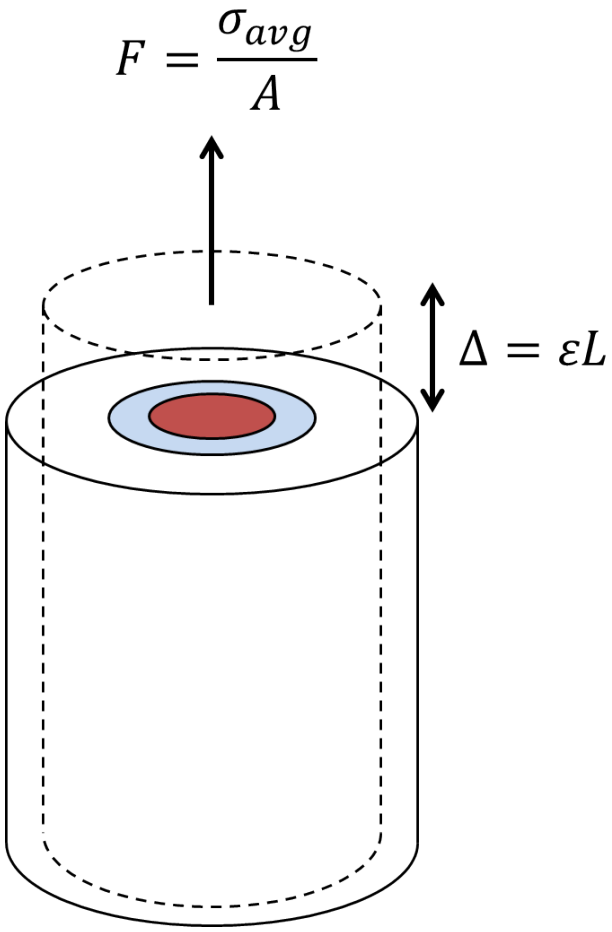

Figure B.1: Three-phase concentric cylinder assembly used for the creep model

where $\Delta\bar{\epsilon}_{c,t+\Delta t}$ is the volume averaged incremental creep strain from time t to Δt, and $\sigma_{avg,t}$ is the volume averaged stress at time t. Combining Equations B.2 and B.3 and solving for $\Delta\kappa^{k,i}$ yields Equation B.4, which describes the evolution of the solution parameter, $\kappa^{k,i}$.

$$\Delta\kappa^{k,i} = \frac{\Delta\bar{\epsilon}_{c,t} - \kappa_t \Delta\bar{\epsilon}_{e,t}}{\bar{\epsilon}_{e,t} + \Delta\bar{\epsilon}_{e,t}} \tag{B.4}$$

In this way, an average total creep strain is determined based on the average stress, and then re-distributed throughout the domain in a manner proportional to the elastic strain field. The cylinder is then subjected to an applied average axial stress, or an applied axial strain. The outer boundary condition is traction-free.

Figure B.2 shows the relaxation of stress in each phase of the CMC over a period of 1000 seconds. It can be seen that the initially very high values of stress present in the constituents due to processing-induced phase transformation. It should be noted that the phase transformation strain is applied instantaneously, rather than over a period of time that would allow for concurrent relaxation of the induced stresses.

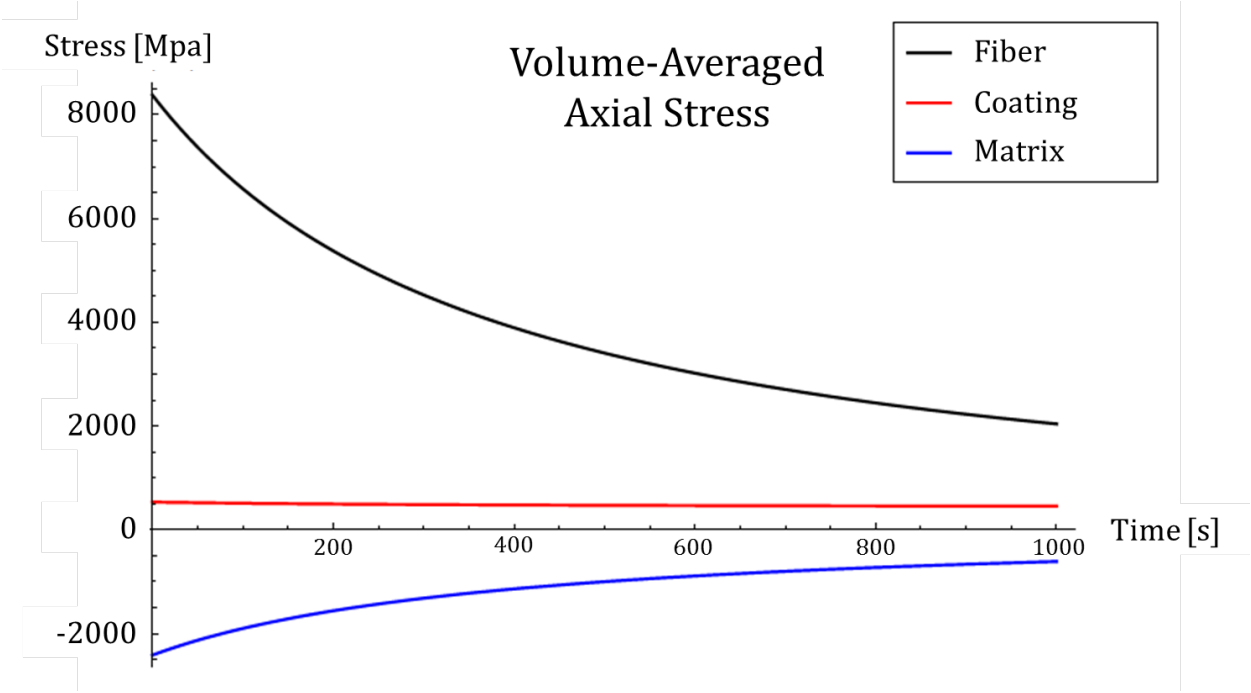

Figure B.2: Relaxation of axial residual stresses in the cylinder

For an illustration of a different problem that can be solved with this model, the unidirectional CMC is first subjected to 10 hour annealing time. After this annealing cycling, a constant load is applied in the axial direction of the composite. The composite response can be seen in Figure B.3.

As discussed in Section 7.2, this model could be combined with the shear-lag-based cracking

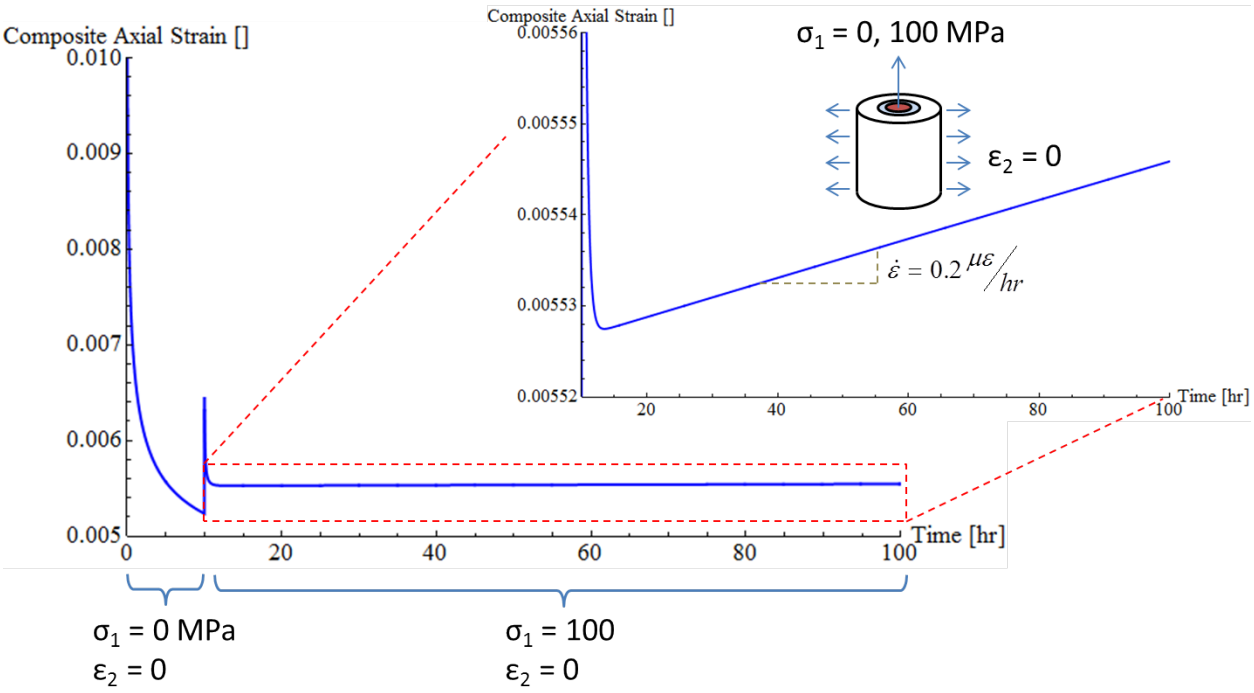

Figure B.3: Response of the CMC to a constant axial load, after a 10 hour stress free annealing.

model presented in Chapter 3 to provide a micromechanical model for combined creep and fracture response of CMCs. Such a model would include a parameter for accumulated creep damage or available creep life used.

APPENDIX C

Analysis of sub-microscale stresses in the CMC matrix

To test the accuracy of the high residual stresses measured by Raman spectroscopy, a finite element model was created using the commercially available software, ABAQUS. In this model, a spherical assembly of silicon and silicon carbide is processed to set in the residual stress due to silicon expansion, and to relax this stress through a cooling phase. After the cooling phase, a cutting operation is simulation, exposing the silicon inclusion. The hydrostatic stress at the center of the inclusion then measured, allowing a comparison to the experimentally observed stress state.

C.1 Model details

The geometric model used is three concentric spheres, representing a spherical inclusion of silicon surrounded by a thick shell of pure silicon carbide, as seen in Figure C.1. The third, outermost phase is an equivalent, homogenized composite of silicon and silicon carbide. This phase is not shown in the figure. The properties of this phase were determined using the relations in [68] and all properties are listed in Table C.1. The purpose of this outer phase is to provide the correct boundary conditions on the silicon carbide sheath such that the stresses in the silicon are not artificially amplified or reduced, as may occur with fixed displacement or traction free boundary conditions. The equivalent composite phase is very large compared to the silicon and silicon carbide phases, such that the smeared phase has an outer radius 10 times the radius of the silicon carbide sphere. This allows the explicit phases to be unaffected by the details of the boundary conditions on the outermost spherical face. The finite element mesh was created in ABAQUS 6.11, using C3DR brick elements with reduced integration.

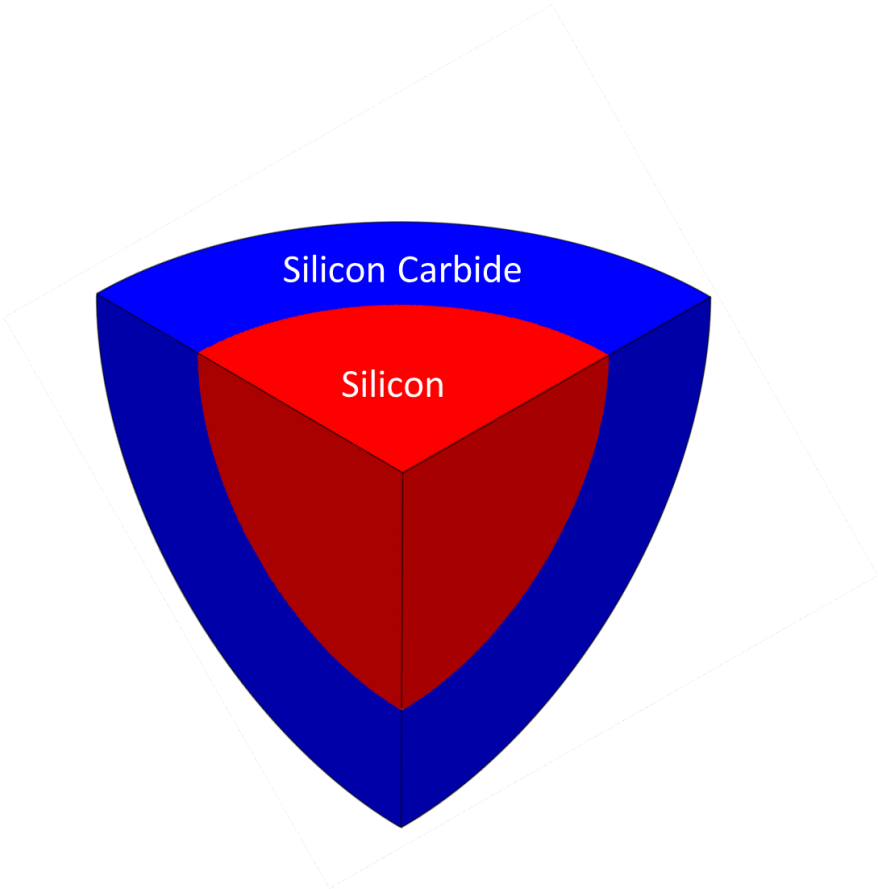

Figure C.1: Schematic of the spherical assembly. Red indicates silicon. Blue indicates Silicon Carbide. Note that the outer homogenized phase has been removed for clarity.

Property	Value
E_{Si}	155.8 GPa
ν_{Si}	0.215
$\alpha_{Si-Crystallization}$	3.2 x 10^{-2} mm/mm/K
α_{Si}	2.6 x 10^{-6} mm/mm/K
E_{SiC}	380 GPa
ν_{SiC}	0.14
α_{SiC}	1.0 x 10^{-6} mm/mm/K

Table C.1: Material properties used in the spherical model for subscale stresses

C.2 Simulation Details

The simulation is performed in 3 steps. In the first step, the crystallization strain is applied within the silicon inclusion. Since there is no built-in module for crystallization expansion within ABAQUS 6.11, this strain is implemented through assigning a large, negative thermal expansion coefficient, such that as the specimen is cooled from 1410°C to 1409°C, the correct expansion is set in. Below this temperature, the linear thermal expansion coefficient is used. In the second step, the assembly is cooled from crystallization temperature to room temperature (1409 to 23°C). During the first two steps, the appropriate symmetry condition is applied on all faces of the spherical octant. In the third step, the symmetry condition is removed from the y-normal face, simulating the cutting process. The faces affected in this step are outlined in Figure C.2. During this step, the stresses redistribute due to the removal of the y-symmetry constraint and subsequent removal of tractions on this face.

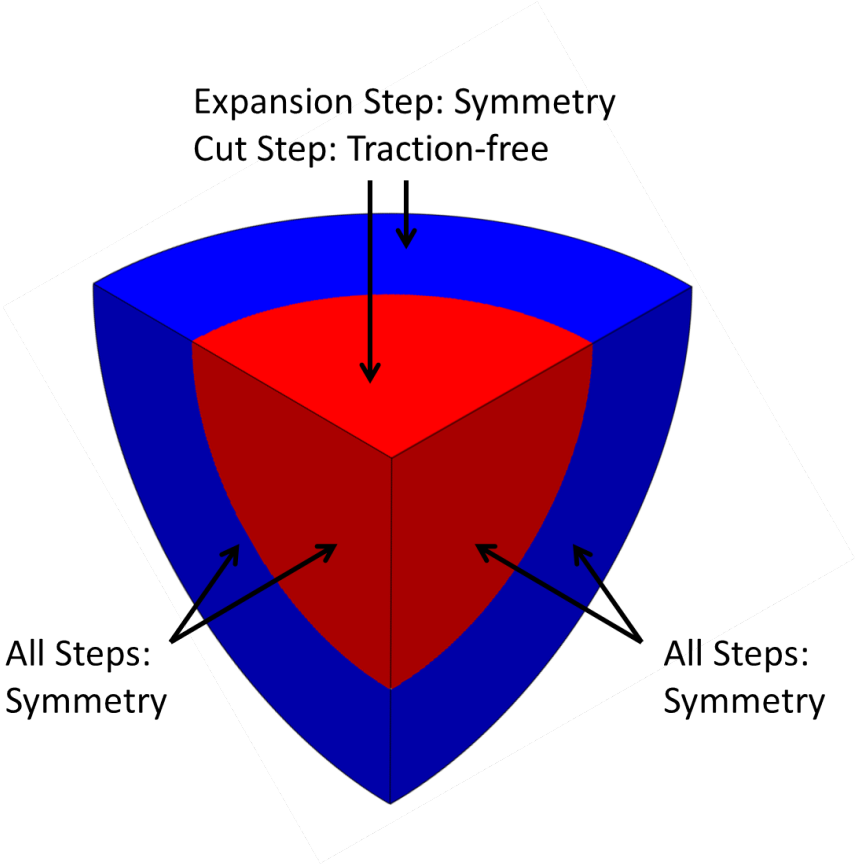

Figure C.2: Boundary conditions on symmetry faces of spherical assembly

The stress distribution in the sphere for a composite matrix with 30% volume fraction of silicon is shown in Figure C.3. Table C.2 describes the stresses seen in the sphere, pre- and post-cut for several values of silicon volume fraction.

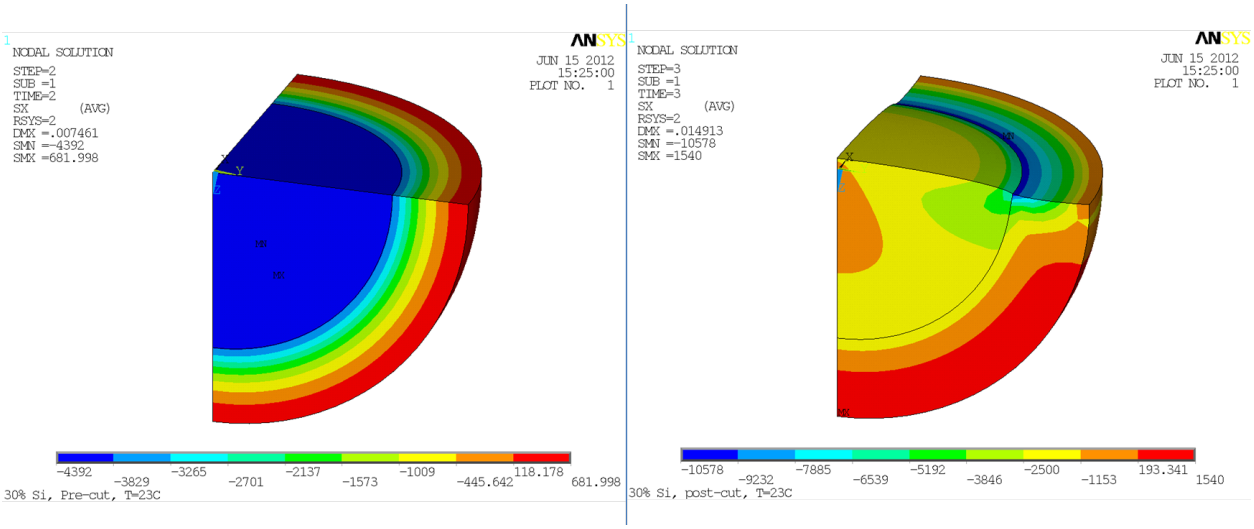

Figure C.3: Radial stresses in the sphere for a 30% volume fraction of silicon, pre-cut (left) and post-cut.

Volume Fraction of Silicon [%]	Hydrostatic Pressure at Center of Silicon Phase [MPa]	Hydrostatic Pressure at Si/SiC interface [MPa]	Hydrostatic Pressure at Outer Radius of SiC Phase [MPa]
10	-1520	203	509
20	-1330	380	1110
30	-1160	436	1584

Table C.2: Summary of post-cut stresses obtained from the sphere model

APPENDIX D

Shear Deformation of the Interphase

To determine the total shear deformation in a differential length of the coating, the coating is approximated by an elastic bushing separating a rigid, movable post from a rigid, fixed outer sheath, as shown in Figure D.1.

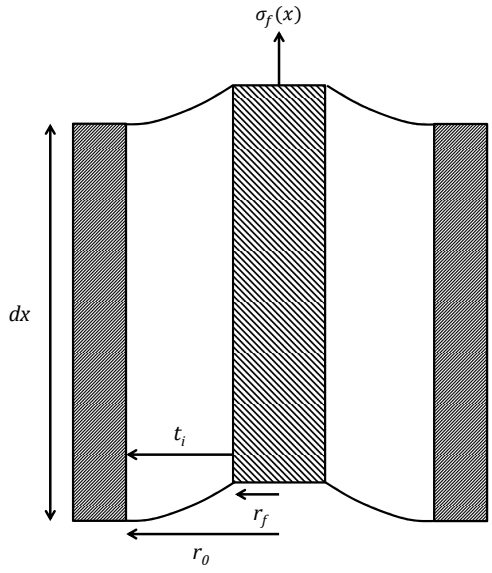

Figure D.1: A differential length of elastic bushing, representing the coating, between a rigid boundary (matrix) and post (fiber).

At any radius, r in the coating, the shear stress can be given as [34]

$$\tau_i(x,r) = \frac{\sigma_f(x) r_f^2}{r} \tag{D.1}$$

The shear strain at that point, then, is

$$\gamma_i(x,r) = \frac{1}{G_i}\frac{\sigma_f(x) r_f^2}{r} \tag{D.2}$$

Integrating the shear strain along the coating thickness gives the total shear deformation of the coating thickness at a given axial position.

$$u_i(x,r_0) = \int_{r_f}^{r_0} \gamma_i(x,r)dr = \frac{5}{6}\frac{\tau_i(x)}{G_i}\frac{(r_0^3 - r_f^3)}{r_0^2} = \bar{\gamma} t_i \tag{D.3}$$

where $r_0 = r_f + t_i$ is the outer radius of the coated fiber. This is the expression given in Eqn (3.11).

BIBLIOGRAPHY

[1] Corman, G. S., Luthra, K. L., and Brun, M. K., *Handbook of Ceramic Matrix Composites*, chap. Silicon Melt Infiltrated Ceramic Composites Processes and Properties, Springer, 2003, pp. 99–115.

[2] ASTM, "Standard Test Method for Monotonic Equibiaxial Flexural Strength of Advanced Ceramics at Ambient Temperature 1," 2009.

[3] Dunn, D., *The Effect of Fiber Volume Fraction in HiPerComp SiC-SiC Composites - Draft*, Ph.D. thesis, Alfred University, 2010.

[4] Marshall, D., Cox, B., and a.G. Evans, "The mechanics of matrix cracking in brittle-matrix fiber composites," *Acta Metallurgica*, Vol. 33, No. Il, 1985, pp. 2013–2021.

[5] Mccartney, L. N., "Mechanics of matrix cracking in brittle-matrix fibre-reinforced composites," *Proceedings of the Royal Society of London, Series A, Mathematical and Physical Sciences*, Vol. 409, No. 1837, 1987, pp. 329–350.

[6] Hutchinson, J. W., Budiansky, B., and Evans, A. G., "Matrix fracture in fiber-reinforced ceramics," *J. Mech. Phys. Solids*, Vol. 34, No. 2, 1986, pp. 167–189.

[7] Marshall, D. and Cox, B., "Tensile fracture of brittle matrix composites: Influence of fiber strength," *Acta Metallurgica*, Vol. 35, No. 11, 1987, pp. 2607–2619.

[8] Mital, S. K., Goldberg, R. K., and Bonacuse, P. J., "Two-dimensional non-linear finite element analysis of CMC microstructures," *Composites Part B: Engineering*, Vol. 57, 2014, pp. 144–154.

[9] Laumakis, P. J. and Bonacuse, P. J., "Monte-Carlo Simulation and the Chain-of-Bundles Model for Titanium-Matrix Composite Materials," *Journal of Composite Materials*, Vol. 35, No. 20, 2001, pp. 1795–1814.

[10] Gowayed, Y., Ojard, G., Prevost, E., Santhosh, U., and Jefferson, G., "Defects in ceramic matrix composites and their impact on elastic properties," *Composites Part B: Engineering*, Vol. 55, 2013, pp. 167–175.

[11] Zhang, D. and Hayhurst, D., "Stress strain and fracture behaviour of 0 / 90 and plain weave ceramic matrix composites from tow multi-axial properties," *International Journal of Solids and Structures*, Vol. 47, No. 21, 2010, pp. 2958–2969.

[12] Jones, R. and Henagerjr, C., "Subcritical crack growth processes in SiC/SiC ceramic matrix composites," *Journal of the European Ceramic Society*, Vol. 25, No. 10, 2005, pp. 1717–1722.

[13] Morscher, G. N., Yun, H. M., Dicarlo, J. A., and Thomas-Ogbuji, L., "Effect of a Boron Nitride lnterphase That Debonds between the lnterphase and the Matrix in SiC/SiC Composites," *Journal of the American Ceramic Society*, Vol. 87, No. 1, 2004, pp. 104–112.

[14] Jacobson, N. S., Morscher, G. N., Bryant, D. R., and Tressler, R. E., "High-Temperature Oxidation of Boron Nitride: II, Boron Nitride Layers in Composites," *Journal of the American Ceramic Society*, Vol. 82, No. 6, Dec. 2004, pp. 1473–1482.

[15] Smith, C., Morscher, G., and Xia, Z., "Monitoring damage accumulation in ceramic matrix composites using electrical resistivity," *Scripta Materialia*, Vol. 59, 2008, pp. 463–466.

[16] Lamon, J., "A micromechanics-based approach to the mechanical behavior of brittle-matrix composites," *Composites Science and Technology*, Vol. 61, No. 15, Nov. 2001, pp. 2259–2272.

[17] Pailler, F. and Lamon, J., "Micromechanics based model of fatigue/oxidation for ceramic matrix composites," *Composites Science and Technology*, Vol. 65, 2005, pp. 369–374.

[18] Marshall, D. B., "Analysis of Fiber Debonding and Sliding Experiments in Brittle Matrix Composites," *Acta metall. mater.*, Vol. 40, No. 3, 1992, pp. 427–441.

[19] Percival, M., Claxton, E., Gabelotaud, S., Dambrine, B., and Maire, J., "Material Testing for Multiaxial Macroscopic Modelling of Ceramic Matrix Composites," *Key Engineering Materials*, Vol. 127-131, 1997, pp. 791–798.

[20] Chen, A. and Matthews, F., "A review of multiaxial/biaxial loading tests for composite materials," *Composites*, Vol. 24, No. 5, July 1993, pp. 395–406.

[21] Danzer, R., Harrer, W., Supancic, P., Lube, T., Wang, Z., and Börger, A., "The ball on three balls testStrength and failure analysis of different materials," *Journal of the European Ceramic Society*, Vol. 27, No. 2-3, 2007, pp. 1481–1485.

[22] Salem, J. and Jenkins, M., "Biaxial Strength Testing of Isotropic and Anisotropic Monoliths," *Multiaxial Fatigue and Deformation*, 2012.

[23] Christensen, R. and Lo, K., "Solutions for effective shear properties in three phase sphere and cylinder models," *Journal of the Mechanics and Physics of Solids*, Vol. 27, No. 4, Aug. 1979, pp. 315–330.

[24] Tsai, S. and Wu, E., "A general theory of strength for anisotropic materials," *Journal of Composite Materials*, Vol. 5, 1971, pp. 58–80.

[25] Hashin, Z., "Failure Criteria for Unidirectional FibreComposites," *Journal of Applied Mechanics*, Vol. 47, No. June 1980, 1980, pp. 329–334.

[26] Basu, S., Waas, A. M., and Ambur, D. R., "Prediction of progressive failure in multidirectional composite laminated panels," *International Journal of Solids and Structures*, Vol. 44, 2007, pp. 2648–2676.

[27] Feyel, F., "Multiscale FE 2 elastoviscoplastic analysis of composite structures," *Computational Materials Science*, Vol. 16, 1999, pp. 344–354.

[28] Feyel, F. and Chaboche, J.-L., "FE2 multiscale approach for modelling the elastoviscoplastic behaviour of long fibre SiC/Ti composite materials," *Computer Methods in Applied Mechanics and Engineering*, Vol. 183, 2000, pp. 309–330.

[29] Feyel, F., "A multilevel finite element method (FE2) to describe the response of highly nonlinear structures using generalized continua," *Computer Methods in Applied Mechanics and Engineering*, Vol. 192, 2003, pp. 3233–3244.

[30] Kouznetsova, V. G., Geers, M. G. D., and Brekelmans, W. a. M., "Multi-scale second-order computational homogenization of multi-phase materials: A nested finite element solution strategy," *Computer Methods in Applied Mechanics and Engineering*, Vol. 193, 2004, pp. 5525–5550.

[31] Hill, R., "Theory of mechanical properties of fibre-strengthened materials: I. Elastic behaviour," *J. Mech. Phys. Solids*, Vol. 12, 1964, pp. 199–212.

[32] Christensen, R. and Waals, F., "Effective stiffness of randomly oriented fibre composites," *J. Composite Materials*, Vol. 6, No. October, 1972, pp. 518–532.

[33] Qiu, Y. P. and Weng, G. J., "Elastic Moduli of Thickly Coated Particle and Fiber-Reinforced Composites," *Journal of Applied Mechanics*, Vol. 58, No. 2, 1991, pp. 388.

[34] Timoshenko, S. and Goodier, J., *Theory of Elasticity*, McGraw-Hill, 1970.

[35] Corman, G. S. and Luthra, K. L., "Silicon Melt Infiltrated Ceramic Composites (HiPerComp)," *Handbook of ceramic composites*, chap. 5, Kluwer Academic Publishers, Boston, 2005, pp. 99–115.

[36] Ahn, B., Curtin, W., Parthasarathy, T., and Dutton, R., "Criteria for crack deflection/penetration criteria for fiber-reinforced ceramic matrix composites," *Composites Science and Technology*, Vol. 58, No. 11, Nov. 1998, pp. 1775–1784.

[37] Aveston, J., Cooper, G. A., and Kelly, A., "Single and Multiple Fracture," *The properties of fibre composites*, 1971, pp. 15–26.

[38] Talreja, R., "Continuum modelling of damage in ceramic matrix composites," *Mechanics of Materials*, Vol. 12, No. 2, Oct. 1991, pp. 165–180.

[39] Aboudi, J., "Micro-Failure Criteria for Coated-Fiber Composites," *Journal of Reinforced Plastics and Composites*, Vol. 10, No. 2, March 1991, pp. 146–157.

[40] Jayaraman, K. and Reifsnider, K. L., "Residual Stresses in a Composite with Continuously Varying Young's Modulus in the Fiber/Matrix Interphase," *Journal of Composite Materials*, Vol. 26, No. 6, Jan. 1992, pp. 770–791.

[41] Wagner, H. D. and Nairn, J. A., "Residual thermal stresses in three concentric transversely isotropic cylinders: Application to thermoplastic-matrix composites containing a transcrystalline interphase," *Composites Science and Technology*, Vol. 57, 1997, pp. 1289–1302.

[42] Hutchinson, J. W. and Jensen, H. M., "Models of Fiber Debonding and Pullout in Brittle Matrix Composites with Friction," *Mechanics of Materials*, Vol. 9, 1990, pp. 139–163.

[43] Waas, A. M., "Mechanics of Fiber Reinforced Composite Structures," 2009.

[44] Mccartney, L. N., "Predicting Transverse Crack Formation in Cross-ply Laminates," *Composites Science and Technology*, Vol. 58, 1998, pp. 1069–1081.

[45] Talreja, R. and Singh, C., *Damage and Failure of Composite Materials*, Cambridge University Press, 2012.

[46] Curtin, W. A., "Stochastic Damage Evolution and Failure in Fiber-Reinforced Composites," *Advances in Applied Mechanics*, Vol. 36, 1999, pp. 163–253.

[47] Przybyla, C., Prasannavenkatesan, R., Salajegheh, N., and McDowell, D. L., "Microstructure-sensitive modeling of high cycle fatigue," *International Journal of Fatigue*, Vol. 32, No. 3, March 2010, pp. 512–525.

[48] Pineda, E. J., Bednarcyk, B. A., and Arnold, S. M., "Effects of Subscale Size and Shape on Global Energy Dissipation in a Multiscale Model of a Fiber- reinforced Composite Exhibiting Post-peak Strain Softening using Abaqus and FEAMAC," *SIMULIA Customer Conference*, 2012, pp. 1–15.

[49] Sutcu, M., "A recursive concentric cylinder model for composites containing coated fibers," *International journal of Solids and Structures*, Vol. 29, No. 2, 1992, pp. 197–213.

[50] Arnold, S. M., "Paradigm Shift in Data Content and structure Required for Generalized Con- stitutive Modeling of Materials Behavior," *MRS Bulletin*, Vol. 31, No. December, 2006, pp. 1013–1021.

[51] v6.11, A., *Abaqus User's Manual*, Dassault Systems Simulia Corp, Providence, RI, 2011.

[52] Aboudi, J., "Micromechanical Analysis of Composites by the Method of Cells," *Applied Mechanics Reviews*, Vol. 42, No. 7, 1989, pp. 193.

[53] Aboudi, J., "The Generalized Method of Cells and High-Fidelity Generalized Method of Cells Micromechanical ModelsA Review," *Mechanics of Advanced Materials and Structures*, Vol. 11, No. 4, July 2004, pp. 329–366.

[54] Bednarcyk, B. a. and Arnold, S. M., *MAC / GMC 4 . 0 User ' s Manual*, NASA TM-2002-212077/VOL2, 2002.

[55] Kim, T. T., Mall, S., and Zawada, L. P., "Fatigue Behavior of Hi-Nicalon Type-S/BN/SiC Ceramic Matrix Composites in a Combustion Environment," *International Journal of Applied Ceramic Technology*, Vol. 8, 2011, pp. 261–272.

[56] Sha, J., Hinoki, T., and Kohyama, a., "Microstructure and mechanical properties of Hi-Nicalon Type S fibers annealed and crept in various oxygen partial pressures," *Materials Characterization*, Vol. 60, No. 8, Aug. 2009, pp. 796–802.

[57] Bazant, Z. and Lin, F.-b., "Nonlocal smeared cracking model for concrete fracture," *J. Structural Engineering*, Vol. 114, No. 11, 1989, pp. 2493–2510.

[58] Heinrich, C., *The Influence of the Curing Process on the Response of Textile Composites by*, Ph.D. thesis, University of Michigan, 2011.

[59] Červenka, J., Bažant, Z. P., and Wierer, M., "Equivalent localization element for crack band approach to mesh-sensitivity in microplane model," *International Journal for Numerical Methods in Engineering*, Vol. 62, No. December 2004, 2005, pp. 700–726.

[60] Dalle Donne, C., Trautmann, K.-H., and Amsutz, H., "Cruciform Specimens for In-Plane Biaxial Fracture , Deformation , and Fatigue Testing," *Multiaxial Fatigue and Deformation; testing and prediction*, 2000, pp. 405–422.

[61] Wing, B., private communication, 2014.

[62] Hill, R., "A Theory of the Yielding and Plastic Flow of Anisotropic Metals," *Proceedings of the Royal Society of London. Series A, Mathematical and Physical Sciences*, Vol. 193, No. 1033, 1948, pp. pp. 281–297.

[63] V.D., A. and Tsai, S., "Anisotropic strength of composites," *Experimental Mechanics*, Vol. 5, No. 9, 1965, pp. 283–288.

[64] Sha, J., Park, J., and Hinoki, T., "Strength and fracture properties od advanced SiC-based fibers," *Mechanics of Composite Materials*, Vol. 42, No. 6, 2006, pp. 527–.

[65] Choi, S. R., Kowalik, R. W., Alexander, D. J., and Bansal, N. P., "Elevated-temperature stress rupture in interlaminar shear of a Hi-Nic SiC/SiC ceramic matrix composite," *Composites Science and Technology*, Vol. 69, No. 7-8, 2009, pp. 890–897.

[66] Morscher, G. N., Baker, C., and Smith, C., "Electrical resistance of SiC fiber reinforced SiC/Si matrix composites at room temperature during tensile testing," *International Journal of Applied Ceramic Technology*, Vol. 11, 2014, pp. 263–272.

[67] Meyer, P., *Untitled PhD Thesis Draft*, Ph.D. thesis, University of Michigan, 2015.

[68] Luo, H., "On Eshelby's inclusion problem in a three-phase spherically concentric solid, and a modification of Mori-Tanaka's method," *Mechanics of Materials*, Vol. 6, No. 4, Dec. 1987, pp. 347–361.